Innovative Boundary Integral and Hybrid Methods for Diffuse Optical Imaging

Josias ELISEE

A dissertation submitted in partial fulfillment

of the requirements for the degree of

Doctor of Philosophy

of the

University College London.

Department of Computer Science

University College London

August 2011

Declaration

I, Josias ELISEE, confirm that the work presented in this thesis is my own. Where information has been derived from other sources, I confirm that this has been indicated in the thesis.

Abstract

Diffuse Optical Imaging (DOI), the study of the propagation of Near Infra-Red (NIR) light in biological media, is an emerging method in medical imaging. Its state-of-the-art is non-invasive, versatile and reasonably inexpensive.

In Diffuse Optical Tomography (DOT), the adaptation of numerical methods such as the Finite Element Method (FEM) and, more recently the Boundary Element Method (BEM), has allowed the treatment of complex problems, even for *in vivo* functional three-dimensional imaging. This work is the first attempt to combine these two methods in DOT.

The BEM-FEM is designed to tackle layered turbid media problems. It focuses on the region of interest by restraining the reconstruction to it. All other regions are treated as piecewise-constant in a surface-integral approach. We validated the model in concentric spheres and found that it compared well with an analytical result. We then performed functional imaging of the neonate's motor cortex in vivo, in a reconstruction restricted to the brain, both with FEM and BEM-FEM.

Another use of the BEM in DOI is also outlined. NIR Spectroscopy (NIRS) devices are particularly used in brain monitoring and Diffuse Optical Cortical Mapping (DOCM). Unfortunately, they are very often accompanied by rudimentary analysis of the data and the 3D appreciation of the problem is missed. The BEM DOCM developed in the current work represents an improvement, especially since a topographical representation of a motor activation in the cortex is clearly reconstructed *in vivo*.

In the interest of computational speed an acceleration technique for the BEM has been developed. The Fast Multipole Method (FMM), which is based on the decomposition of Green's function on a basis of Bessel and Hankel functions, eases the evaluation of the BEM matrix, along with a faster calculation of the solutions.

Acknowledgements

I would first like to acknowledge the contribution of Prof. Simon R. Arridge, my first supervisor. He was particularly helpful in suggesting the initial ideas which lead to the development and implementation of most of the techniques outlined here. Dr. Adam Gibson, my second supervisor, was also giving helpful and inspiring comments along with a sustained support for my work. Besides, I would like to thank the examiners Dr. Terence Leung and Dr. Oliver Dorn.

Dr. Athanasios Zacharopoulos and Dr. Jan Sikora are also to be recognised for their pioneering work in the design and implementation of the Diffuse Optical Imaging Boundary Element Method with quadratic shape functions. Their renewed input and the further development of the technique have been essential in the successful completion of my work.

I also want to thank Dr. Juha Heiskala, Dr. Martin Schweiger and Dr. Louise Enfield for their contribution to the development of the combined BEM-FEM. From the early ideas to the testing and implementation, they have been available to answer my questions and to support my work.

The outstanding support of Prof. Marc Bonnet in the implementation of the FMM has been very important in the development process and I want to thank him for that. His pedagogical approach to the matter has been very helpful. He is also a co-author of the software.

I would also like to thank all the other members of Prof. Arridge's group, Dr. Martha Betcke, Dr. Teresa Correia, Dr. Surya Prerapa, Tim Rudge and Dr. Vadim Soloviev for their

suggestion and contribution to the quality of my stay in the Centre for Medical Image Computing. The other members of the laboratory and staff also contributed.

The support and administrative staff of the Computer Science Department and more particularly Dawn Bailey, Patricia Fenoy, JJ Giwa, and Wendy Williams are also to be acknowledged for their help and support.

Last but not least, I would like to thank my parents, Dr. Philippe Elisee and Brigitte Elisee whose support has been essential to this work.

This research was supported by EC Seventh Framework programme, grant number: 201792, and by EPSRC grant EP/E034950/1.

Publications

Combination of Boundary Element Method and Finite Element Method in Diffuse Optical Tomography J. Elisee, A. Gibson, S. Arridge, IEEE Transactions on Biomedical Engineering, vol. 57 (2010), Issue 11, p. 2737-2745

Diffuse Optical Cortical Mapping using the Boundary Element Method J. Elisee, A. Gibson, S. Arridge, Biomedical Optics Express, vol. 2 (2011), Issue 3, p. 568-578

An Accelerated Boundary Element Method for Diffuse Optical Imaging J. Elisee, M. Bonnet, S. Arridge, Optics Letters, *submitted*

Contents

List of Figures

List of Tables

List of Acronyms

ACA Adaptive Cross-Approximation

BEM Boundary Element Method

BIE Boundary Integral Equation

BMT Bioluminescence Molecular Tomography

BOLD Blood-Oxygen-Level Dependent

CCD Charge-Coupled Device

CSF Cerebro-Spinal Fluid

CW Continuous Wave

DA Diffusion Approximation

DE Diffusion Equation

DOCM Diffuse Optical Cortical Mapping

DOI Diffuse Optical Imaging

DOT Diffuse Optical Tomography

DPF Differential Pathlength Factor

ECA Equivalent Cortical Absorption

EEG Electro-Encephalography

FDM Finite Difference Method

FEM Finite Element Method

FFT Fast Fourier Transform

FMM Fast Multipole Method

fMRI functional Magnetic Resonance Imaging

FMT Fluorescence Molecular Tomography

FMTXCT Fluorescence Molecular Tomography/X-Ray Computed Tomography

fNIRS functional Near Infra-Red Spectroscopy

FVM Finite Volume Method

FWHM Full Width at Half Maximum

GMRES Generalized Minimal Residual Method

ILU Incomplete LU

MINRES Minimal Residual Method

MONSTIR Multichannel Opto-electronic Near-infrared System for Time-resolved Iterative Reconstruction

MRI Magnetic Resonance Imaging

MTSF Mean-Time of flight Sensitivity Factor

NIR Near Infra-Red

NIRS Near Infra-Red Spectroscopy

PMDF Photon Measurement Density Function

PDP Partial Differential Pathlength

PET Positron Emission Tomography

RAM Random Access Memory

RTE Radiative Transfer Equation

TCSPC Time-Correlated Single-Photon Counting

TOAST Temporal Optical Absorption and Scattering Tomography

TPSF Temporal Point Spread Function

VENOM Vectorized Non-varying Shape Functions Method of Moments

XCT X-ray Computed Tomography

Chapter 1

Introduction

1.1 The place of optical techniques in medical imaging

The two major uses of medical imaging techniques are pre-clinical and clinical imaging. They each correspond to very different challenges. The optical method presented in this thesis can be used in both contexts. However, it is still mostly used in applied research. Some commercial products exist or have existed, especially in the field of small animal imaging (see subsection 2.1.1.3).

In the process of drug design (see Figure 1.1), pre-clinical imaging constitutes a major step in understanding a disease and ensuring the safety of a new molecule. It is first a modelling technique, with the test bench being the animal(s) studied. Functional imaging techniques, such as functional Magnetic Resonance Imaging (fMRI) or Positron Emission Tomography (PET) is much more difficult to use in this context than optical imaging. They allow to observe the physiological processes and progression of the disease. Fluorescence techniques, such as FMT even provide a better insight by allowing one to concentrate on a particular process by designing the fluorescent probe so that it is active only where the process of interest takes place. Coupled with an anatomical imaging technique, such as X-ray Computed Tomography (XCT) or Magnetic Resonance Imaging (MRI), the optical methods become very useful and provide a localized functional insight.

In the field of functional clinical imaging, fMRI is the most used technique. It is very easily coupled with MRI and provides functional information up to a millimeter resolution. The other most widely used technique is PET, although its usage is more difficult with humans, especially because of the small period of the fluorine 18 and the effects of the radiations it emits. Optical imaging techniques, in diagnosis or observation are very marginal and actually corresponds to one of the aims of the research in this field. We know that it will take time before the technique is accredited. It is currently confined to research in brain, breast and rarely

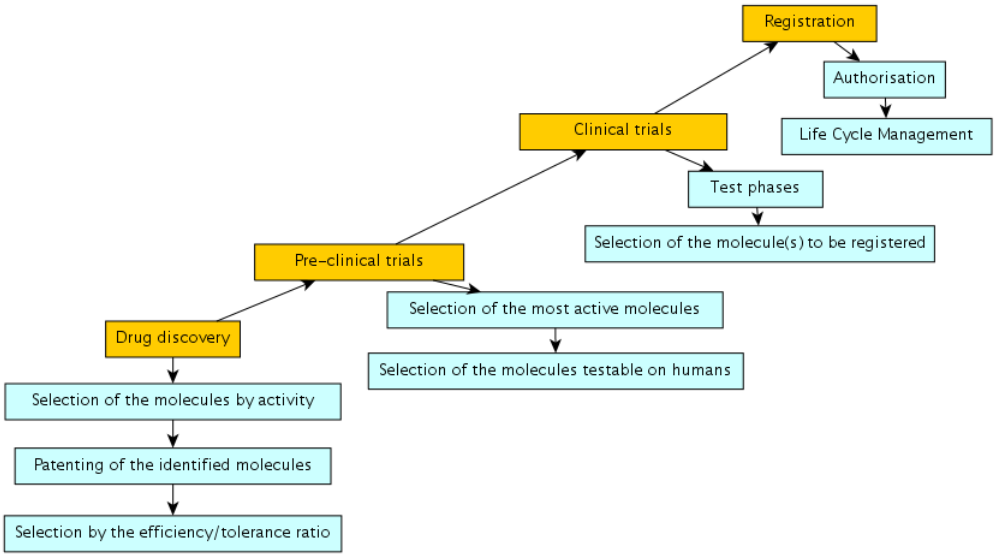

Figure 1.1: Drug design process

limb imaging (see subsection 2.1.1.3). Near-infrared spectroscopy, however, is used beyond the sole optical imaging research, especially in neurology and cognitive sciences, disorders and activations are monitored with commercially available devices (see subsection 2.2.2).

1.2 Diffuse Optical Imaging framework

If the diffusive media observed with DOI are biological tissues (which is the case considered in our study), it usually exploits the so-called "optical window" (Figure 1.2 and [11]), in the Near Infra-Red (NIR) spectrum to investigate its targets. In practice, the biological tissues absorb NIR light much less than photons in the visible spectrum, making the detectable propagation of photons from one end surface to the other more likely. However, one should notice that the diffusion process only takes place after a relatively long distance (the transport length) is traveled within the turbid media (see Figure 1.3). The diffusely reflected and diffused photons obey to the same laws but refer to two slightly different imaging techniques, especially distinguished when Charge-Coupled Device (CCD) cameras are used, respectively transmission and reflection imaging. They constitute the photons that we are interested in. The absorbed photons are also included in our energy balance calculations, since they are sent by the source but never reach the detectors. The ballistic photons are rare and difficult to measure, especially in thick turbid media. They travel accross without being disturbed on their path and are the first to reach the detectors. Lastly, the specular photons are of no interest in our study, since they do not travel through the media investigated.

When diffused in the tissue, the photons are also absorbed (like any other electromagnetic

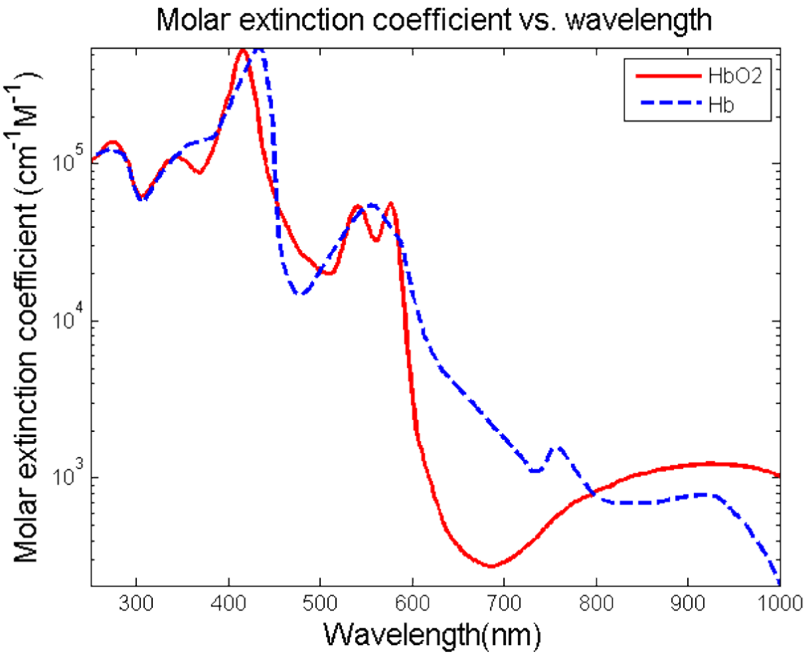

Figure 1.2: Absorption spectra of the most commonly met molecules in DOI adapted from BME591 Wikiproject. A more complete version can be found in [1] (Hb: hemoglobin)

wave within a non-void medium) and refracted. It means that the parameters of the diffusion depend on at least three properties:

μ_a, the absorption coefficient

μ_s, the scattering coefficient

n, the refraction index

In a strictly diffusive theory, using a first order approximation of the phase function, only one parameter is missing from the above list, namely the average cosine of angle scattering [12], usually noted g. These parameters and the actual physical model of diffusion can be derived

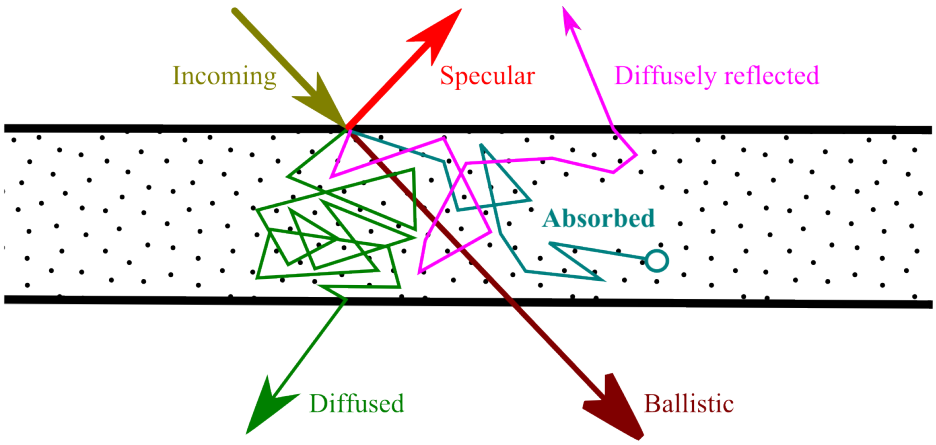

Figure 1.3: Example paths of photons through tissue - we are only interested in the diffused ones

from a more general theory (see section 3.1). We will not discuss the refraction effects in this thesis.

1.2.1 Model-Based Iterative Image Reconstruction

In all DOI methods described in this thesis, the unknown is the distribution of the optical properties (actually only the absorption coefficient here) within the investigated medium. This is then linked to the functional activity of the biological tissue probed.

We illuminate the medium with a known source and surface photon density measurements are taken. This is usually done with optical fibers acting as sources and detectors. CCD cameras can also be used [13, 14, 15, 16, 17] along with multi-wavelength sources [18, 19, 20] but they require a different treatment and acquisition process.

In order to reconstruct the optical parameters, the measurements taken on the turbid medium's surface have to be completed by a geometrical model of the system, of the source and of the detectors. One then builds a numerical model called the Forward Model. It is the simulation of the actual experiment. An Inverse Problem solving method is then applied to make the actual surface data and the surface data coming from the Forward Model match. More details about the means used to solve the Inverse Problem are given in section 4.2. We particularly notice that, in this thesis, the problem is always reduced to a linear single-step Gauss-Newton approach which implies the assumption of the background optical properties of the turbid media.

This thesis is about improving the Forward Model and making it easier to setup. The basic principles of existing reconstruction methods will not be changed.

1.2.2 Numerical Methods used for the Forward Model in DOI

Various numerical methods can be used for the forward model which represent different approaches to the solving of a partial differential equation on a 3D geometry. Most of the conventional techniques come from mechanical engineering. These include, the Finite Element Method (FEM) [7, 21, 22, 23], the BEM [24, 9] and the Kirchhoff Approximation thereof [25], the Finite Difference Method (FDM) [26, 27] and the Finite Volume Method (FVM) [28, 29, 30].

Boundary integral based methods are useful when one can consider large regions of the turbid medium as piecewise-homogeneous. This means that assumptions have to be made regarding the distribution of optical parameters and the position and value of the perturbations searched for [31, 9]. The principle behind the BEM is to use Green's second identity [32, 33] and to describe the field through its integral on the surface: in the Diffuse Optical

Tomography (DOT) and Diffuse Optical Cortical Mapping (DOCM) cases, the photon density and flux. The main advantage of the method is the avoidance of high-resolution volume meshes (needed by the FEM, FDM and FVM) which are time-consuming to construct and can introduce errors especially when thin layers are involved. It is also easier to create adaptive meshes [34] and methods to handle non-scattering regions [35] using the BEM. However, in a conventional approach, as so far used in DOT, the BEM matrix arising from the discretisation of the problem is full and non-symmetric and in addition suffers from intrinsic ill-conditioning [33]. Furthermore the piecewise-constant assumption is too restrictive for use in the inverse problem and does not allow the level of detail or flexibility of the volume mesh or volume grid-based methods. Despite these limitations, this thesis is there to show the use of this method in DOT and Optical Topography.

Chapter 2

FEM, BEM and Cortical Mapping

2.1 The Finite Element and Boundary Element Methods in Diffuse Optical Tomography

As early as in the 1970s [36], the association of the FEM with a boundary solution has been proposed. Such a combination allows one to sum the advantages of the two methods and extend the range of problems solvable with such algorithms.

The FEM is widely used in Diffuse Optical Tomography since the first study by Arridge *et al* [37], especially for its flexibility and referenced accuracy [21, 22, 23]. Volume integrals-based reconstructions of optical properties, especially the absorption coefficient, are of particular interest. For example, they allow a lot of freedom for the priors definition [38] and fine reconstructions [39]. The well-known [13, 14, 40] Temporal Optical Absorption and Scattering Tomography (TOAST) software package for Optical Tomography is currently based on this technique. It reaches its limits when dealing with thin multiple layers (see the mathematical formulation in the next section).

On the other hand, the BEM is surface-based, a feature which allows to model finely multilayered geometries with ease. In a paper from Sikora, Arridge *et al* [24], a pure BEM forward model was proved to be an excellent alternative to the common volume integral-based techniques. However, the treatment of multiple large-scale inhomogeneities (coming out of *a priori* knowledge of the position of uninteresting organs, layers or other structures) is more challenging and requires the addition of many extra boundaries.

In our study, we chose to address the problem of thin layers and spread inhomogeneities in combining the BEM and FEM. This association has already been tested in the fields of continuum mechanics [41], elastostatics [42, 43], electromagnetics [44], etc. For example in the study by Guyot *et al* [41], the BEM is used for the modelling of the two surfaces in direct contact, where the FEM is not converging correctly (thin layer). On the other hand, the known

inhomogeneous structure and the thickness of the pipe's shell in Kortschak *et al*'s study [44] allows a simpler treatment with the FEM. However, no reported attempt had ever been made to combine these methods in the field of optical imaging.

2.1.1 Finite Element Method in DOT

2.1.1.1 Origin and history

First mention The physical models used to represent reality are infinite-dimensional partial differential equations, on which only few purely analytical methods can be applied to reach the solution. These analytical schemes are only able to be used adequately in a small number of trivial cases. The idea lying behind a FEM is to reduce a complex problem to a finite-dimensional system by dividing it in a large number of elements and searching the system's solutions as a linear combination of highly regular shape functions associated to these elements.

Before 1953, the most commonly used method for the solving of complex engineering problems, especially in the mechanical and aeronautical engineering fields was the FDM. This technique is not using a discretization of the system's shape, but of the space, since it needs a regular grid to be applied [45]. Unfortunately, the assumptions needed to be able to write the problems in this form are numerous [46] and prevents it to be applied to complex configurations such as those met in aerodynamics [47].

It was not an easy task for the post-war computational engineers and scientists of the early 1950s to switch from the FDM to the FEM. In the first problem ever reported to be solved by the FEM, the stiffness problem of the delta wing [47], the pioneer of this approach, Clough, first attempted to model the wing with 1D elements without success. It is then his supervisor Turner who had the idea to extend the "elements" to create a 2D mesh, the first ever recorded. Their work is presented in the original paper on what was then called the Boeing Direct Stiffness Method [48].

The FEM comes from a mostly recent background as stated in the introduction of [49] and contains many areas with research incentives. However, we will focus exclusively on its usage in DOT.

2.1.1.2 Features and advantages

Basic principle The FEM in DOT is used for the forward model, i. e. to compute the energy density within the diffuse media and relate it to a simulated detection. For details on the reconstruction method, see section 4.2.

When placed in this section of the DOT problem, the FEM allows to define regions with mismatching optical properties (absorption and scattering inhomogeneities) with an accuracy

depending on the fineness of the mesh. All the operators of the diffusion equation are developed on element-wise shape functions of various types [37], with linear and quadratic functions being the most used. The diffusion equation in frequency domain, as in eq.(3.12), can then be written with a system matrix (M) operating on the energy density (φ) on the left-hand side and a nodal source term (Q) on the right-hand side:

$$M\varphi = Q \tag{2.1}$$

Actually, the M matrix represents the action of the diffusion operators (see section 3) which is, depending on the solving algorithm, inverted explicitly or optimized in a least-squares formulation.

From the nodal energy density distribution on the surface of the system, one can find the approximated detected signal by multiplying this energy density by a nodal measurement distribution, as in eq.(4.6).

Advantages The main advantages over the other numerical techniques such as the FDM [27, 26] or the FVM [29] are its ability to model very complex 3D structures relatively easily, thanks to the high sparsity of the resulting forward model matrix [50], as well as taking in account boundary effects.

The matrix's sparsity comes from the fact that only adjacent elements (those who share one or more nodes) have a non-zero shape function product. Since all the diffusion operators have to be discretized on this basis of shape functions, the resulting matrix becomes very sparse with only very few non-zero values per row.

de facto, the FEM has become a standard for the treatment of (real) systems which have a complex geometry and a highly inhomogeneous background such as the breast [19, 51], the fingers [52], small animal imaging [14], the neonatal brain [40] and parts of the adult brain [53]. These abilities especially show up when two imaging modalities are combined, for instance when MRI segmented regions are used as a background information in the reconstruction [54].

2.1.1.3 Applications and current trend in the volume integral-based DOT

Premature infants The historical application of the FEM in a "close-to-clinical" optical tomography setting is the problem solved by Hebden *et al* [40]. This milestone is one of the most important in the establishment of the FEM as a practically usable computational technique.

Premature infants often suffer from ischemia-related blood vessel damage or haemorragia due to perinatal conditions [55]. Normally, the observation and diagnosis of their state must be done early enough (ideally within 15 hours from the birth [56]) to assess the actions to be

taken before irreversible brain damage is inflicted by the injury. The only techniques applicable in such contexts are ultrasound-based technologies such as color Doppler-ultrasonography [57] and MRI-based techniques such as described by Ferriero [58]. Unfortunately, few maternities can afford MRI scans for premature babies in such short periods of time after birth, and reliable and portable ultrasonography techniques designed to be used in an intensive care unit environment are still in development.

In the case of optical tomography using the FEM, the intrinsic high heterogeneity of an actual premature infant brain seems to require a deep insight into the modelling technique. To find a contrast between an heterogeneous background and an heamorragia does not require a perfect knowledge of the anatomy of the baby. Hebden *et al* managed to recover the asymmetry of an hypoxic-ischemic injury in an infant's brain while taking as a reference for their perturbative DOT reconstruction approach a balloon filled with an homogeneous intralipid solution. In addition to that, the FEM mesh used was representing a baby doll's head warped onto a helmet of sources and detectors.

We will see that part of our planned work coincides with this study and the improvement of the head model used for the computation.

Other research groups have worked on this subject recently, and we would want to single out the study by Heiskala *et al* [59], in which they assessed the importance of the optical parameters distribution in the reconstruction using simulation on Monte Carlo-based data. They concluded that although an heterogeneous representation of the neonatal head in the mesh does contribute to accuracy, a layers-based technique gives more accurate results, especially in terms of depth recovery.

Adult brain The adult brain, especially the uppermost layer, the cerebral cortex, was investigated by Bluestone *et al* [53]. They recovered changes in the hemoglobin concentration in superficial areas of the brain using the FEM for the reconstruction.

However, this biological tissue is very thick for near-infrared light to pass through. The depth limite of breast imaging (see paragraph 2.1.1.3) for example is overtaken by the necessary source-detector distance due to the human head's shape and goes down to about 1.5 cm. This theoretical limit comes out of a sensitivity study for the use of the current FEM in this case by Dehghani *et al* [60] on a large-scale (whole head of 90000 nodes mesh) simulation. Experimentally, this value varies between 5 and 10 mm [61] or slightly more [62] up to 15-20 mm. This is very close to the size of the extracerebral layers, which varies between 8 [62] and 14 mm [63]. It means that only the superficial layer of the adult brain (cortex), which is very largely flat (at the resolutions achieved by DOT), is imaged. Due to these limitations, the

current clinical applications of the investigations on this system in tomography are few, if any. The optical topography mode is further described in chapter 7.

Another study where layers played an important role is the series of experiments by Huppert *et al* [64] where they reached an outstanding 3D positioning precision of oxy- and deoxy-hemoglobin rate change targets on the brain surface. According to the article's authors, it shows similar patterns to the fMRI findings. Although not being DOT, it used a layered forward model FEM code designed for DOT: NIRFAST [19, 65], a package similar to TOAST.

Limbs, joints and muscles The capacity of DOT with the FEM to image absorption differences in bones and oxygenation in muscles allows its application range to reach the area of movement effect observation and articulation damage assessment. Arthritis, for example, is a major disease [66] of which the effects on the joints and articulation can be seen through changes in the absorption and scattering coefficients [67, 68] using these techniques.

Thanks to its versatility, especially in the case of a reference-free (non-linear, see section 4.3) problem solving, the FEM was used in a study by Xu *et al* [52] in which they recovered acceptable scattering and absorption coefficients for the bone and synovia in healthy finger joints. This first attempt was followed by more extensive studies using the RTE and Monte-Carlo Simulations by A. Hielscher's group [26]. These studies do not involve the FEM or the diffusion approximation.

Hillman *et al* also made a breakthrough in this field by imaging the arm activity during exercise with DOT [69]. Activation patterns have been proven to be visible, even within the context of the Diffusion Approximation (DA), using the FEM.

Breast Imaging This area is one of the earliest application of optical imaging. It has been reported as being employed by Cutler in 1929 to observe lesions in the breast [70]. It was then called diaphanoscopy, and consisted simply in observing the inner structures of the breast with visible light.

Since then, considerable improvement have been made and the 3D resolution, thanks to the FEM, has been reached. The first report of such an achievement with pure optical tomography (an ultrasound aided one had been done before [71]), in a Continuous Wave (CW) framework, was made by Jiang *et al* [72]. Using the FEM, they recovered the characteristic signals of two tumors. Although, because of the CW setting, absorption and scattering were not properly separated [73].

Because of the growing concerns on breast cancer [74] particularly and also on other pathologies [75] affecting this organ, widespread efforts are made to improve the specificity and accuracy of DOT and FMT in this field. The depth limit has been pushed back to about 4-5

cm. The seminal work of Choe *et al* [10] proves that DOT can detect the effect of chemotherapy (or the absence of effect) earlier in the therapy than MRI using the FEM and the DA (see also [76]).

Small Animal Imaging The Fluorescence Molecular Tomography/X-Ray Computed Tomography (FMTXCT) scanner which is developed by some members of our research group in collaboration with our european partners (FMTXCT project) is designed to perform mouse, rat and rabbit imaging for the monitoring of animal models of human diseases. In fact, recent developments in genetic engineering [77] have allowed the emerging of an intensive effort on studying human diseases this way, and investigate them with *in vivo*, non-invasive optical imaging [78, 79].

However, the reliability and accuracy of the optical tomography, and more specifically of the DA in this field is debated by some. For example, Klose *et al* [80] expressed concerns about its use in setups where the sources and detectors are close to each other and where very thin layers are present. One will notice that they are using the FDM which itself is less adapted to the complex geometries met in small animal imaging compared to the FEM [50].

Focusing on DOT using the FEM and the DA, we realize that this method is indeed applicable, since it is the basis of a significant part of the studies [81]. In the particular case of *in vivo* small animal imaging where the proper treatment of the complex geometry requires a fine analysis, unlike the compressible/easily immersible breast which geometry can be modified for example, anatomical data is obtained prior to the actual *in vivo* optical tomography. Then, a FEM mesh is generated and, depending on the resolution required and the expected accuracy of the reconstruction algorithm, the segmented mesh is assigned background optical properties.

One should distinguish two types of tomographic optical imaging in the case of small animals. First, the endogenous contrast imaging, similar to what we saw before, where the scattering and absorption coefficients are recovered (sometimes at multiple wavelengths [82]) They can lead to various values in the environment such as the concentration of oxidised hemoglobin versus the concentration of deoxy-hemoglobin, depending on the information available [83, 84].

The exogenous contrast can be achieved through the use of fluorescent [85, 86, 87, 88] or bioluminescent probes [89] mainly. Companies, such as QUIDD S.A.S. (QUantitative Imaging for Drug Development with their QUIDD Optical System scanner, Saint-Etienne du Rouvray, France), Visen Medical (with their FMT Scanner, Woburn, Massachussets, USA) and Caliper Life Sciences (with their IVIS Spectrum scanner, Hopkinton, Massachussets, USA) develop such probes along with their associated FMT scanner. This modality is the most looked upon by external players, since the 2D fluorescence imaging was, and is, still of primary importance

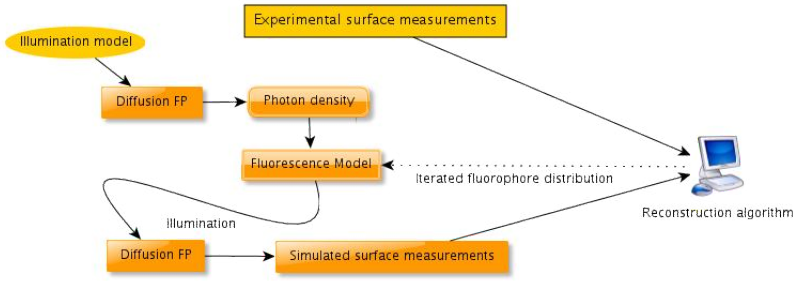

Figure 2.1: Double diffuse optical tomography forward model of FMT (FP: Forward Problem) in a MOBIIR scheme (Model-Based Iterative Image Reconstruction [2, 3, 4])

in a number of pharmaceutical applications along with the new 3D abilities that FMT provides [90, 91]. The monitoring of animal models of diseases and its response to chemical stimuli such as induced by engineered chemicals is a long lasting area of research and a key step in the development of drugs [92, 93].

Small animal imaging is the main modality in which exogenous contrast is met [17]. In the particular case of fluorescence, two different problems must be adressed:

- the **excitation** problem
  - *Source:* excitation light source
  - *Outcome:* photon density in the medium
- the **fluorescence** problem
  - *Source:* fluorophores excited by the photon density in the medium found in the previous problem
  - *Outcome:* final signal

This combination constitutes the FMT forward model (see Figure 2.1). In the case of bioluminescence, the forward problem is reduced to the fluorescence problem: the technique is then called Bioluminescence Molecular Tomography (BMT) [94].

2.1.1.4 Limits of a volume mesh-based method

Void (non-scattering) regions It is well-known that the FEM fails to recover proper optical parameters when confronted by void regions [95]. This is due to the failure of the DA formulation it models. The integral equations have to be modified to take in account the low-scattering region in order to correctly represent the phenomenon observed in this case [96]. This includes the Cerebro-Spinal Fluid (CSF) layer present between the grey matter and the skull [97, 5]. In our work, however, the CSF is not taken in account at any time. This is a common custom in

the tomography of the neonatal brain [40, 98]. In adults, it can significantly alter the results by modifying the shape of the measurements' sensitivity as seen in Okada *et al* [5]. As we will see in a subsequent section, the CSF's influence can be taken in account by restraining the reconstruction to the outer cortex layer, the only reachable region of the adult brain. Once more, the CSF cannot be properly modelled with the diffusion approximation alone [96, 99, 100], especially with complex geometries such as a multi-layered model of the neonate's head. The BEM-FEM presents an advantage over the FEM in this particular problem, since it has been proven that, a formulation very interpretable as a BEM-FEM hybrid equivalent has been combined with a radiosity-diffusion model of the propagation of photons in the CSF, the forward model can be matched against a more rigorous technique based on the RTE [96]. However, no attempt to implement this has been made in our work.

Thin layers The treatment of thin layers by the FEM on complex geometries requires the generation of a large number of small elements which in addition have a sometimes strong discontinuity in optical properties inherent to the layered structure. This effort should be avoided, since it generates a computational weight which slows down the overall solving process.

We do not consider here the actual computational effort made to generate the meshes which is very comparable between surface and volume meshes when using the appropriate tools. We rather speak about the optimization process needed to obtain a mesh which properly represents the layered nature of the biological media. Volume meshes like the one presented in [101] are not easy to obtain since some tetrahedra in the thin layers have to be very small to fit in them. Large disparities in element sizes have been proven to have a negative effect on the interpolation error [102, 103] (by compromising the conditioning of the system matrix, for example), and the only stable solution would be a very fine meshing all over the geometry. Such mesh densities are sometimes unpractical and ask for an additional computational effort. However, this is the solution we chose to compare the BEM-FEM results with a FEM solution later in this thesis and in the article we have published. Actually, as it can be seen in the reconstruction pictures (see section 6.2), the skull layer is so thin at some points that almost no grid element was found being completely inside it. This resulted in an extrapolation to the grid base which does not exhibit to the naked eye any skull layer. In fact, this layer is present in the values given to the absorption and scattering around it which differ from the "pure" scalp or "pure" brain. One can argue that, in order to really get to a point where every layer is easily recognisable everywhere in the mesh, an even higher mesh density should have been used for the restricted FEM. This would have severely altered the Jacobian building time and might even have proven the restricted FEM slower than the BEM-FEM.

Computational effort One might argue that there are no alternatives to a finer mesh when wanting to represent thin layers, if we want to stay in the diffusion theory framework. It is true that it was the case in the 1990s, when techniques like the BEM, which "skips" the treatment of homogeneous volumes and only considers their boundary in an integrated manner, were slow and not very distinguishable from the FEM [104]. Actually, although a boundary meshing involves obviously less unknowns, the linear equations to solve in the forward model are more complicated. In our particular DOT case, we will see that, with the current implementations, the FEM generates sparse system matrices while the BEM generates full ones. However, we will also see in the next subsection that recent advances in the numerical implementation of the BEM changes the mathematical landscape in its favor.

2.1.2 Boundary Element Method in DOT and FMT

2.1.2.1 Origin and basic principle

Actually, as mentioned in subsection 2.1.1.1, the first FEM problem solved was actually using 2D surface elements to represent a 3D thin volume. The BEM goes beyond this approach by considering integrated quantities over the volume. It was proposed very early on as an alternative to the FEM, and was actually "born" in the UK, thanks to the pioneering work of two researchers from the Imperial College London, Jaswon and Symm [105, 106]. From its "boundary integral equation" initial name it became the BEM in Brebbia *et al*'s pioneering work [107].

One has to wait until Ripoll's seminal work [108, 109] to see a surface integral formulation being applied with success to the DOT problem. And before the unique shape-based reconstruction scheme developed by Zacharopoulos *et al* [9], reconstruction methods with the BEM were not comparable in shape accuracy to the FEM, although fundamental differences still remain. However, one will notice that the BEM in DOT still suffers from severe slowness as seen in the second figure of [110] for example. It has been tested on various models, from a human head model [24] or a mouse head model [111] to a small animal's chest phantom [112]. It still lacks *in vivo* tests.

The advances made from these early works are summarized in [33].

In its modern form, the BEM uses Green's second equality [32] which enables us to directly and simultaneously compute the photon density and flux on the surface. It thus needs only to discretize surfaces and the continuity in the volumes is automatically ensured. This is a reduction of dimensionality [113, 114].

2.1.2.2 Advantages

Mesh generation Not meshing the inner part of a system considerably reduces the modelling time and allows an easier consideration of adaptative techniques [34]. It avoids the presence of a large number of thin elements. It significantly facilitates the handling of infinite and semi-infinite domains as well.

In the particular treatment of data from patients, which involves the treatment of changing biological media geometries due to the anatomical features of each subject, the BEM eases the process of adapting the discretization meshes. Actually, in our work (see subsection 6.2.1), we used this particular ability to generate the patient-specific meshes presented.

Computational accuracy Green's second equality gives the photon density simultaneously with its normal derivative on the surface, the photon flux, contrary to the FEM. A separated processing of the photon density to obtain the flux needed for the computation of the intensity measurements on optical detectors introduces an additional error level in a volume integral-based framework.

Treatment of non-scattering regions Compared to the FEM, it can directly handle void regions and provide accurate results [35]. However, these considerations are outside the DA framework.

2.1.2.3 Fundamental limitations

Matrix handling Although the treatment of less nodes obviously reduces the number of unknowns and of equations, the BEM matrix is very densely filled. In a regular approach, like the one used so far in DOT, the BEM matrix is non-symmetric [24]. In addition to that, it suffers from intrinsic ill-conditioning [33].

Non-straightforward reconstruction One of the fundamental assumptions made in BEM is that the space optical properties are region-wise constant. This complicates the inverse problems, as we saw before, and the level of detail and flexibility reached with volume mesh or volume grid-based methods is never fully reacheable.

2.1.3 BEM-FEM Combination

2.1.3.1 Reported attempts and formulation

Combining the BEM and FEM is common in many areas of computational physics, such as acoustics [115, 116], electromagnetics [117, 44] and of course its "birthplace", continuum mechanics [42, 118, 119, 120, 121, 122]. However, there is not any record of the combined usage of these methods in DOT.

It is actually some of the co-inventors of the FEM, Zienkiewicz *et al*, experts in computational mechanics, who first stated a numerical formulation for the BEM-FEM combination

BEM	Link	FEM
FP Solution Search	<Elleithy *et al*'s Method [123]>	FP Solution Search
Variables' Definition	<Our Method>	Variables' Definition
Matrix Form	<Our Method>	Matrix Form
	<Sikora's Method[33]>	
Discretisation	<Sikora's Method>	Discretisation
Weak Formulation		Weak Formulation
Boundary Conditions	<Our Method>	Boundary Conditions
	<Sikora's Method>	
Local Formulation		Local Formulation

Table 2.1: BEM-FEM formulation representation showing the different links established between FEM and BEM - the higher the link, the weaker it becomes (FP: Forward Problem)

[36]. It was then applied to a number of problems in mechanics and elsewhere, as we saw in the list above. However, one will notice that almost each team of researchers invented its own BEM-FEM combination formulation and conditions. These approaches mainly differ in the level where the bound is created, either in a simple equality constraint on the values on the boundary, or a more sophisticated condition on the unknown function and its derivative on the boundary, or an iterative scheme leaving intact the matrices, etc. Sikora [33], in the beginning of his digression about the BEM-FEM combination, and Elleithy *et al* [123], in the literature review of their article, outline dozens of different formulations that we will not enumerate here. Each physical problem has different laws prevailing at the boundary, and Descartes' law of refraction (Snell's law) on an index mismatch boundary are very different from the laws applying on the boundaries of a Poiseuille flow. We will expose later (Section 3) in this thesis the chosen formulation, specific to the DOT problems, and its application.

We listed some formulations in a layered table 2.1 which represents the different levels of computation.

2.2 Optical Topography and Cortical Mapping

2.2.1 Origin of NIRS

2.2.1.1 Basic principles

It is in 1977 that Jöbsis [124] had the idea to use infrared light to have an insight on the oxygenation of vital organs. In most of the optical topography/DOCM/NIRS problems, the quantity which is monitored is the Hemoglobin/Total Hemoglobin ratio (HbO_2/Hb_{total}) or the Deoxy-Hemoglobin/Total Hemoglobin ratio closely related to the absorption coefficient. Some researchers also use different metrics and compute the actual concentrations of HbO_2 and HHb. It gives an insight on the oxygenation and can indirectly measure the activation of a region. This

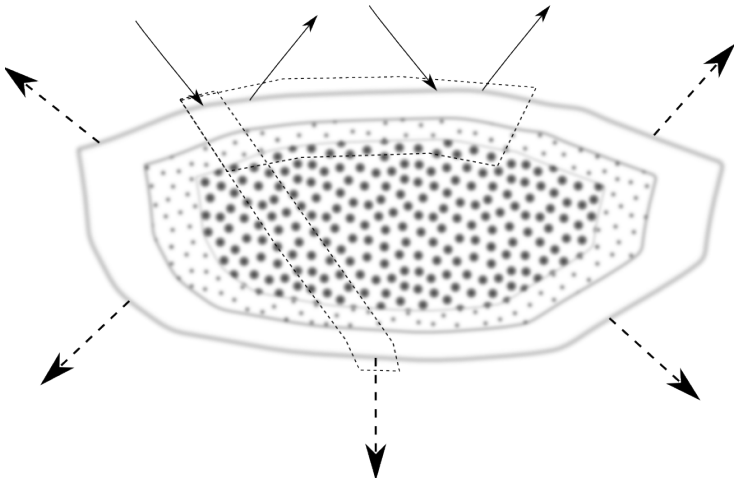

Figure 2.2: The difference between tomography and topography: tomography considers slices (from the Greek *tomos*, "section") like the one which goes accross the layers while topography (from the Greek *topos*, "place") refers to the mapping of a surface

technique should not be confused with the diffuse optical tomography we have spoken about so far (see Figure 2.2).

The technique is called spectroscopy because of the fact that this ratio cannot be determined by a measurement at a single wavelength. In fact, as depicted in Figure 1.2, finding these variables requires the computation of the absorption of the investigated tissue at two wavelengths at least. This procedure also allows to reduce the scattering effects [125]. The link between the attenuation in a measurement ΔA, a change in the absorption coefficient $\Delta\mu_a$, and changes in the concentration of chromophores was established later by Delpy *et al* [126] from a Beer-Lambert law. They called this expression the modified Beer-Lambert law:

$$\Delta\mu_a = \frac{\Delta A \times ln10}{\rho \times DPF} = \varepsilon\Delta\mathbf{C} \tag{2.2}$$

where ρ represents the distance between the detector and the source, Differential Pathlength Factor (DPF) represents the derivative of the attenuation by the absorption coefficient (estimated by simulation), ε is the matrix of the specific absorption coefficients for each chromophore at the different wavelengths and $\Delta\mathbf{C}$ is the vector of chromophore concentration changes. When possible, the DPF can also be derived from time domain measurements [127]. This method can be extended to more than two layers (the DPF becomes the Partial Differential Pathlength (PDP) [63]) and the number of measurements to take increases with the number of layers added to the model. Such considerations allow the use of the continuous wave instruments to find the oxygenation ratio in tissue. They have the advantages of having a very fast response time below 1s [128] and have less motion restriction than the devices as the one used for the experiments in

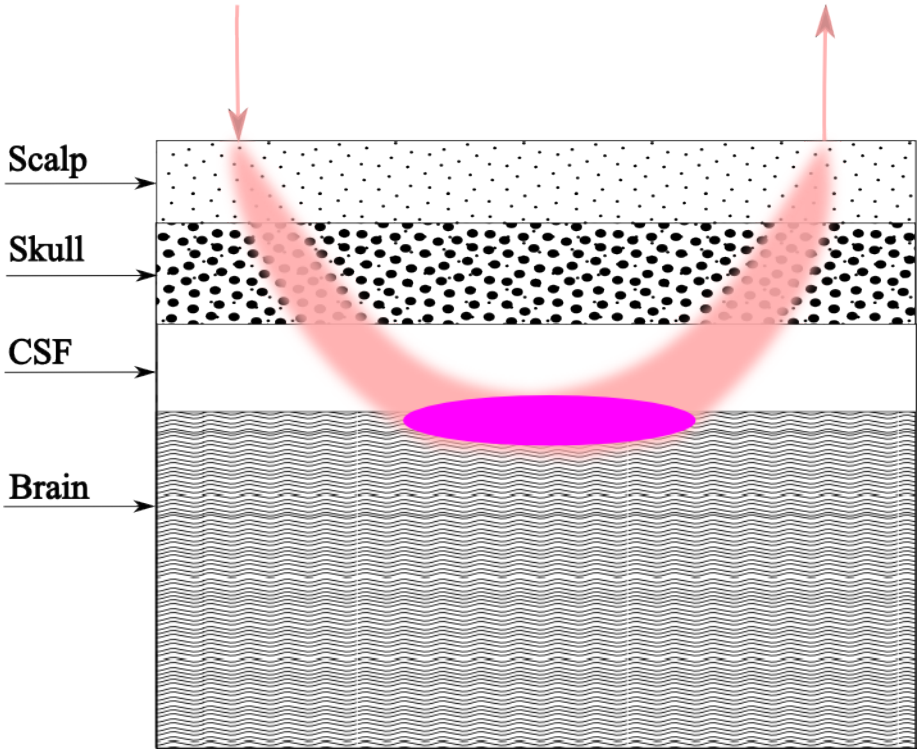

Figure 2.3: Penetration of a measurement in pink with the probed area of the cortex in purple - this is inspired from the findings of [5]

this thesis (time domain). They are currently the most readily available commercially and very large versions of them with multiple source-detector couples exist [129, 130, 131].

Other methods of computing the absorption, hence the oxygenation, have been developed [132] and another one will be described later in subsection 2.2.1.3. It is even possible, with sophisticated optimization techniques and spatially resolved spectroscopy, to obtain the scaled absorption and oxygenation in the tissues investigated [133, 134, 135].

There are actually no standard approaches for the analysis of functional Near Infra-Red Spectroscopy (fNIRS) data [125].

2.2.1.2 The particular case of the brain

Most of the current efforts in fNIRS are concentrated on the adult brain. Usually, an array of sources and detectors emitting NIR light at levels of 5-10 mW [64] are applied. The brain of an adult human, when probed with a NIR device, is thought to behave like a multi-layered slab [5] (see Figure 2.3). Due to the optical properties of the latter, particularly due to the presence of a CSF layer, the light cannot reach deeper than 5-10mm according to some [136, 61] (see subsection 2.1.1.3).

The models used are mainly linear, like the modified Beer-Lambert law and the results of the reconstruction depend strongly on the model. Errors of 5 to 11% on the absorption

coefficient can be introduced by the uncertainty on the thickness of the upper layer [137] (in a two-layered model, it represents the skull/scalp extracerebral layer). When the thickness of this layer increases or the source-detector distance increases, the spatial resolution decreases linearly but the contrast falls exponentially [136, 138]. A good review of the optical parameters assigned to these layers can be found in [139].

Part of the solution is usually found with the input of a very sophisticated technique, most commonly a Monte-Carlo based method (examples: [140, 61, 141]), to compute a few key parameters, such as the PDP or the Mean-Time of flight Sensitivity Factor (MTSF), the time-domain counterpart of the PDP, as we will see later. These Monte-Carlo techniques are too often poorly documented and each laboratory has his own code. Some tend to favor complicated models with a lot of layers, which do not have any biological meaning [62], some others just separate an extra-cerebral and an intra-cerebral layer [136] and a very large part of the literature, as we will see in subsection 2.2.2 considers the pathlengths as just parameters already put into a commercial machine (example: [142]). However, the most impressive results obtained so far have used alternative techniques with a multi-layered anatomical model, close to ours [64, 143].

The method has its limits and for example, the modified Beer-Lambert law, if based on two distances, remains the best method to compute the changes in absorption in the cerebral area as long as the upper layer (in a slab model) does not exceed a thickness of 1.4cm and does not thin below 0.8cm [63] which is not a large range.

In order to cope with the limitations of the CW techniques, various methods have been designed. One of the most readily available machine, the Hitachi ETG-4000 (http://www.hitachi-medical.co.jp/english/products/opt/etg4000/index.html) is able to image up to 52 channels at the same time (see [144]), enabling the CW technique to probe a larger area. However, one must bear in mind that the maps given by this machine are based on atlases and tabulated data, not on the individual subject, despite the apparent simplicity, speed and insight it is said to give into the cognitive processes [145]. A more careful usage is possible, when registering fiducials based either on the 10-20 Electro-Encephalography (EEG) system [146, 147, 148] or custom positions. MATLAB routines exist to perform such operations (http://brain.job.affrc.go.jp/wordpress/). They compute the coordinates of the probed brain in the MNI-Talairach (Montréal Neurological Institute atlas) space as stated by Singh *et al* [149] and Tsuzuki *et al* [150].

One can also simply increase the redundancy of the measurements. This is the solution chosen by Boas *et al* [151], for instance. It is also possible to increase the accuracy by using statistical methods to analyse the data, such as the Generalized Linear Model [152, 153], which considers the signal's temporal varations rather than its amplitude and is the standard analysis

method for fMRI [154], Statistical Parametric Mapping [155, 156] or the Wavelet-Minimum Length Description [157]. These methods, however interesting, will not be detailed here, because they are out of the scope of our study.

2.2.1.3 Alternative topographical methods

Time-domain optical topography Despite the fact that they are more expensive than most CW systems, a large number of time-domain imagers and other spectrometers have been developed for this [158, 159, 160, 161, 162, 163]. All these machines are able to record the arrival of photons at a picosecond level (rather than the ms of the CW systems) and are based on Time-Correlated Single-Photon Counting (TCSPC) units (see our Multichannel Opto-electronic Near-infrared System for Time-resolved Iterative Reconstruction (MONSTIR) system described in subsection 4.1.1).

One of the leading groups in this domain use a linear model derived from the modified Beer-Lambert law. H. Wabnitz and A. Steinbrink developed an analysis method based on the moments of the Temporal Point Spread Function (TPSF) [62, 164, 165, 166]. They include the mean, variance and total number of photons. More particularly, the variance of the TPSF has been proven to have a selective sensitivity to deep absorption changes and is deemed by them as being suitable for the representation of cerebral signals, while the total number of photons is sensitive to extra and intra-cerebral changes. Using moments allows to get rid of the influence of the instrument response function as well as the timing drift (for the variance).

Their analysis method extends the modified Beer-Lambert law by introducing time-dependent partial differential pathlengths computed with Monte-Carlo simulations using the RTE. However, the background optical properties are computed using an analytical expression on the averaged TPSF over time. For the absorption coefficient, they have developed a method to separate the extra-cerebral from the intra-cerebral layers [167]. Their goal is to obtain the oxygenation rate around the particular optode, not to reconstruct actual functional cortical image because they would then need more accurate values for their background optical properties. Instead, they do what is called “depth selective analysis” where the information from the moments and the time windows from the instrument are combined to observe selected layers of the head.

A. P. Gibson and C. E. Elwell’s group rather use the TOAST package to reconstruct actual images of the observed region [168]. Like the German group, a pad of sources and detectors (much smaller than the Hitachi ones) are placed on the subject’s head, and time-domain data is acquired. Then, the data is analysed with a tomography package, which, because of the flatness of the pad, cannot provide accurate depth resolution but can produce 2D images. The model of

the section of the head under investigation is a multi-layered slab such as in [63].

There exists an intimate link between the time domain and phase measurements (described in section 4.1.1), not only because having the former implies having the latter through a Fourier transform, but also because the phase shift is linearly related to the mean optical path length [169].

Anatomy-based or mixed modalities The most sophisticated methods of analysis include data from other modalities, mostly MRI. We will particularly see that, in our case, the phantom studies in section 7.3 use data from X-Ray CT while our in vivo experiment (section 7.4) uses an atlas mesh built from MRI data.

As far as accuracy is concerned, the best studies so far have relied on MRI-derived data and analysis methods. Abdelnour *et al* [64, 170], for example, have used a Finite Element Method (FEM) model for the propagation of light through tissue in a biologically accurate 5 tissue types model of the head. The fidelity to the anatomical features was ensured by the use of a well-known MRI tool, Freesurfer [171] which contains an atlas of the adult head. However, since the FEM gives a volume solution, the surface one has to be extracted in order to perform actual DOCM. Our model aims to simplify a similar process by integrating the photon density on the volume within the model itself. The solution that it outputs is a surface density. Another example of this combination is found in a study by Y. Tong and B. Frederick [172] where the fMRI analysis tools have been used with the Blood-Oxygen-Level Dependent (BOLD) signal being replaced by the fNIRS data. Studies by Custo *et al* [173] and Caffini *et al* [174] also show the successful use of MRI-derived data for the geometry of the adult head in a similar context.

It is also possible to simply co-register MRI and optical data as is often done with interpolated oxygenation maps [175, 176, 142]. We will see later why this is easily criticable.

EEG is also a popular method to associate with fNIRS. Its 10-20 system allows to register the NIRS data to the brain without the help of any anatomical measurement. Some commercial machines, such as the Hitachi one mentioned before have an embedded parallel EEG recording board and use this correspondence to register the NIRS on their atlas. In addition to the frequent allusions to the 10-20 positions in the NIRS articles, one can find many studies where the methods have been explicitly practically combined [177, 178, 179, 180].

2.2.1.4 Criticism

This part is strongly inspired by a very comprehensive review by Y. Hoshi [125].

Chromophores When we look at the full picture, in a biological tissue, it is actually not only the hemoglobin which produces the absorption signal observed, but rather a collection of molecules (water, lipids, some proteins, melanin, collagen, etc.). Some consider that HHb, HbO_2 and

H_2O are the main chromophores and should be included in the computation, a consideration which leads to changes in the final value of the oxygenation, as reported by Leung *et al* [133]. Some others [125] see the $CytOx$ (cytochrome C oxidase) and Mb (myoglobin) as being the contributors to consider alongside the hemoglobin. Particularly, the oxidation status of the $CytOx$ has been found to correlate with estimated changes in cerebral oxygen delivery [181]. Moreover, this chromophore is also less susceptible to extra-cerebral contamination [182]. Its disadvantage is that its redox state only changes under severe hypoxic conditions [183]. In our study, only the absorption coefficient will be computed, but these assessments emphasize the fact that a more complete theory for the interpretation of the NIRS signal is needed.

Localization of the sampled region This matter is apparently the subject of intense debates, since the different publications do not agree with each other as we have seen with the size of the layers over the investigated region (see subsection 2.1.1.3). Okada *et al* [5] have clearly demonstrated that the region lies within the cortex and not beyond, providing normal thicknesses for the layers, even if the CSF is present. However, the contamination of the NIRS signal by extracerebral sources, particularly coming from the physiological (non-cerebral) response to any movement or emotion supposed to be imaged in the cortex [184, 185, 186, 187]. Evidence has been brought forward to argue that a method is more sensitive to intracranial signals than the other. The variance of the TPSF is said to be mostly sensitive to intra-cerebral activation [62, 166]. Some others just increase the number of optodes and/or put wider gaps between them to separate the signals, but they have not been proven right [130, 131]. It is also argued that spatially resolved spectroscopy has a high sensitivity to intra-cranial changes [188]. Statistical techniques can as well have an impact on the localization of the change monitored [189].

Quantification of the investigated variable/comparison between experiments Despite some claims that the fNIRS and the fMRI can be compared [190], it has been proven many times that the NIRS signal quantitative accuracy is highly unreliable. There is, in particular, no quantitative link between the BOLD signal and the NIRS one [191, 192].

In addition to this, most of the time, the DPF (or any related quantity) is supposed to be constant in the experiment, especially between different source-detector pairs. This is actually wrong [126, 125], and, particularly in the case of CW measurements, it is not possible to compare the amplitude of data and to give any insight on the absolute value of the investigated variable.

Even time domain and frequency domain measurements, which are looking at the optical path length, cannot actually detect transient local signals which do not modify it. Actually, the ratio of the partial path length (part of the path followed by a photon which is in the cortex) to the

mean total path length varies with every measurement [193] and this makes the concentration changes being always under-estimated.

The absorption coefficient change computed in a NIRS experiment can also be challenged, since the measured quantity is partial [194, 165]. Its value is always lower than what it should be [195], due to the partial volume effect arising from the focal nature of a NIRS measurement [196, 192].

Conventional interpolation based approach The shortcut taken by many research groups, such as Ye's [156], Takeuchi's [142], etc. [175, 176, 197], to interpolate the values computed between measurements to create brain maps is dangerous. No theory of diffuse optical imaging can justify such a move, since the definition of the scattering forbids such a computation. It is much more prudent, when no proper 3D modelling of the diffusion events is available to draw maps without interpolation like in [143] where the positions of the optodes are just lit, without any interpolated values in between.

Despite all this criticism, the fNIRS has been proven to be a reliable technique when compared to modalities which are better understood, like PET [198, 199, 200] or fMRI [201, 202]. It has also found applications in many domains, from medicine to psychology. Even the DOT, on which much of this report discusses, is coming from a deeper understanding of the NIRS techniques.

2.2.2 Current applications of NIRS

For psychologists/neurophysiologists Despite the fact that it is impossible to compare two CW measurements and that many assumptions made to develop the commercially available NIRS devices, many studies have been made on high cognitive processes using the NIRS. It actually provides a relatively cheap (cheaper than the fMRI) way of investigating phenomenon which are difficult to detect (or interpret). The areas of observation include:

- Mental illnesses: [203, 204]
- Developmental psychology: [205, 206, 175, 207, 208]
- Linguistics: [209, 210, 211]
- Other cognitive processes: [212, 213, 214]

For physicians NIRS is not yet a totally reliable diagnosis instrument but it is used in a large extent by research groups to get more information about some dysfunctions in the brain. It also provides an insight into the attitude coordination and muscle-brain interaction, although the extra-cerebral signal becomes more important in such cases. A few portable devices have

been developed to enable NIRS to do what fMRI cannot, i. e. record data on the go, while the subject is walking or moving in other challenging situations [215, 216].

The areas of investigations include:

- Chirurgy: [217]
- Oxygenation monitoring: [218, 219, 220, 221]
- Pediatrics: [222, 223, 224, 225]
- Muscle-brain coordination: [226, 197, 227, 228, 215]

2.3 Acceleration methods for the BEM

The Boundary Element Method, due to the fullness of its discretized matrix has been deemed, in the DOT community, as slow and thus a secondary method compared to the FEM or other faster similar techniques such as the Kirchhoff Approximation [25, 229]. However, there exist acceleration methods for the BEM. They could allow the DOCM and potentially also the BEM-FEM to be competitive in computational time, not only in meshing ease.

We describe here the two main acceleration methods, the Adaptive Cross-Approximation (ACA) and the Fast Multipole Method (FMM). We have chosen the FMM and it is the only technique described in chapter 8.

2.3.1 ACA

The Adaptive Cross-Approximation [230, 231, 232, 233] is based on the algebraic decomposition of the BEM matrix. If the nodes are well-organized, i. e. if the node index and the distance between the nodes are correlated, the BEM matrix has a diagonal band with values far larger than at the perpendicular extremities as illustrated in [230]. This property is exploited in the technique to separate the important blocks from the large low rank matrices which are widely off-diagonal.

Central blocks are generated as-is while the off-diagonal are decomposed following a particular scheme which simplifies the computation. The expected speed improvement is very similar to what would be expected by the single-level fast multipole method we will describe later. For the fully pivoted ACA, the gain is from $O(N^3)$ [234] for the complete BEM to $O(N^2)$ for the accelerated one [232] with N being the number of degrees of liberty (in the problems presented in this report, the number of nodes).

Nevertheless, one should remember that the ACA decomposition is algebraic and does not take in account the geometry and physical properties of the system, contrary to the FMM. There

has been attempts to integrate the geometry of the problem and thus optimize the ACA, with an algorithm built for symmetrical media. Besides, the ACA is not as developed and tested as the FMM [234].

2.3.2 FMM

A breakthrough to improve the speed of the BEM technique was made by Greengard *et al* when they first described a new fast acceleration technique in their seminal paper of 1987 [235]. It was later implemented in 3D by Schmidt and Lee [236]. The FMM [237, 238, 239, 240, 235, 241, 242] consists in separating the near and far interactions and decompose the equation matrix-vector products into a sum of vectors on the unit sphere and a sparse matrix-vector product. The only remaining integrals are on the close nodes. No system matrix is computed fully explicitly, because only matrix-vector products are actually output.

The expected improvements range from an acceleration to $O(N^{\frac{3}{2}})$ operations for the single-level FMM to the maximum acceleration possible for the BEM which is $O(Nlog(N))$ for the multi-level FMM.

2.4 Hypotheses: forward model improvement

My Ph.D. is focusing on a novel approach for the forward model, using a combined BEM-FEM and a BEM DOCM scheme. The justification and detailed explanation of the method's content is provided in the following chapters of the thesis. We also show improvements to the existing BEM technique through the completion of the development of a single-level FMM.

All these quoted techniques have no precedent usage record in the DOI/DOT field. They actually all come from Continuum Mechanics [243, 36] except the FMM [235]. Their basic principles, which will be innovatively changed to fit our purposes, and the hypotheses we want to prove are outlined in the following paragraphs.

BEM-FEM (Chapters 3 - 6)

Our first hypothesis is that the BEM-FEM is a more easily accurate forward model method than the existing FEM while still being very versatile. It combines the meshing and adaptability of the BEM method with the reconstruction simplicity and accuracy of the FEM. Its worth is proven in this thesis through a large number of benchmark results. We first assess the effect of the presence of the FEM part of the problem on the BEM-FEM results by comparing them with an analytical solution in some simple cases. We then test the script on numerous meshes and complex geometrical configurations representing some of the major DOT's areas of investigation.

The second part of our tests is based on previous publications of our research group. They

are done on two experiments, one with a multi-layered phantom and the other with data from an *in vivo* experiment. All the reconstructions in this thesis are done using a linear single-step approach with assumed background optical properties for the layers.

BEM DOCM (Chapter 7)

The second hypothesis is that using the BEM eases the reconstruction of cortical maps from optical data and anatomical information. We believe that this new method allows a better interpretation of the experiments compared to the existing interpolations methods. This should be particularly visible in the localization accuracy. We also show its usage in simulated, phantom and *in vivo* contexts. The simulation highlights the integration-based nature of the technique, by showing its intimate link with the characteristics of the measurements, more particularly the Photon Measurement Density Function (PMDF). The phantom and *in vivo* results, though based on the same data than the previous technique, highlight different aspects. They also show the accuracy of the method.

BEM Acceleration (Chapter 8)

Our third and last hypothesis is that the FMM is adaptable to optical imaging, despite the challenges brought by the introduction of a significantly imaginary wave number.

The FMM's background is described in details in this thesis. Through a clustering of the elements of the surface mesh and some mathematical scheme to reduce the number of operations to perform, a significant speed improvement is achieved. The adaptation of the FMM to the Diffusion Equation (DE) is not straightforward. It requires us to return to the basic principles and explain the whole decomposition. After the description, speed tests are performed on various geometries.

A simplified BEM code able to handle experimentally available sources is also associated to it in order to further accelerate the method. It is only used to illustrate the FMM and no reconstruction is performed.

Chapter 3

BEM-FEM Theory and Numerical Problem Formulation

Principle of the method In this chapter, we will start by describing the Diffusion Approximation, then the BEM and FEM we intend to use throughout my thesis. Then, we will explain how we bind them together by making the intrinsic relationship between the energy density and the flux of photons coming partly from the BEM and partly from the FEM computation. The original idea was suggested in an unpublished note by S. Arridge [244], from which most of this chapter is inspired.

3.1 Diffuse Optical Imaging framework

We are now going to establish in an heuristic way the complete standard model which governs all scattering problems, from optics to thermics, or astrophysics or meteorology: the RTE. It was established in its modern form by S. Chandrashekhar [245].

Let's consider an arbitrary diffusive volume in which an electromagnetic light wave passes (see Figure 3.1). The radiative energy balance on this volume is the following, taking care of each individual term and without approximations:

- Input and intrinsic energy:
  - entry of photons and transport of the directional energy density
  - internal sources
  - incoming scattered photons
- Output and losses
  - absorption
  - scattered photons from the inside going outside the volume

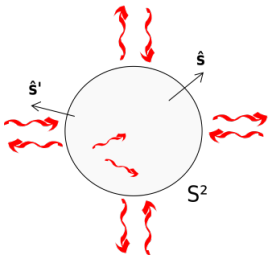

Figure 3.1: Sketch of a unit sphere of scattering volume described when writing the energy density balance equation (RTE 3.1)

One can then write the following radiative energy balance equation (temporal form):

$$\left(\frac{1}{c}\frac{\partial}{\partial t}+\hat{\mathbf{s}}\cdot\nabla+\mu_{tr}(\mathbf{r})\right)\phi(\mathbf{r},\hat{\mathbf{s}},t)=\mu_s(\mathbf{r})\int_{S^2}\Theta(\hat{\mathbf{s}},\hat{\mathbf{s}}')\phi(\mathbf{r}',\hat{\mathbf{s}}',t)dS(\mathbf{r})+q(\mathbf{r},\hat{\mathbf{s}},t) \tag{3.1}$$

This equation is the RTE, with:

- c: speed of light (in $m\cdot s^{-1}$)
- t: time (in s)
- $\hat{\mathbf{s}}$: vector on the considered unit sphere S^2, taken in the point where the photon density is computed
- $\phi(\mathbf{r},\hat{\mathbf{s}},t)$: density of photons passing through the point at position $\mathbf{r}$ going along the direction $\hat{\mathbf{s}}$ at time t (in $W\cdot m^{-2}$)
- S^2: unit sphere
- $\hat{\mathbf{s}}'$: other normal vectors on S^2
- μ_{tr}: transport coefficient (sum of μ_a and μ_s, in m^{-1})
- Θ: phase function determining the way the photons are scattered (example: tells about the directionality) - the anisotropy parameter g that we define in our diffusion model is actually the first order approximation of Θ
- q: internal source (in $W\cdot m^{-3}$)

To actually be able to write the diffusion approximation equation, one needs to pass through many simplification steps.

If we decompose the equation's solution on a basis of spherical harmonics [2], and take in account only the zeroth and first order of these functions, we make the assumption that

the radiance is quasi-isotropic (we do not discuss here the anisotropic diffusion equation). This approximation is also called the P1 approximation of the RTE. It leads us to this set of equations, with q_0 isotropic and $\mathbf{q_1}$anisotropic components of the sources:

$$(\frac{1}{c}\frac{\partial}{\partial t}+\mu_a(\mathbf{r}))\Phi(\mathbf{r},t)+\nabla\cdot\mathbf{J}(\mathbf{r},t)=q_0(\mathbf{r},t) \tag{3.2}$$

$$(\frac{1}{c}\frac{\partial}{\partial t}+\frac{1}{3D})\mathbf{J}(\mathbf{r},t)+\frac{1}{3}\nabla\Phi(\mathbf{r},t)=\mathbf{q_1}(\mathbf{r},t) \tag{3.3}$$

with

$$D=\frac{1}{3(\mu_a+\mu_s(1-g))} \tag{3.4}$$

diffusion coefficient, which comprises the anisotropy effects, at the first order of the phase function,

$$\mathbf{J}=\int_{S^2}\hat{\mathbf{s}}\phi(\mathbf{r},\hat{\mathbf{s}},t)dS \tag{3.5}$$

photon current and

$$\Phi(\mathbf{r},t)=\int_{S^2}\phi(\mathbf{r},\hat{\mathbf{s}},t)dS \tag{3.6}$$

photon density.

Then, we consider that the sources present in the medium, if any, emit an isotropic way ($\mathbf{q_1}=0$) and that the non-stationary variation of the radiative flux is negligible before the energy density gradient, i. e. that the transport length $l_{tr}=3D$ is lower than the flux's characteristic variation length. We could consider the anisotropic effects in the diffusion approximation framework itself by defining a diffusion tensor instead of a diffusion coefficient. This approach has not been developed in my work, but Heino *et al* detail it in their 2003 publication [246].

All the approximations outlined before lead us to write these basic equations:

Steady-state

$$\mathbf{J}(\mathbf{r})=-D\nabla\Phi(\mathbf{r}) \tag{3.7}$$

$$-\nabla\cdot D\nabla\Phi(\mathbf{r})+\mu_a\Phi(\mathbf{r})=q_0(\mathbf{r}) \tag{3.8}$$

Time-domain

$$\mathbf{J}(\mathbf{r},t) = -D\nabla\Phi(\mathbf{r},t) \tag{3.9}$$

$$-\nabla\cdot D\nabla\Phi(\mathbf{r},t) + \mu_a\Phi(\mathbf{r},t) + \frac{1}{c}\frac{\partial\Phi(\mathbf{r},t)}{\partial t} = q_0(\mathbf{r},t) \tag{3.10}$$

Frequency-domain

$$\mathbf{J}(\mathbf{r},\omega) = -D\nabla\Phi(\mathbf{r},\omega) \tag{3.11}$$

$$-\nabla\cdot D\nabla\Phi(\mathbf{r},\omega) + (\mu_a + \frac{\imath\omega}{c})\Phi(\mathbf{r},\omega) = q_0(\mathbf{r},\omega) \tag{3.12}$$

In most of the following, only the frequency-domain formulation will be used. It is mainly because this type of data is easier to handle and yields sufficient information for our study. More considerations for choosing this modality rather than the historical time-domain for clinical applications especially are explained in [247, 248]. There is also consistently more noise in time-domain data, especially since it explores a larger frequency band (up to several GHz) than the frequency-domain data (the sources cannot be modulated at such frequencies with the current technology). However, one should remember that the time-domain measurement data, the TPSF (see subsection 4.1.1) has a higher information content than the amplitude and phase data coming from a frequency domain approach [125].

Speaking about the steady-state equation, the information drawn out of such experiments have been proven insufficient for the reconstruction of both the scattering and absorption coefficients simultaneously [73].

Boundary conditions - Milne's problem To properly implement the diffusion approximation, we realize that we need to introduce an additional parameter. As we have seen above, the diffusion approximation is only applicable at "large" distances (the transport length has to be larger than the light beam's characteristic variation length) within the scattering medium, a condition which is definitely not satisfied on the boundary. Nonetheless, we know that only the surface is imaged. It means that, since the raw solution is not acceptable on the surface, we need to somehow "force" the solution to be accurate there while staying in this diffusion theory framework.

One can actually find a simple solution to this problem which bears E. Milne's name with a Robin-type boundary condition: defining an *extrapolation coefficient* z_e on each point of the surface, i. e. an extrapolated surface (at a distance $l_{ext} = 2z_eD$, the extrapolation length of the actual surface) on which the solution would converge to zero [249, 250]. This length can be defined through many less approximated means. For example, one can solve the RTE on a

simple geometry: the semi-infinite diffusive medium. This z_e then allows the solution of the diffusion approximation to fit the RTE's solution on the surface. An example of this approach is given in an article by Kienle [251]. The other way to solve Milne's problem, is the definition of a relationship between the radiative flux and the energy density, both being computed when solving the diffusion approximation problem on the surface:

$$[\Phi + 2z_e \hat{\nu} \cdot \mathbf{J}]_\Gamma = 0 \tag{3.13}$$

$\hat{\nu}$ here represents the normal vector on the considered point on the surface Γ. Popescu *et al* [252] show the correspondence between the two approaches, as stated in the above formula 3.13.

Detailed computations of the extrapolation length can be found in articles by Contini *et al* [253] and by Case and Zweifel in a more general radiative transport context [254]. In fact, it depends on the mismatch between the refraction indices of the two media surrounding the interface. In the rest of this study, the refraction index will be considered constant everywhere and equal to that of the vacuum.

In summary, the extrapolation length's usage is two-fold:

It is defines a necessary but virtual entity, the extrapolated surface on which the energy density is zero in the framework of the diffusion approximation.

It defines also a zone in which the singularity of Green's function is manageable. For example, in the case of the spheres described in section 5.1, the point sources were not put exactly on the outer sphere but slightly inside it, at a distance from the surface which is of the order of magnitude of the extrapolation length. This problem does not occur with the Gaussian sources, since the highest frequencies of Green's function are not taken in account in the inverse Fourier transform (see subsection 4.1.2).

3.2 Collocation Boundary Element Method formulation

3.2.1 Integral equations (frequency-domain)

We divide the scattering domain Ω into a piecewise uniform collection of volumes $\Omega_i,\ 0 \leq i \leq n_\Omega$, with Ω_0 being the outermost one. Interfaces between subdomains define surfaces $\Gamma_i,\ 0 \leq i \leq n_\Gamma$ with Γ_0 the outer domain boundary (see Figure 3.2). A given surface Γ_j for $j > 0$ is the interface between two subdomains Ω_{j+} and Ω_{j-}. The closed boundary of a subdomain is given by a set of surfaces $\partial\Omega_i = \cup_{j \in \mathbb{B}_i} \Gamma_j$ where $\mathbb{B}_i$ is the index of surfaces that comprise the boundary of Ω_i.

We define the wave number in each subdomain as such:

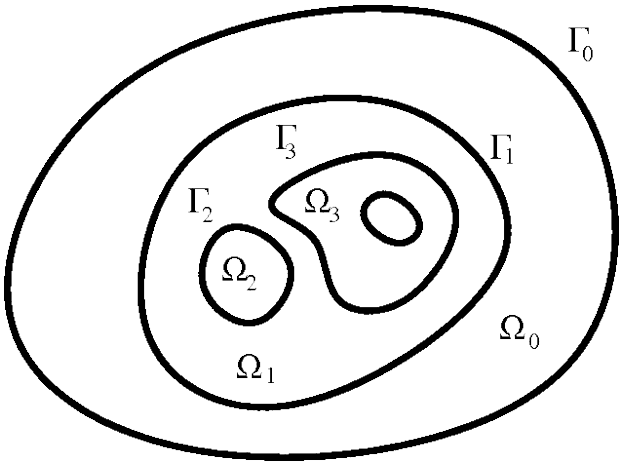

Figure 3.2: Division of the diffusive domain Ω in subregions Ω_i

$$\varpi_i = \left(\frac{\mu_{a,i} + \frac{\iota\omega}{c}}{D_i}\right)^{\frac{1}{2}} \; with\ here\ \iota^2 = -1 \tag{3.14}$$

where the square root is taken with a positive real part to ensure physically realistic asymptotic behaviour.

We define Green's functions for each subdomain as solutions of the point source problem in an infinite medium which has the subdomain's optical parameters:

$$\triangle G_i(\mathbf{r},\mathbf{r}';\omega) - \varpi_i^2 G_i(\mathbf{r},\mathbf{r}';\omega) = -\delta(\mathbf{r}-\mathbf{r}') \; with\ G_i(\mathbf{r},\mathbf{r}';\omega)|_{|\mathbf{r}|\to\infty} = 0$$

$$\Rightarrow G_i(\mathbf{r},\mathbf{r}';\omega) = \frac{1}{4\pi}\frac{e^{-\varpi_i|\mathbf{r}-\mathbf{r}'|}}{|\mathbf{r}-\mathbf{r}'|} \tag{3.15}$$

The diffusion equation (3.3) and Milne's boundary condition (3.13 and [252]) are enforced in the volume and at the surface of each individual subdomain.

To simplify the BEM equations we adopt a similar notation to [24] and define:

- ϕ_i: solution of the diffusion equation within the subdomain Ω_i
- Q_i: source in subdomain Ω_i
- q_i: source on the surface convolved with Green's function G_i
- l_e: extrapolation length
- U_j: density ϕ restricted to surface Γ_j
- V_j: normal current $\hat{\nu}_i \cdot \mathbf{J}$ restricted to Γ_j

- $\hat{\nu}_j$: normal vector to Γ_j

Milne's boundary condition is then written on the outer subdomain which is only surrounded by the air:

$$U_0 + l_e V_0 = J^- \tag{3.16}$$

where J^- is an incoming flux.

When we apply Green's second theorem to subdomain Ω_i assuming that the boundary of this domain consists of surfaces Γ_j and $\Gamma_{j'}$, we obtain the following:

$$\begin{aligned}\phi_i(\mathbf{r}) = &\int_{\Gamma_j} \frac{G_i(\mathbf{r},\mathbf{r}')}{D_i} V_j(\mathbf{r}') - \partial_j G_i(\mathbf{r},\mathbf{r}') U_j(\mathbf{r}') dS_j(\mathbf{r}') \\ &- \int_{\Gamma_{j'}} \frac{G_i(\mathbf{r},\mathbf{r}')}{D_i} V_{j'}(\mathbf{r}') - \partial_{j'} G_i(\mathbf{r},\mathbf{r}') U_{j'}(\mathbf{r}') dS_{j'}(\mathbf{r}') \\ &+ \int_{\Omega_i} G_i(\mathbf{r},\mathbf{r}') Q_i(\mathbf{r}') d^3\mathbf{r}'\end{aligned} \tag{3.17}$$

where we used the notation $\partial_i := \hat{\nu}_i \cdot \nabla$ for brevity.

The boundary integral equations are then obtained when $\mathbf{r}'$ approaches Γ_i or any inner surface to the subdomain Ω_i.

We define the following operators mapping functions on $\Gamma_{j'}$, to functions on Γ_j with $j, j' \in \mathbb{B}_i$:

$$\mathscr{A}^{(i)}_{j,j'} U = \int_{\Gamma_{j'}} \partial_{j'} G_i(\mathbf{r}_j, \mathbf{r}'_{j'}) U(\mathbf{r}'_{j'}) dS(\mathbf{r}'_{j'}), \tag{3.18}$$

$$\mathscr{B}^{(i)}_{j,j'} V = \int_{\Gamma_{j'}} \frac{G_i(\mathbf{r}_j, \mathbf{r}'_{j'})}{D_i} V(\mathbf{r}'_{j'}) dS(\mathbf{r}'_{j'}). \tag{3.19}$$

Let us use the properties of the layer potential operators [255, 256] to handle singularities that occur due to the nature of the Green's function eq.(3.15) and consider the limits as $\mathbf{r}$ approaches Γ_i from each side of the interface. Each surface Γ_j, $j > 0$ gives rise to two equations which we write as:

$$\frac{1}{2} U_j + \sum_{j' \in \mathbb{B}_{j+}} s_{j'} \left(\mathscr{B}^{(j+)}_{j,j'} V_{j'} - \mathscr{A}^{(j+)}_{j,j'} U_{j'} \right) = 0 \tag{3.20}$$

and this equation when $\mathbf{r}$ approaches the boundary Γ_j from the outside:

$$\frac{1}{2} U_j - \sum_{j' \in \mathbb{B}_{j-}} s_{j'} \left(\mathscr{B}^{(j-)}_{j,j'} V_{j'} - \mathscr{A}^{(j-)}_{j,j'} U_{j'} \right) = 0 \tag{3.21}$$

where $s_j = \pm 1$ is an indicator as to whether $\hat{\nu}_j$ points into or out of region $\Omega_{j\pm}$. Using eq.(3.16)

to eliminate V_0 results in $2n_\Gamma - 1$ Boundary Integral Equation (BIE) as detailed in [24].

One notices that eq.(3.20) and eq.(3.21) present singular integrals, due to the form taken by Green's function. The factor $\frac{1}{2}$ arises due to the method by which the singularities are removed. It has been calculated [113, 257, 33, 256] for smooth boundaries and thanks to simple physical considerations, adding a new constraint for the BEM-treated volumes. In fact, for the sharp corners, other values exist depending on their nature [33].

3.2.2 Discrete system and numerical implementation

The discrete BEM system is obtained from the BIE by choosing a basis representation for the functions U_i and V_i, and an observation set for the layer potential functions. Following [24], we use a piecewise polynomial basis for U_i, V_i defined on the surfaces Γ_i and a collocation method for the observation set. Each surface Γ_j is discretised by n_j vertices $\mathbf{N}_{j,k}; k = 1...n_j$, with U_j and V_j approximated by the nodal basis functions $\{u_{j,k}\}$:

$$U_j(\mathbf{r}) \approx \sum_{k'=1}^{n_j} U_{j,k'} u_{j,k'}(\mathbf{r}), \quad V_j \approx \sum_{k'=1}^{n_j} V_{j,k'} u_{j,k'}(\vec{r}) \tag{3.22}$$

The discretisation of the operators (3.18) and (3.19) leads to $n_j \times n_{j'}$ dense matrices $A^{(i)}_{jj'}$, $B^{(i)}_{jj'}$, with entries

$$A^{(i)}_{jj'}(k,k') = \int_{\Gamma_{j'}} \delta(\mathbf{N}_{j,k}) \mathscr{A}^{(i)}_{j,j'} u_{j',k'} dS_{j'}, \tag{3.23}$$

$$B^{(i)}_{jj'}(k,k') = \int_{\Gamma_{j'}} \delta(\mathbf{N}_{j,k}), \mathscr{B}^{(i)}_{j,j'} u_{j',k'} dS_{j'} \tag{3.24}$$

with $k' \in 1...n_{j'}$ and $k \in 1...n_j$.

In the actual implementation, the basis functions are quadratic, and the singular integrals are treated as described in [9].

Writing $f_0 = U_0$, $f_j = \begin{pmatrix} U_j \\ V_j \end{pmatrix}$ we can write the BEM system in matrix form as:

$$\begin{pmatrix} K_{00} & K_{01} & 0 & \dots & 0 & \dots & 0 & 0 \\ K_{10} & K_{11} & K_{12} & \dots & 0 & \dots & 0 & 0 \\ \vdots & \vdots & \vdots & \ddots & \dots & \dots & 0 & 0 \\ 0 & 0 & 0 & \dots & K_{jj'} & \dots & 0 & 0 \\ \vdots & \vdots & \vdots & \dots & \dots & \ddots & 0 & 0 \\ 0 & 0 & 0 & \dots & \dots & \dots & K_{n_\Gamma n_{\Gamma-1}} & K_{n_\Gamma n_\Gamma} \end{pmatrix} \begin{pmatrix} f_0 \\ f_1 \\ f_2 \\ \vdots \\ f_j \\ \vdots \\ f_{n_{\Gamma-1}} \\ f_{n_\Gamma} \end{pmatrix} = \begin{pmatrix} q_0 \\ 0 \\ 0 \\ \vdots \\ 0 \\ \vdots \\ 0 \\ 0 \end{pmatrix} \tag{3.25}$$

For $j > 0$ the diagonal blocks take the form

$$K_{jj} = \begin{pmatrix} \frac{1}{2}\mathbb{I} - s_j A_{jj}^{(j+)} & s_j B_{jj}^{(j+)} \\ \frac{1}{2}\mathbb{I} + s_j A_{jj}^{(j-)} & -s_j B_{jj}^{(j-)} \end{pmatrix} \tag{3.26}$$

and the off-diagonal blocks take the form

$$K_{jj'} = \begin{cases} \begin{pmatrix} -s_{j'} A_{jj'}^{(j+)} & s_{j'} B_{jj'}^{(j+)} \\ 0 & 0 \end{pmatrix} & j, j' \in \mathbb{B}_{j+} \\ \begin{pmatrix} 0 & 0 \\ s_{j'} A_{jj'}^{(j-)} & -s_{j'} B_{jj'}^{(j-)} \end{pmatrix} & j, j' \in \mathbb{B}_{j-} \\ 0 & \text{otherwise.} \end{cases} \tag{3.27}$$

Making use of eq.(3.16) to eliminate V_0 we have the particular cases

$$K_{00} = \frac{1}{2}\mathsf{I} + A_{00}^{(0)} + \frac{1}{l_e} B_{00}^{(0)}, \tag{3.28}$$

$$K_{01} = \begin{pmatrix} -A_{01}^{(0)} & B_{01}^{(0)} \end{pmatrix}, \tag{3.29}$$

$$K_{10} = \begin{pmatrix} A_{01}^{(0)} + \frac{1}{l_e} B_{10}^{(0)} \\ 0 \end{pmatrix}. \tag{3.30}$$

We will not investigate the case of Galerkin BEM, for this thesis does not involve any re-writing of this part of the forward problem, even if the next formulation, the FEM part, is a Galerkin FEM.

3.3 Galerkin Finite Element Method formulation

We first summarize the FEM solution to eq.(3.12). We consider a domain Ω divided into P_{FEM} elements $\tau_k; k = 1 \ldots P_{FEM}$with n_{FEM} nodes $\mathbf{N}_k; k = 1 \ldots n_{FEM}$, with ϕ approximated by the nodal basis functions u_k:

$$\phi(\mathbf{r};\omega) = \phi^h(\mathbf{r};\omega) \approx \sum_{k=1}^{n_{FEM}} \phi_k(\omega) u_k(\mathbf{r}). \tag{3.31}$$

For convenience, let us arrange for the first n_Γ to be located on the boundary Γ and the remaining $n_{int} = n_{FEM} - n_\Gamma$ to be on the interior of Ω.

In the Galerkin formulation, the errors resulting from using ϕ^h in place of ϕ in eq.(3.12) are made orthogonal to the n_{FEM}-dimensional Hilbert space spanned by the basis functions $\{u_k\}$. By application of the divergence theorem and using the representation of the eq.(3.31), we get the following relation:

$$\sum_{k'=1}^{n_{FEM}} K(k,k')\phi_{k'} - \int_\Gamma u_k(\mathbf{r}) D(\mathbf{r}) \hat{\nu} \cdot \nabla \phi^h(\mathbf{r};\omega) dS(\mathbf{r}) = q_k \tag{3.32}$$

where $K(k,k')$ is a matrix element of the system matrix K^{FEM} and is given by

$$K(k,k') = \int_\Omega [D(\mathbf{r}) \nabla u_k(\mathbf{r}) \cdot \nabla u_{k'}(\mathbf{r}) + \left(\mu_a(\mathbf{r}) + \frac{\imath\omega}{c}\right) u_k(\mathbf{r}) u_{k'}(\mathbf{r})] d\mathbf{r} \tag{3.33}$$

and

$$q_k = \int_\Omega u_k(\mathbf{r}) Q_0(\mathbf{r};\omega) d\mathbf{r}. \tag{3.34}$$

Using the Robin condition eq.(3.16) in eq.(3.32), we get

$$\sum_{k'=1}^{n_{FEM}} K(k,k')\phi_{k'} + \frac{1}{l_e} \sum_{k'=1}^{n_\Gamma} M(k,k')\phi_{k'} = q_k - \frac{1}{l_e} J^- \tag{3.35}$$

where $M(k,k')$ are the elements of a matrix M given by

$$M(k,k') = \int_\Gamma u_k(\mathbf{r}) u_{k'}(\mathbf{r}) dS(\mathbf{r}) \tag{3.36}$$

and

$$J_k^- = \int_\Gamma u_k(\mathbf{r}) J^-(\mathbf{r};\omega) dS(\mathbf{r}). \tag{3.37}$$

If we make use of the splitting of nodes between the interior and the boundary we can write the discrete system as:

$$\begin{pmatrix} K_{\partial\Omega\partial\Omega} + \frac{1}{l_e}M & K_{\Omega\partial\Omega} \\ K_{\Omega\partial\Omega} & K_{\Omega\Omega} \end{pmatrix} \begin{pmatrix} \phi_{\partial\Omega} \\ \phi_{\Omega} \end{pmatrix} = \begin{pmatrix} q_{\partial\Omega} + J^{-} \\ q_{\Omega} \end{pmatrix}. \tag{3.38}$$

3.4 BEM-FEM Formulation

Surface-flux condition We set these equalities coupling the FEM and the BEM on the surface of each BEM-FEM boundary subdomain:

$$\phi^{FEM}_{\partial\Omega_i}(\mathbf{r};\omega) = U^{BEM}_j(\mathbf{r};\omega), \tag{3.39}$$

$$D_i(\mathbf{r})\hat{\nu}_j \cdot \nabla\phi^{FEM}_{\partial\Omega_i}(\mathbf{r};\omega) = -V^{BEM}_j(\mathbf{r};\omega). \tag{3.40}$$

The above eq.(3.40) means that the gradient of the approximated energy density $\phi^{FEM}_{\partial\Omega_i}(\mathbf{r};\omega)$ on the inner surface (or the outer) multiplied by the diffusion coefficient and its outer normal $\hat{\nu}_j$ is equal to the inner flux coming from the volume $-V^{BEM}_j(\mathbf{r};\omega)$ (treated with BEM) surrounding (or totally surrounded by) this surface. This fundamental association of the BEM with the flux and the FEM with the energy density is a consequence of the difference existing between these schemes in the treatment of the flux. Indeed, in a volume integral-based approach, the flux can be computed only by deriving it from the energy density while in a BEM scheme, it is computed along with the energy density, as we saw in the previous sections.

Collocation BEM/Galerkin FEM matrix construction If we associate $i = j'$ for the surface $\partial\Omega_i$, we modify eq.(3.26) to

$$\tilde{K}_{jj} = \begin{pmatrix} \frac{1}{2}\mathbb{I} - s_j A^{(j+)}_{jj} & s_j B^{(j+)}_{jj} \\ K^{FEM}_{\partial\Omega\partial\Omega} & -M \end{pmatrix} \tag{3.41}$$

and eq.(3.27) similarly. Then eq.(3.25) is augmented by introducing extra variables $\phi_{i,k}; k = 1 \dots n_{int}$ to give

$$\begin{pmatrix} K_{00} & \dots & 0 & 0 & \dots \\ \vdots & \ddots & \dots & \dots & \dots \\ 0 & \dots & \tilde{K}_{jj'} & K^{FEM}_{\Gamma_{j'}\Omega_i} & \dots \\ 0 & \dots & \begin{pmatrix} K^{FEM}_{\Omega_i\Gamma_{j'}} & 0 \end{pmatrix} & K^{FEM}_{\Omega_i\Omega_i} & \dots \\ \vdots & \vdots & \vdots & \vdots & \ddots \end{pmatrix} \begin{pmatrix} f_0 \\ \vdots \\ f_{j'} \\ \phi_i \\ \vdots \end{pmatrix} = \begin{pmatrix} q_0 \\ 0 \\ \vdots \\ 0 \\ \vdots \end{pmatrix}. \tag{3.42}$$

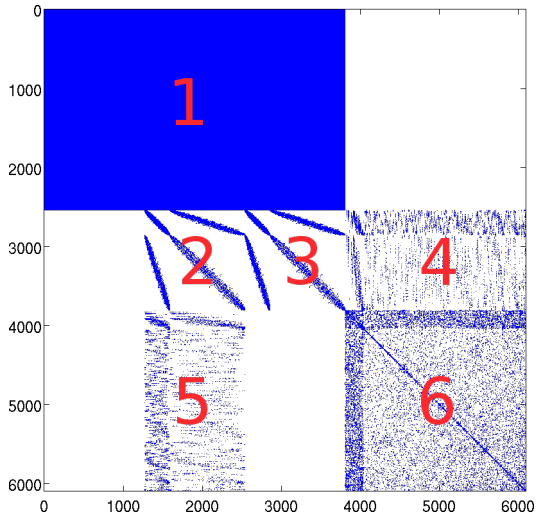

Figure 3.3: Example two layers BEM-FEM matrix occupancy plot; 1: BEM matrix for the first layer, 2: FEM matrix of the second layer's surface nodes, 3: Galerkin matrix of the second layer's surface nodes, 4 and 5: FEM matrix between the second layer's surface nodes and its inner nodes, 6: FEM matrix of the second layer's inner nodes

All matrix blocks are dense apart from the $K^{FEM}$and M matrices. Figure 3.3 shows a practical example of such a construction.

Note In the practical implementation, we sometimes eliminate the flux from the variables by taking the Schur complement [258] of the matrix. This allows us to achieve at least two goals:

- Getting rid of the ambiguity of computing the energy density and the corresponding flux (derivative) at the same point
- Reducing the size of the problem and then the computational time

For example, in two layers, the simplification is performed as in eqs.(3.43, 3.44).

$$\begin{pmatrix} A_0^{00}+\frac{1}{2}\mathbb{I}+\frac{B_0^{00}}{2D_0} & A_0^{01} & -\frac{B_0^{01}}{D_0} \\ A_0^{10}+\frac{B_0^{10}}{2D_0} & A_0^{11}+\frac{1}{2}\mathbb{I} & -\frac{B_0^{11}}{D_0} \\ 0 & A_1+\frac{1}{2}\mathbb{I} & \frac{B_1}{D_1} \end{pmatrix} \begin{pmatrix} U_0 \\ U_1 \\ V_1 \end{pmatrix} = \begin{pmatrix} Q \\ 0 \\ 0 \end{pmatrix} \tag{3.43}$$

$$\Rightarrow \begin{pmatrix} A_0^{00}+\frac{1}{2}\mathbb{I}+\frac{B_0^{00}}{2D_0} & A_0^{01}+\frac{B_0^{01}B_1^{-1}}{D_0D_1}(A_1+\frac{1}{2}\mathbb{I}) \\ A_0^{10}+\frac{B_0^{10}}{2D_0} & A_0^{11}+\frac{1}{2}\mathbb{I}+\frac{B_0^{11}B_1^{-1}}{D_0D_1}(A_1+\frac{1}{2}\mathbb{I}) \end{pmatrix} \begin{pmatrix} U_0 \\ U_1 \end{pmatrix} = \begin{pmatrix} Q \\ 0 \end{pmatrix} \tag{3.44}$$

3.5 Meshing task

The meshing task is considerably reduced with the BEM-FEM compared to a full FEM, as aforementioned in 2.1.1.4. In a DOT FEM or BEM system preparation phase, the BEM-FEM

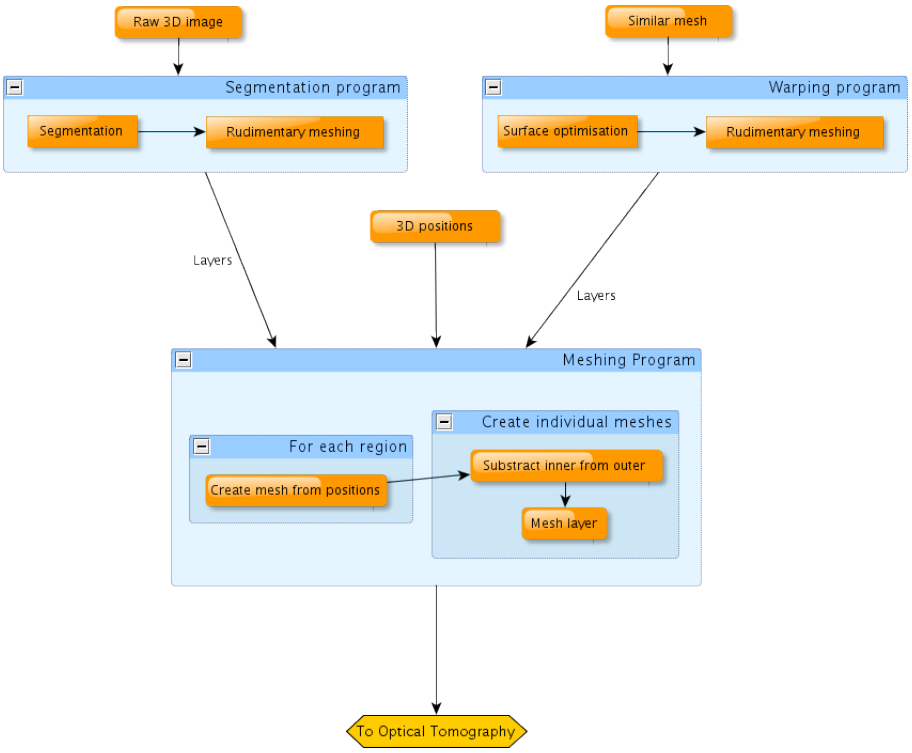

Figure 3.4: Schematic view of the meshing task associated to high resolution DOT

allows to skip some time-consuming steps. Most of the time, a high resolution DOT computation starts with some information on the diffusive media geometry coming from another modality, preferably an anatomical one, such as XCT [173, 259] or MRI [75, 260, 39]. The mesh is then built from this data using segmentation tools such as Freesurfer [171] or Brainsuite [261]. Usually, the optodes/CCD camera/sources position is also known and integrated into the computation. In the particular case of contact tomography, their position can be used to infer the geometry. In our work, as described in section 5.3.2, we took an atlas generated from MRI and warped it on the surface described by the optodes' positions before creating the meshes. The whole process is described on Figure 3.4 whose three large upper branches represent three ways of generating the meshes.

In the BEM-FEM framework, the warping is simplified since it can be applied to the surface meshes alone without a significant change in the volume-integral treated region, providing that one knows that the region of interest has a stable geometry. Warping volumes is far more complicated than warping surfaces [262, 263, 264, 265, 266].

Since some MRI-based atlases already exist for the neonatal head, we only had to generate surface and volume meshes and used the following packages:

- NETGEN [267]: for surface and volume mesh generation

- TETGEN (http://tetgen.berlios.de): for volume mesh generation

Chapter 4

Measurements and Reconstruction

This thesis is focused on improving the forward model of Diffuse Optical Tomography. This is why we will only briefly describe the reconstruction model and measurement apparatus used.

The reconstruction method has actually already been published in details, and in a more general setting, in [268]. In all our simulations and experiments, we will only consider the linear reconstructions of small targets (perturbative approach). The optical properties of the surrounding diffusing media (background properties) are deemed constant and known.

4.1 Measurements

4.1.1 Apparatus and data

All optical measurements used in this thesis are acquired through optodes (optical fibers) which are alternatively used as sources and detectors. The device used is the optical scanner MONSTIR [269]. It is a TCSPC instrumentation with 32 I/O channels.

MONSTIR's main output are the Temporal Point Spread Functions (see [126]) or histograms of the time of flight of the photons sent through the turbid media studied. They usually have the form shown in Figure 4.1. From these time-domain measurements, it is possible to obtain frequency domain data through a simple Fourier transform. The latter type of data is easier to handle. The phase shift and amplitude are derived from the complex value of the Fourier transform at the desired frequency in the Fourier domain.

4.1.2 Source model

As it can be seen in eq.(3.17), the light sources in the diffusive media, in the BEM formulation adopted here are not represented by the simple distribution of the energy density generated by them but by a convolution of this distribution with Green's function. This convolution has to be performed on all the surfaces that the source illuminates.

In the simple case of the Dirac distribution as a source, the effective term is the classic Green's function, as presented in [24]. However, in the present work, we were trying to mimic

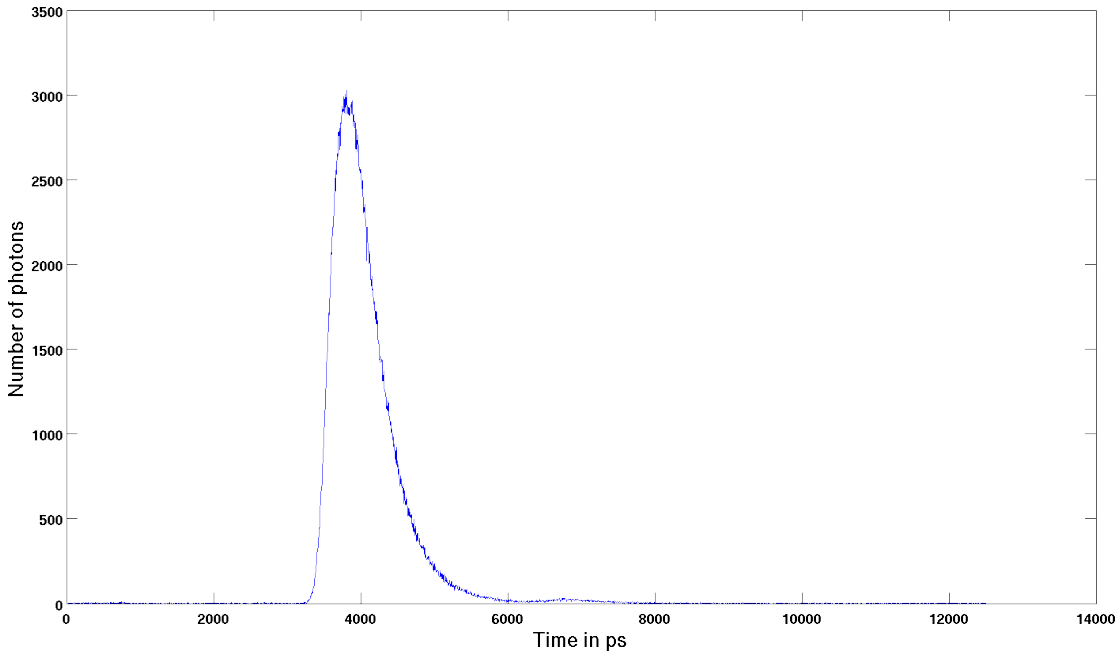

Figure 4.1: Experimental Temporal Point Spread Function

the experimental results, i.e. the optical fibers of the optical scanner MONSTIR, which we commonly modelled with Gaussian distributions (e.g. in [270]). We perform this operation in the Fourier space:

$$q_0(\mathbf{r};\omega) = \int_{\Omega_0} G_0(\mathbf{r},\mathbf{r}')Q_0(\mathbf{r}')d^3\mathbf{r}'$$

$$\Rightarrow q_0(\mathbf{r};\omega) = \hat{\mathscr{F}}(\mathscr{F}G_0(\mathbf{k}))\otimes\mathscr{F}Q_0(\mathbf{k}))) \tag{4.1}$$

providing the source is on the outer surface, as in all the experiments presented in this report. The variable $\mathbf{k}$ is here the Fourier variable and has the dimension of a wave number, although it is different from the subdomain wave number ϖ_i defined in eq.(3.14).

The expressions of the Fourier transforms are as follows:

$$\mathscr{F}G_0(\mathbf{k}) = \frac{1}{(\mu_a - \imath\frac{\omega}{c}) + D_0\mathbf{k}^2} \tag{4.2}$$

$$\mathscr{F}Q_0(\mathbf{k}) = \frac{P\sigma}{\sqrt{2\pi}}e^{-\frac{\mathbf{k}^2\sigma^2}{2}} \tag{4.3}$$

for a normalized Gaussian source of power P and width σ.

This computation, apparently simple, is not actually easy to carry out, because the mesh on which the values are computed is not a regular grid. The theory of non-uniform Fourier transform seems to be needed in this case [271]. However, we developed another way of performing the convolution. It is possible, by using detailed tables of the value of q_0 for a large

number of radii, from the simple inversion described in eq.(4.1) to the actual value of this BEM source at all points of the mesh. For each node, a value is picked in a look-up table which corresponds to the closest distance to the center of the real space. The table is generated by the inverse Fourier transform and a spline interpolation for intermediary values. This technique is simple to implement using only the existing Fast Fourier Transform (FFT) tools, providing one can create a set of evaluations of the source term at enough distances to the center of the space to give every node a sensible source value.

4.2 Reconstruction method

The difference between the resting state x_0 with set optical properties (background) and the activated state $x_1$is assumed to be linearly related to the difference in measurements y_0 and y_1 through a sensitivity matrix, the Jacobian [2, 272] W:

$$\delta y = W \delta x, \tag{4.4}$$

where x represents a vector of all optical parameters considered in the inversion, and y represents the vector of all measurements from all sources. Further, we consider the scenario in [98], wherein the change in optical parameters is considered to be in the absorption parameter only and that the measurements are the logarithmic amplitude $ln(A)$ and the phase θ of the complex valued flux J^+. This means that eq.(4.4) is now written:

$$\delta \begin{pmatrix} ln(A) \\ \theta \end{pmatrix} = W \delta \mu_a. \tag{4.5}$$

The experimental derivation of the data is obtained using a time-domain measurement system, MONSTIR [269], whose output data is Fourier transformed and sampled at a single modulation frequency [98]. To obtain the corresponding numerical model we introduce the measurement operator:

$$\begin{pmatrix} y_{d,s}^{lnA} \\ y_{d,s}^{\theta} \end{pmatrix} = \begin{pmatrix} Re \\ Im \end{pmatrix} log \mathscr{M}_d \mathbf{f}_s = \begin{pmatrix} Re \\ Im \end{pmatrix} log \mathscr{M}_d K^{-1} \mathbf{q}_s, \tag{4.6}$$

where $\mathbf{q}_s$ is the model for the s^{th} source distribution K is either the FEM or the BEM-FEM matrix, and $\mathscr{M}_d$ defines the integration of the photon current $J^+ = V_0$ over the aperture of the detector d. Since the assumption in the BEM-FEM model is that the image variation is restricted just to the domain Ω_i, we define a regular $n_x \times n_y \times n_z$ grid over the entire domain Ω and a basis $\{b_k\}$ as the set of trilinear interpolation functions with value unity on each grid point falling

within Ω_i and zero on each neighbouring point. Using these definitions, we define the Jacobian matrix as:

$$\begin{pmatrix} W^{lnA}_{ds,k} \\ W^{\theta}_{ds,k} \end{pmatrix} = \begin{pmatrix} Re \\ Im \end{pmatrix} < \frac{\phi^{+}_{\Omega_i,d}\phi_{\Omega_i,s}}{y_{d,s}}, b_k >, \tag{4.7}$$

where $\phi^{+}_{\Omega_i,d}$, $\phi_{\Omega_i,s}$ are the forward and adjoint fields within Ω_i from source s and detector d respectively.

The solution to the image reconstruction problem is considered as the solution of the linear inversion:

$$(W^T C_y W + \alpha C_x)\delta x = W C_y^T \delta y, \tag{4.8}$$

where C_y, C_x are the inverse covariance matrices of the assumed measurement noise model, and image prior distribution respectively, and α is a regularization parameter.

In this paper, we take $C_x = \mathbb{I}$ the identity matrix, which corresponds to a zero-order Tikhonov regularization scheme, and $C_y = diag[1/\overline{lnA}, 1/\overline{\theta}]$, where $\overline{lnA}$, $\overline{\theta}$ are the average initial errors in log amplitude and phase respectively [268]. Eq.(4.8) is solved using the GMRES or the Minimal Residual Method (MINRES) solvers in MATLAB with a tolerance of 10^{-6}. Regularisation parameter α is chosen using the L-curve method [273] or a derivative of it.

Restricted FEM Many times in this thesis, we will refer to a reconstruction method called "restricted FEM". This means that the reconstruction model outlined here is applied to only a fraction of the nodes of the FEM, while the others have fixed optical properties. In eq.(4.7), this is translated as ϕ referring only to the energy density field computed on these nodes. In the context of this study, they always correspond to the equivalent volume-integral treated region in the BEM-FEM, although, due to the need for a good computational accuracy, the FEM nodes are more numerous.

This operation is performed in order to ensure the comparability between the BEM-FEM and the FEM.

4.3 Alternative reconstruction techniques

Non-linear reconstruction This kind of inverse problem will not be thoroughly explained here, since it is actually not met in our research and only mentioned in this thesis.

When the evolution from the resting state x_0 to the activated state x_1 is not considered linear, the solution is obtained through an iterative process. This is actually a more general way of solving the DOT problem, since the dependency of the measurements to the optical parameters is not linear. An initial guess is first created from the information available. It can be a homogeneous background, for example. Generally, the objective function of eq.(4.9) with

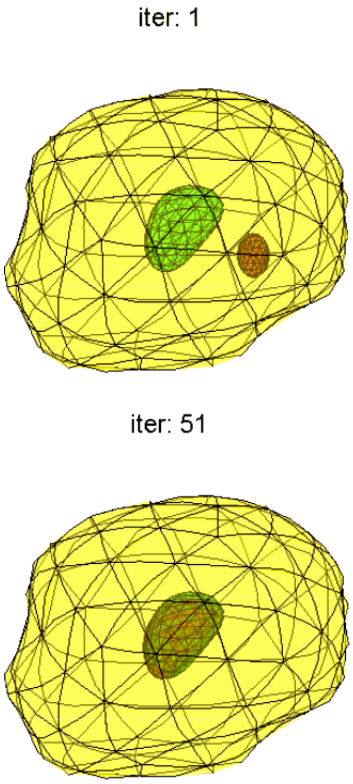

Figure 4.2: Shape-based reconstruction using the BEM: first (top) and last (bottom) iteration. The guess is in orange and the target is in green - adapted from [6]

its regularization term $\Psi(x)$ ($\Psi(x) = ||x||^2$ in the zeroth order Tikhonov case) is then optimized through a second or higher order of approximation. The main difference in the usage of the solvers based on descent methods (such as GMRES) is in the introduction of a line search step where the displacement on the direction of gradient decrease has to be found through an additional optimization process.

$$\mathscr{H} = ||y - Kx||^2 + \alpha\Psi(x) \tag{4.9}$$

Other methods which are not based on a descent algorithm exist [272].

Shape-based reconstruction and BEM Few attempts were made to reconstruct targets in a pure BEM framework and they have succeeded only on synthetic data. Arridge *et al* [6] used a shape-based non-linear method which iteratively generated shapes for a single target until convergence (see Figure 4.2). This process is computationally expensive and requires the user to know the number of perturbations present in the medium. Besides, it has only be successfully tested with the FEM on experimental data by Zacharopoulos *et al* [274].

Chapter 5

BEM-FEM Simulation Results

5.1 Forward Model - spheres

We benchmark here the accuracy of the forward model on simple analytically-computable problems where frequency domain data (modulated intensity) is computed. The analytical solution is derived from the algorithm used in a previous publication [24]. It is based on a decomposition of the solution in spherical layers on a basis of modified spherical Bessel functions and spherical harmonics.

In all our forward model results, no detectors are considered, the energy density is computed on all the nodes of the mesh and displayed as such.

5.1.1 Two concentric spheres

In this subsection, only the innermost sphere is treated with a volume-integral formulation.

We used a spherical volume mesh of 3554 volume nodes, 2146 volume elements, 1270 surface nodes and 634 surface elements. The outer sphere's surface mesh is the same as the inner sphere surface mesh as depicted on Figure 5.1.

Although the spheres were relatively small (2.5 cm radius for the outer sphere and 1.25 cm for the inner sphere), the optical properties were characteristic of a regular biological medium: $\mu'^0_s = 1mm^{-1}$, $\mu^0_a = 0.01mm^{-1}$, $n_0 = 1$; $\mu'^1_s = 0.5mm^{-1}$, $\mu^1_a = 0.02mm^{-1}$, $n_1 = 1$. The frequency was $f = 100MHz$.

The forward model (Figure 5.2) shows a perfect agreement with the BEM, and comes very close to the analytical solution. We avoided to put the point source directly on the surface but at a transport length from it because of the singularity it would create in the equation 3.17, since the source model includes a direct division by the distance between the nodes and the point source. Only the amplitude graph is scaled by a factor to fit the solutions on the outer sphere at the angle 91.4° and help in the overall understanding.

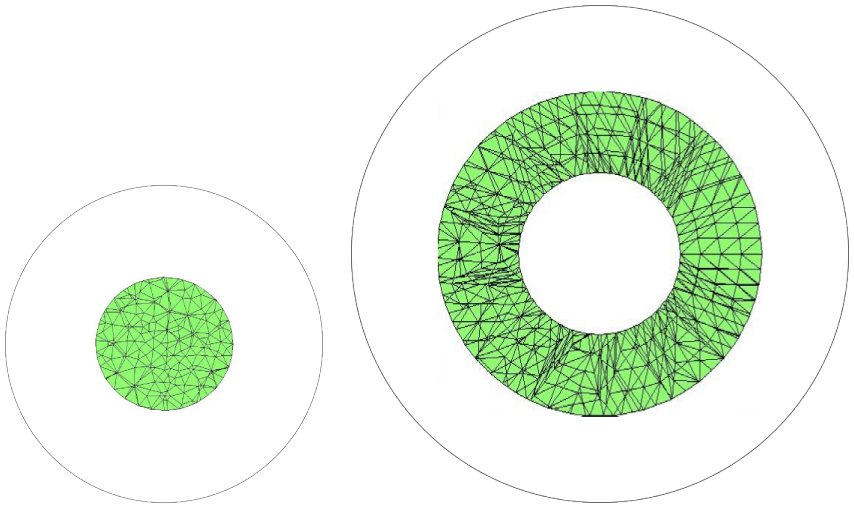

Figure 5.1: Cut through the meshes setting in the spherical cases (left: two concentric spheres; right: three concentric spheres with a volume meshed shell)

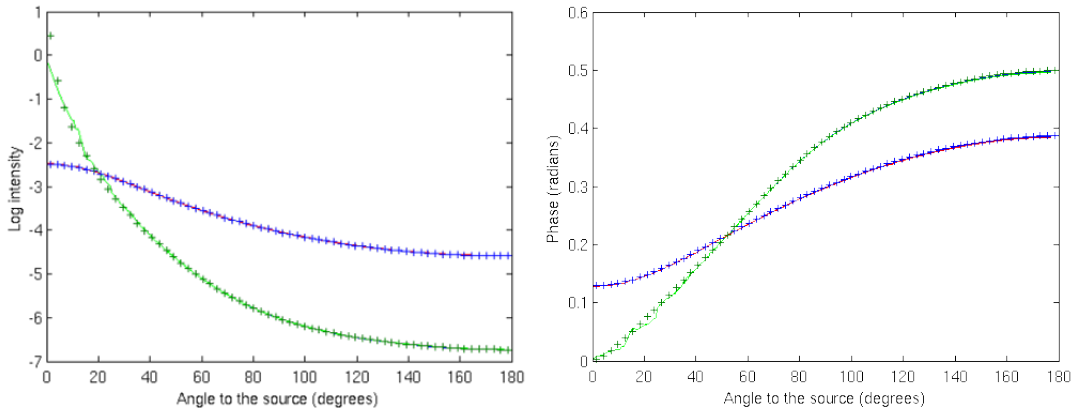

Figure 5.2: Forward model results on two concentric spheres (crosses: analytical model, continuous lines: BEM and BEM-FEM models which are superposed) - on the left, the log amplitude results can be seen against the angle to the source in degrees - on the right, it is the phase in radians against the angle to the source in degrees. Notice that the energy densities (log intensity and phase) on the two surfaces are plotted together. They can be identified by considering that the smaller the value of the log intensity at 0° and the larger the value of the phase at 0°, the deeper the surface.

5.1.2 Volume meshed shell

Here, it is a spherical shell, in between two BEM-treated volumes (see Figure 5.1) which was simulated.

As in the previous setting, the outer sphere surface mesh is the same than the outer surface of the shell but the innermost surface mesh differs from it. There were 35398 volume nodes, 23680 volume elements, 3906 surface nodes and 3808 surface elements.

Speaking about the physical properties of the system, the inner and innermost radii were the same as in the previous setting but the additional outer sphere had a radius of 3.25 cm. The optical properties were also similar with $\mu_s^{'outer} = 1mm^{-1}$, $\mu_a^{outer} = 0.01mm^{-1}$; $\mu_s^{'inner} = 0.5mm^{-1}, \mu_a^{inner} = 0.02mm^{-1}$; $\mu_s^{'innermost} = 1mm^{-1}, \mu_a^{innermost} = 0.01mm^{-1}$. The plot is visible on Figure 5.3. Once more, the amplitude results have been scaled in an identical fashion to the two-layers model to fit the analytical solution.

5.2 Forward Model - complex geometry - neonatal baby head

This case is in the continuation of a previous study by Sikora *et al* [24]. We used the same meshes (see Figure 5.4) and a NETGEN-generated volume mesh for the inner part of the brain. In the results shown in Figure 5.5, the optical properties are these of the article's case 1, which are $\mu_s^{'brain} = 1.25mm^{-1}$, $\mu_a^{brain} = 0.0178mm^{-1}$, $\mu_s^{'skull} = 1mm^{-1}$, $\mu_a^{skull} = 0.01mm^{-1}$ and $\mu_s^{'scalp} = 0.8mm^{-1}$, $\mu_a^{scalp} = 0.0149mm^{-1}$. The source has been placed behind the head of the subject. Notice that the intensity of the source and its exact placement are different from the ones used in [24].

A further analysis could have led us to compare our results with a Monte-Carlo simulation similar to [59] but we relied on the accuracy of the BEM code instead [24] throughout this thesis, since it was itself tested against a Monte-Carlo simulation.

5.3 Reconstruction results

The computations presented here are all perturbation reconstructions where the optical properties of the regions are considered as known *a priori*. It is only localised absorption coefficient changes which are reconstructed. The scattering coefficients are set throughout.

5.3.1 Concentric spheres

We placed an absorption blob of size 1.4mm (x) by 1.4 mm (y) by 12.4mm (z) in the center in z of the innermost sphere of a three-layered model and slightly out-centered in x and y with a contrast of 3.6:1, i. e. $\mu_s^{'blob} = 0.61mm^{-1}$, $\mu_a^{blob} = 0.05mm^{-1}$. We used the mesh shown in Figure 5.6, which allows a precise reconstruction and is typical of a problem difficult to solve with

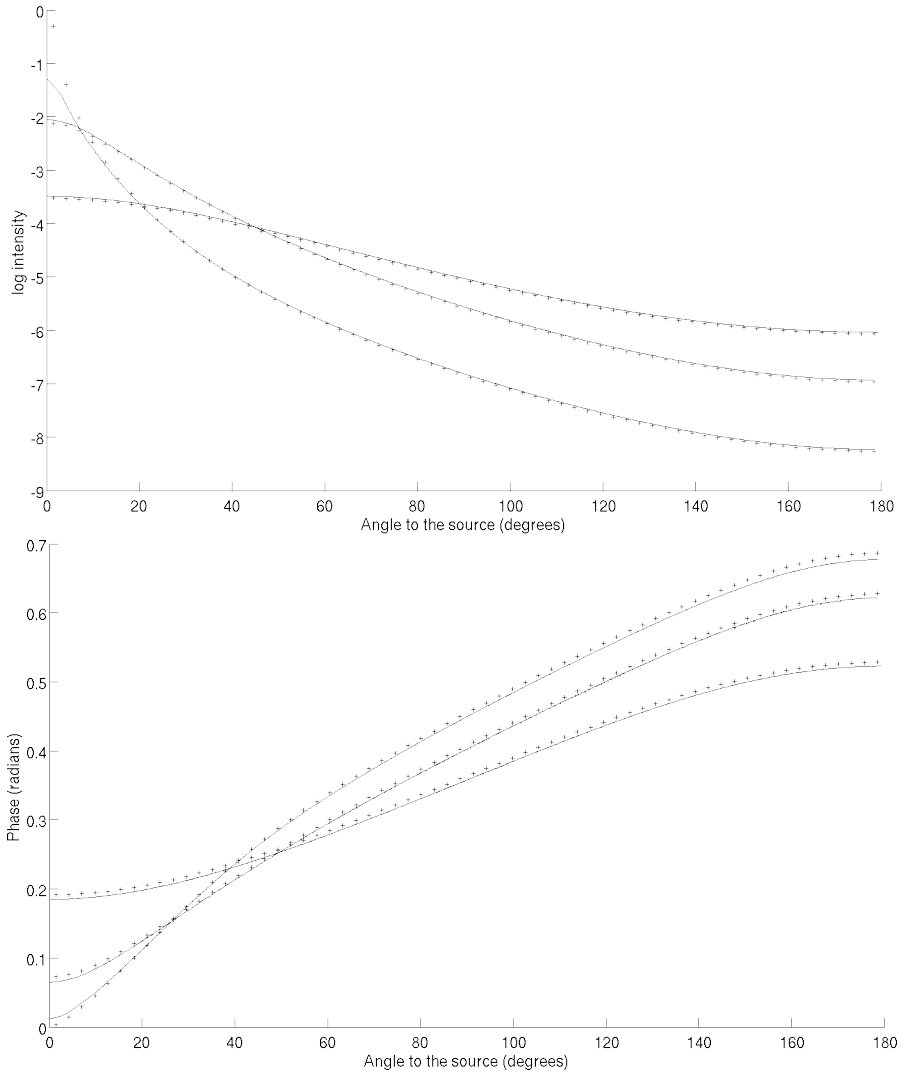

Figure 5.3: Forward model results on three concentric spheres (stars: analytical model, circles: BEM-FEM model, continuous line: BEM model) - on top, the log amplitude results can be seen against the angle to the source in degrees - on the bottom, it is the phase in radians against the angle to the source in degrees. Notice that the energy densities (log intensity and phase) on the three surfaces are plotted together. They can be identified by considering that the smaller the value of the log intensity at 0° and the larger the value of the phase at 0°, the deeper the surface.

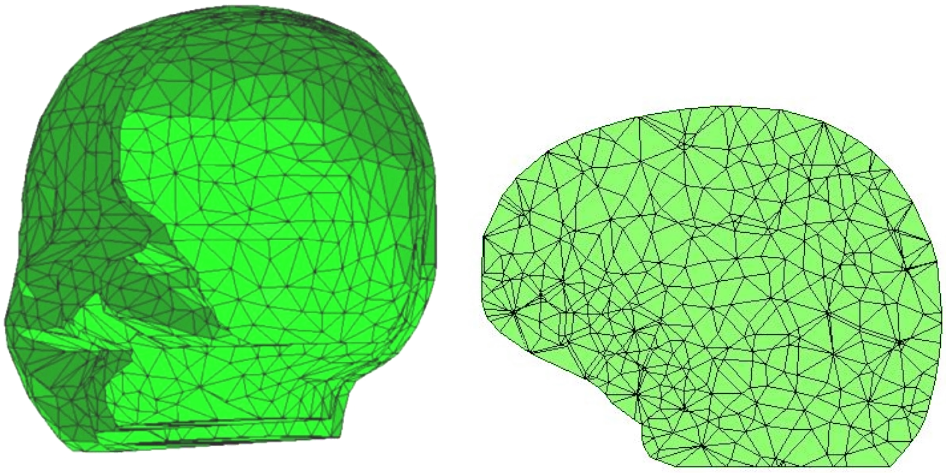

Figure 5.4: Meshes used for the neonatal baby head problem (left: original meshes, right: cut through the newly generated brain's volume mesh of 8174 volume nodes, 5285 volume elements - its surface is the same as the original brain surface mesh)

the FEM, i.e. with very thin layers between spheres of radii 44, 47 and 50 mm. It was successfully recovered as shown in Figure 5.7. The 32 sources and 32 detectors were arranged in a ring around the equator of the spheres in a 1 source - 1 detector equally spaced pattern. The optical parameters were close to a neonatal human head $\mu_s^{'brain} = 0.61mm^{-1}$, $\mu_a^{brain} = 0.014mm^{-1}$, $\mu_s^{'skull} = 0.625mm^{-1}$, $\mu_a^{skull} = 0.024mm^{-1}$ and $\mu_s^{'scalp} = 1.4mm^{-1}$, $\mu_a^{scalp} = 0.016mm^{-1}$. A 1% Gaussian noise was added to the synthetic data generated with the model.

Some results present negative absorption: this is due to the noise present in the simulated data. It generates artefacts which can lead to such problems, since the values the absorption coefficient can take are not constrained. One should also remember that this is a difference measurement, and that what is displayed is the difference between the optical absorption coefficient changes and the background optical properties.

5.3.2 Neonatal head

A volume mesh for the inner part of the brain was generated from Γ_2 using NETGEN [267]. The setup consists of 12 sources and 30 detectors positioned in an helmet-shaped distribution as described in Figure 5.8. The minimum source-detector distance is 14mm and the maximum is 114 mm. In order to provide a fair comparison to the *in vivo* measurements in section 6.2, we used only 258 out of the 360 possible measurements. The actual experiment is detailed in this same section.

For the restricted FEM (see 4.2) reconstruction, the mesh is quadratic tetrahedral, with 100789 nodes and 69357 elements but the reconstruction was restricted to the 43280 nodes brain region which was obtained by cutting through the bulk mesh volume with the warped

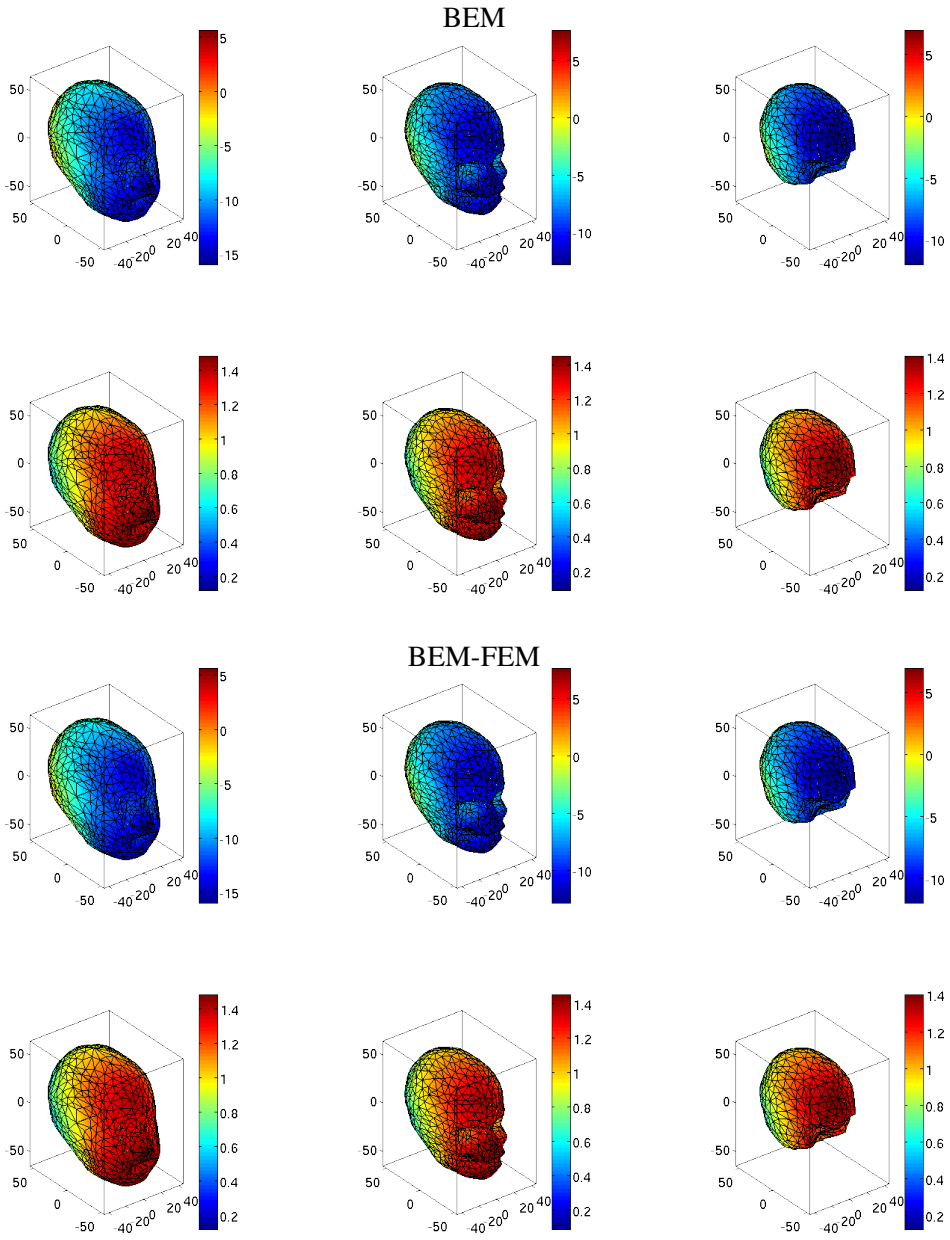

Figure 5.5: BEM (top) and BEM-FEM (bottom) forward model results on the neonatal head. In these two sets of pictures, the three top graphs show the log intensity while the three bottom graphs show the phase

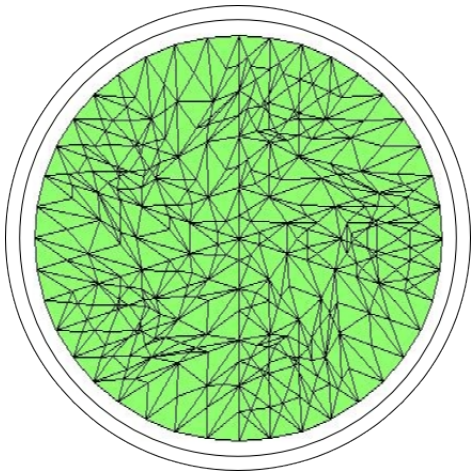

Figure 5.6: Cut through the meshes setting in the three layers case - the innermost mesh has 14993 volume nodes, 10240 volume elements, 2562 surface nodes and 1280 surface elements and the inner and outer meshes are scaled versions of the coarser mesh presented before

BEM surfaces. A 31336 nodes skull layer and a 26173 scalp layer were also created by the same process. The BEM-FEM mesh is made of a much coarser mesh with 2806 surface nodes and 1402 surface elements for the scalp layer, 3294 surface nodes and 1646 surface elements for the skull layer, 2098 surface nodes and 1048 surface elements for the brain region of the BEM mesh and 6719 volume nodes and 4192 volume elements for the FEM brain mesh. The entire FEM mesh is mapped to a regular grid of voxels while, in the case of the BEM-FEM reconstruction, only the brain region is actually mapped to voxels. In the displaying process, however, both solutions and all meshes are mapped to similar voxel grids for comparison.

The reconstructions shown in Figure 5.9 are obtained with optical parameters close to a neonatal human head $\mu_s^{'brain} = 0.61mm^{-1}$, $\mu_a^{brain} = 0.014mm^{-1}$, $\mu_s^{'skull} = 0.625mm^{-1}$, $\mu_a^{skull} = 0.024mm^{-1}$ and $\mu_s^{'scalp} = 1.4mm^{-1}$, $\mu_a^{scalp} = 0.016mm^{-1}$. When comparing the two methods on simulated data, we found that the BEM-FEM is as accurate as the FEM with the maximum of the reconstructed blob distributions being both about 3mm away from the target.

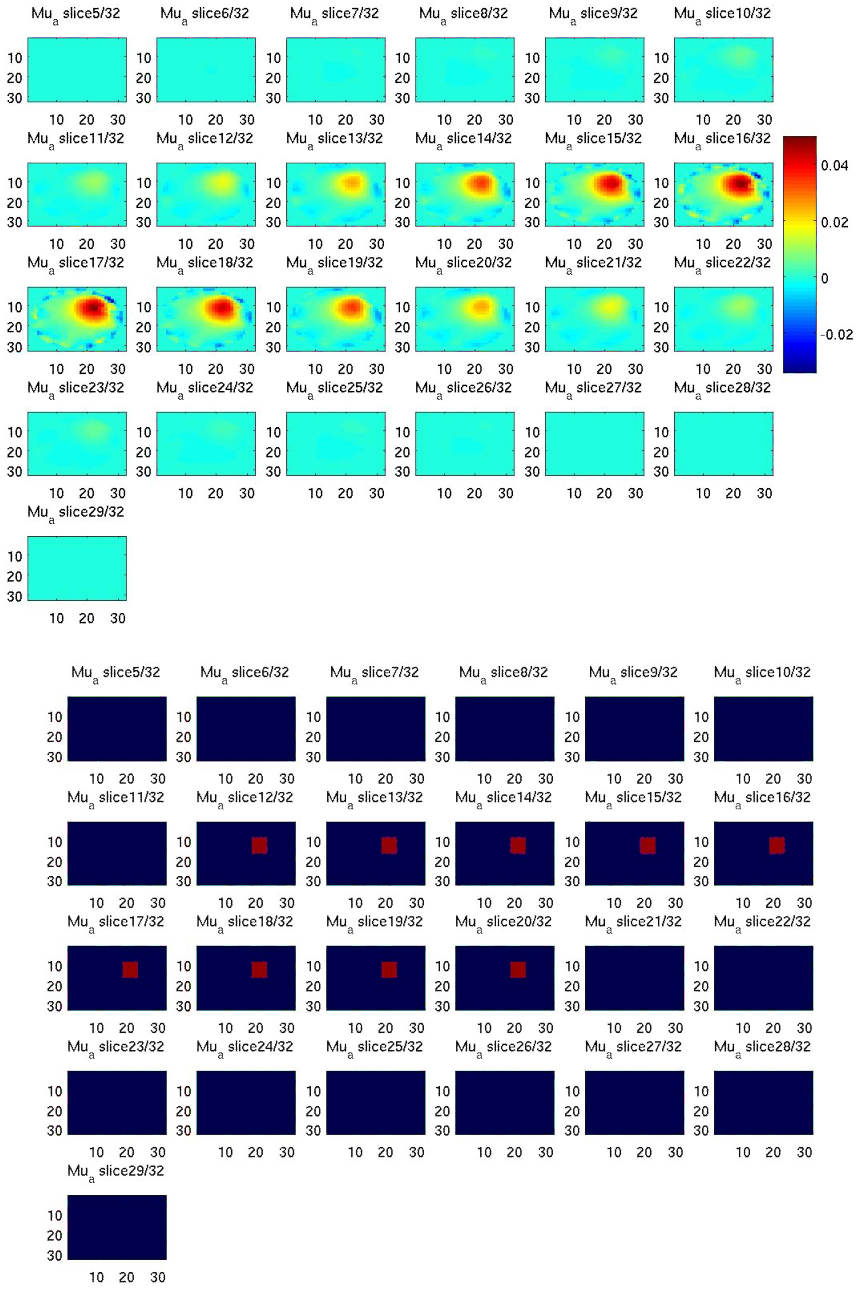

Figure 5.7: Reconstruction on the three concentric spheres model (slices 5-29 of 32 in z in the reconstruction volume which fits the inner volume integral-treated sphere only) - on top: reconstructed absorption distribution on the three layers model with a 0^{th} order Tikhonov regularisation term $\alpha = 4 \times 10^{-3} \times Trace(Jacobian^2)$; on the bottom: ground truth with the background in blue and the target in red ($0.05 mm^{-1}$ absorption)

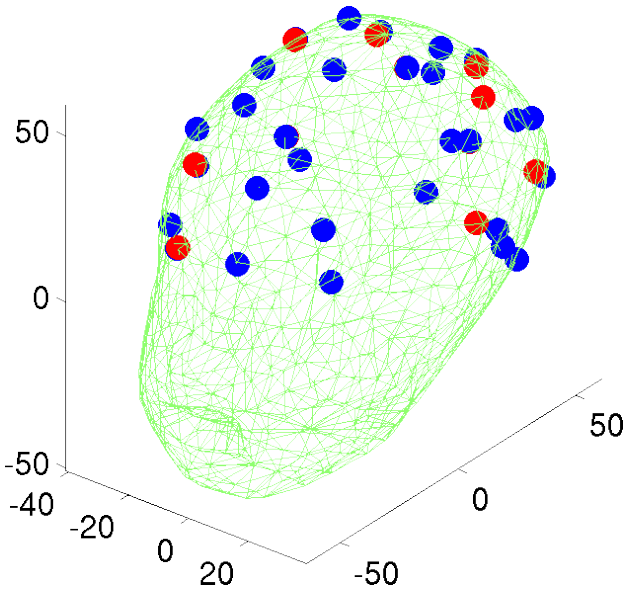

Figure 5.8: Partial 3D view of the optodes on the scalp mesh; the sources are in red and the detectors in blue

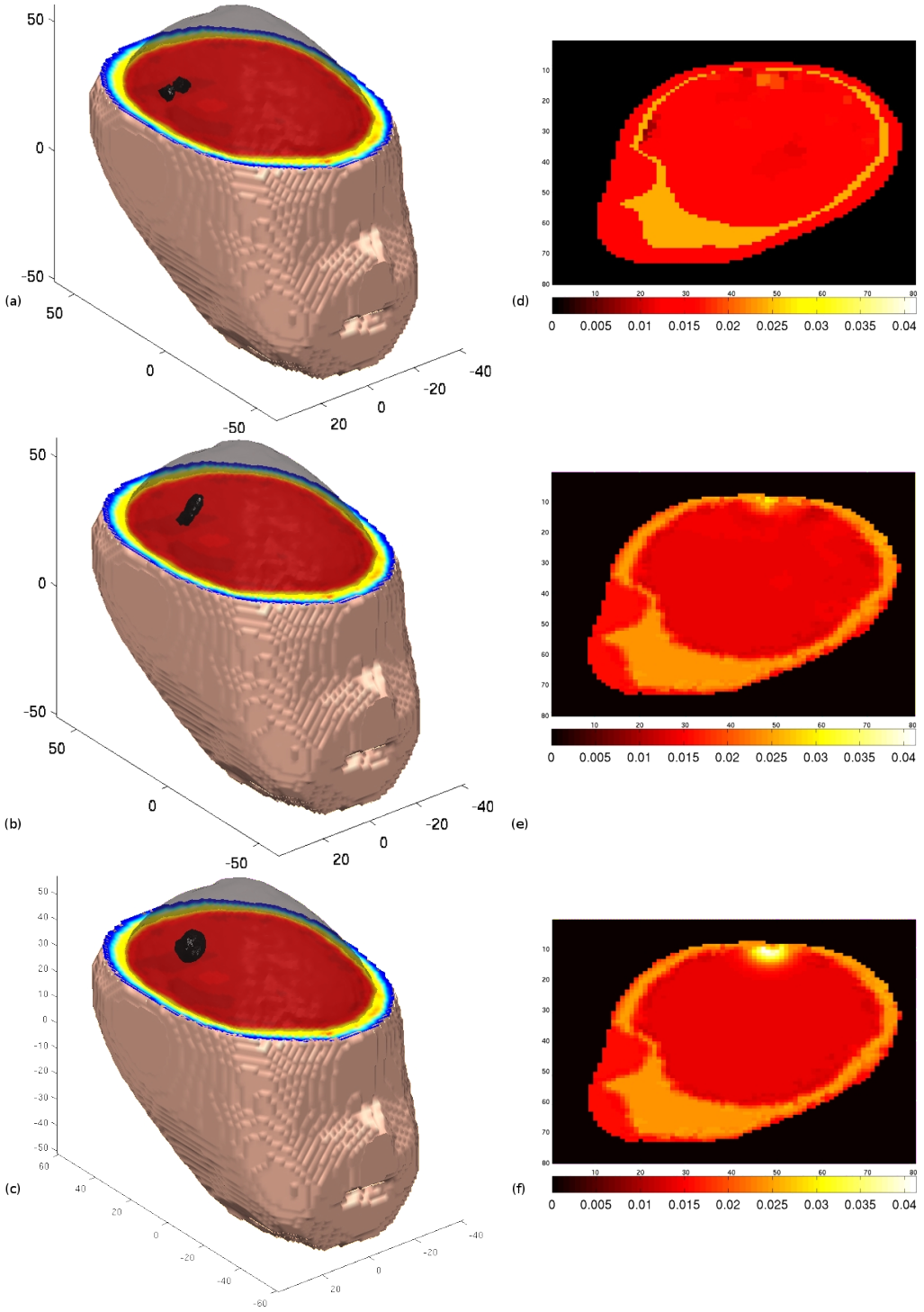

Figure 5.9: Simulated reconstructions on the baby head model (a, b and c: 3D views of BEM-FEM, FEM and ground truth reconstruction isosurfaces in head models; d, e and f: BEM-FEM, FEM and ground truth slices in the reconstructed absorption volume

Chapter 6

BEM-FEM Experimental Results

6.1 Baby head phantom

6.1.1 Experimental setup

In this section, we decided to test the methods on a baby head phantom [7]. It consists of a head model in which a diffusive liquid is put. The container has the shape and size of a baby head. A cavity of a size comparable to a baby's brain has been made inside to put the liquid. Figure 6.1 describes how the system looks.

I carried out the experiment and analyzed the data in collaboration with Dr. Louise Enfield. We fitted our 32 sources and detectors helmet [40, 275, 276, 98] on this resin doll and filled the "brain" area with a liquid with non-matching optical properties. We then recorded time-domain data (TPSFs [126]) through 29 sources and detectors. This data was Fourier-transformed to 10 MHz frequency-domain data with the embedded software of our MONSTIR [269] scanner (see subsection 4.1.1). Of the potential 841 measurements, 473 were kept for their consistency.

The phantom is composed of a two-part epoxy resin [277] (MY753 with XD716 hardener, Ciba-Geigy Ltd) and is made from an anatomically realistic doll. Its average radius is close to 3.8cm, which corresponds to a pre-term baby. In order to reproduce the optical properties of a neonatal head, titanium dioxide has been added to reach a scattering coefficient of $\mu_s' = 1mm^{-1}$ and a near-infrared absorbing dye called Pro Jet 900 NP (Zeneca Ltd, Manchester, United Kingdom) for an absorbing coefficient of $\mu_a = 0.01mm^{-1}$.

The non-matching liquid is made out of the same resin, but without hardener and with a different percentage of titanium dioxide. We prepared 230g of resin, of which 227.9g was MY753 with 1.86g of Pro Jet dye and 0.24g of scatterer. This solution, according to our knowledge of the individual components has the optical properties $\mu_s' = 0.8mm^{-1}$, $\mu_a = 0.01mm^{-1}$.

We introduced a $\mu_a = 0.03mm^{-1}$ (and matching scattering coefficient) perturbation in the form of a small cylinder (height and diameter: 7mm) in the liquid resin. It is attached to a thin

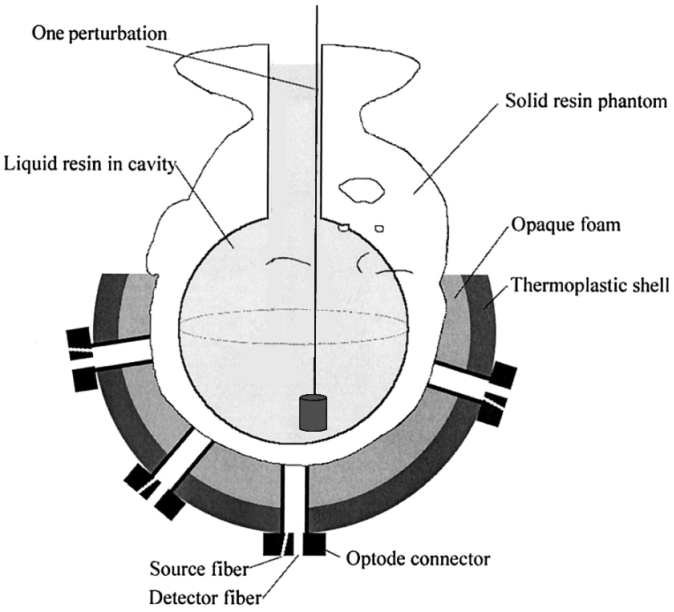

Figure 6.1: Schematic cut through the experimental device adapted from [7]

steel rod, which measures about 20cm with a diameter of about 1mm in order to stay in place in the resin. The rod is not visible and is ignored during the reconstruction because its dimension is far below the resolution. Besides, it is opaque to photons at the wavelength used.

6.1.2 Mathematical setup

We have the exact geometrical properties of the phantom, thanks to an earlier XCT scan [7]. From the surfaces of these scans, we created new meshes for BEM-FEM and FEM. The pure FEM mesh contains 139397 volume nodes and 97608 volume elements. On the other hand, the surface meshes of the BEM-FEM, for the scalp, contains 4486 surface nodes and 2242 surface elements and for the inner layer that we will call the “brain”, 4814 surface nodes and 2406 surface elements. The volume-integral treated region of the BEM-FEM (here, the brain) contains 10910 volume nodes and 6260 volume elements. A cut through the models can be seen on Figure 6.2.

6.1.3 Results

In Figure 6.3, very clear results can be seen. A blob is recovered close to the bottom of the “brain” region. This is in agreement with the Figure 6.1. Despite the lack of precision of the shape recovered, which was expected, the BEM-FEM results is somewhat convincing. However, when looking at the FEM one, it appears that the resolution is much poorer. The reason for this is unknown, especially when we consider the much better *in vivo* results in subsection 6.2.2.

The computation time was longer for the FEM (40 mins) than for the BEM-FEM (25 mins)

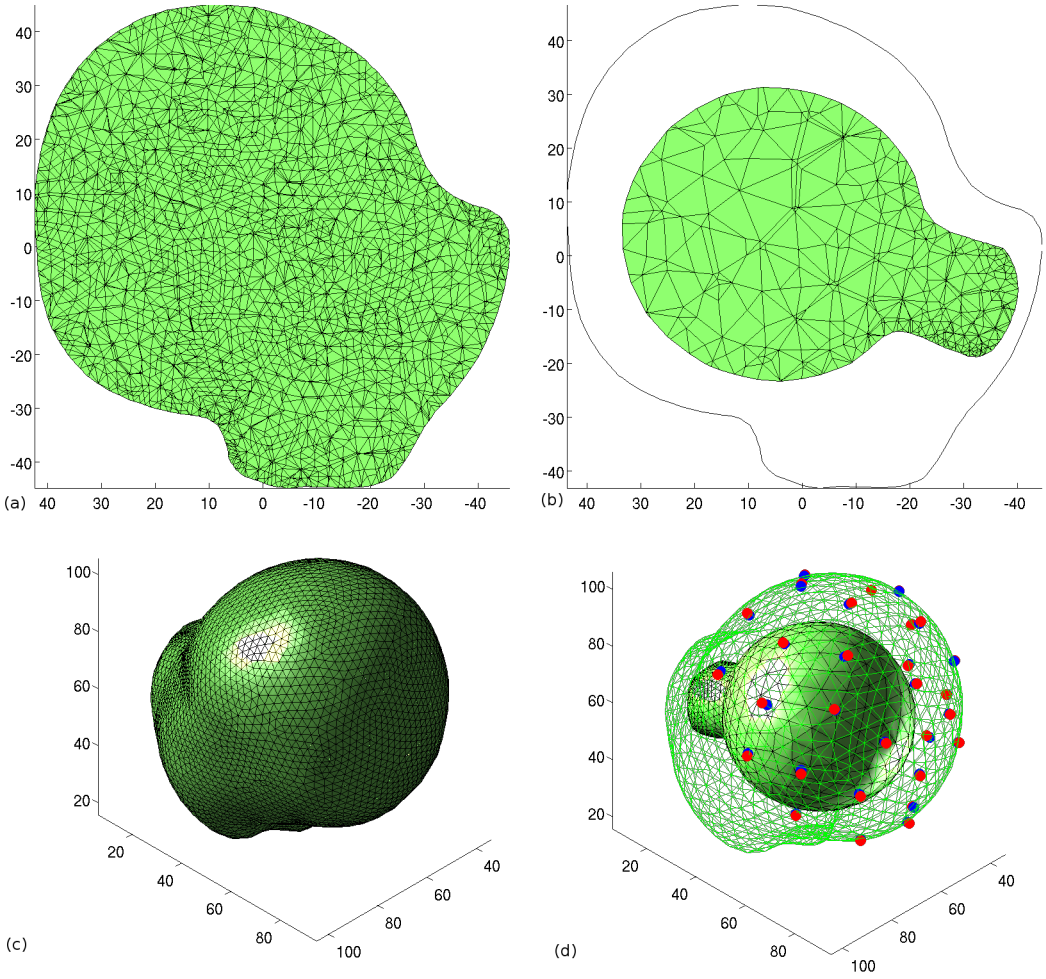

Figure 6.2: Meshes used in the simulation, with the phantom facing down - (a): cut through the FEM mesh; (b): cut through the BEM-FEM meshes; (c): surface of the FEM mesh; (d): surface of the BEM mesh with the sources in red and the detectors in blue

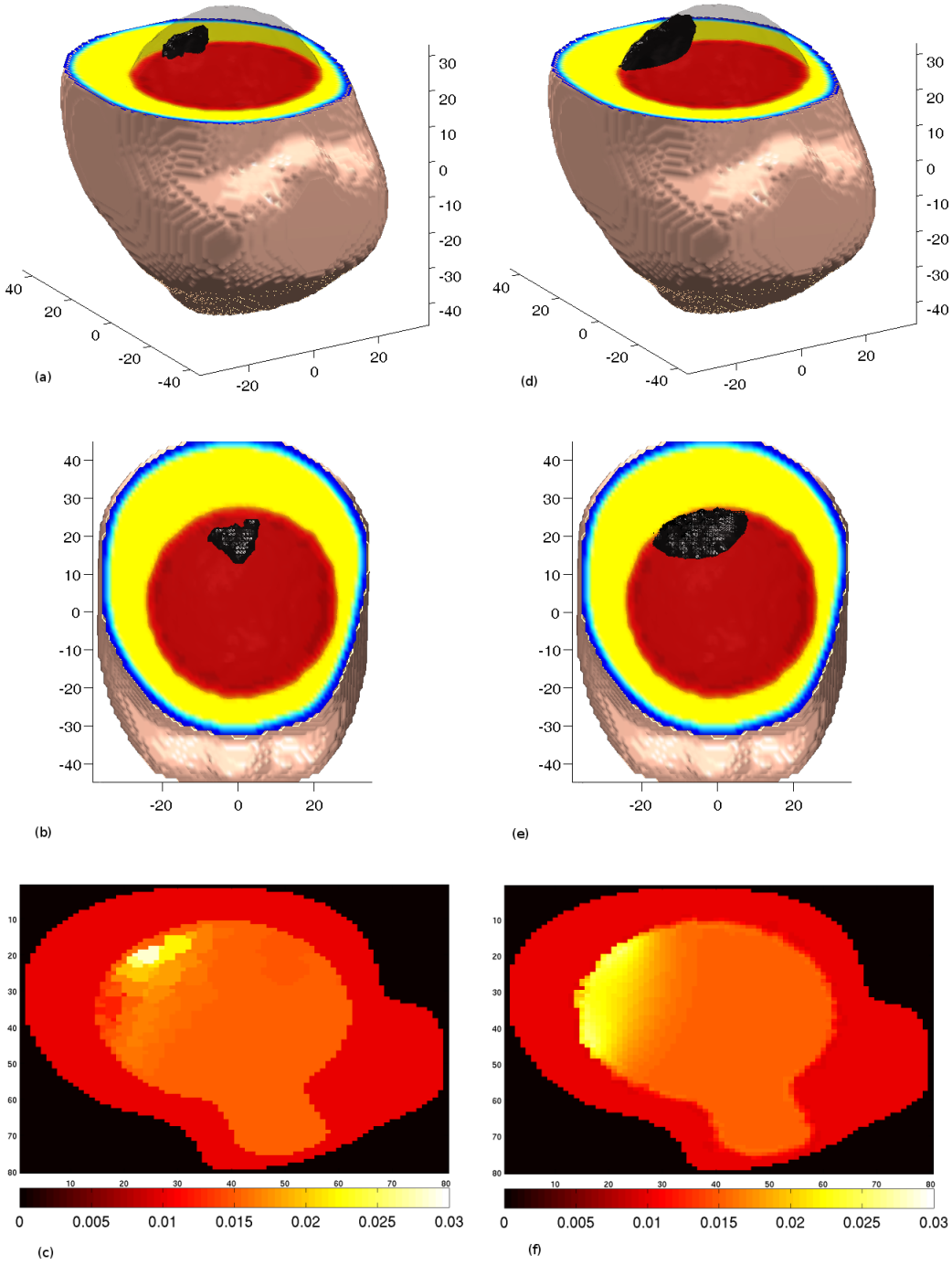

Figure 6.3: Experimental reconstruction on the phantom head model (a): 3D view of a BEM-FEM reconstruction isosurface (only the scalp and brain are represented for convenience), (b): Top view of that same BEM-FEM reconstruction isosurface, (c): BEM-FEM slice in the reconstructed absorption, (d): 3D view of a restricted FEM reconstruction isosurface, (e): Top view of that same restricted FEM reconstruction isosurface, (f): restricted FEM slice in the reconstructed absorption.

for the Jacobian building. All other steps were very comparable. This is mainly due to the high resolution of the FEM mesh chosen.

This study is considered as a step towards the much deeper understanding brought by the *in vivo* experiment and further analysis of the difference between the methods is found there.

6.2 In vivo results

6.2.1 Setup and experiment

After these successful testing of the BEM-FEM against the FEM in the aforementioned phantom study, we went on to test the method on data from an *in vivo* motor response study on pre-term babies as reported in [98, 276].

As the neonate is sleeping, his arm is moved: this stimulus activates area of the brain corresponding to the action, here the motor cortex. Such a technique allows to use the linear reconstruction theory, since we can have the data before (reference rest state) and during the movement. In the present case, it is the right arm which is displaced.

The experimental setup consisted of 12 sources and 30 detectors, as presented earlier in the Figure 5.8. 258 measurements were kept for the analysis out of the 360 possible ones.

All the meshes used here and the optical parameters are identical to the simulation in subsection 5.3.2. The only difference is in the actual position of the activation, which is here in the left hemisphere.

In the previous publication [98], the motor cortex's activation was reconstructed with a resolution of 10mm. Here, we took as a reference a restricted FEM reconstruction in which the FEM is tuned to find a change in the absorption only inside the brain region. In such an experiment, due to the setup and the nature of the subject, one only has the position of the sources and detectors relative to an absolute origin. The actual attitude of the baby has to be inferred from this data. The mesh is then warped onto the measurement cap using a method in three steps:

1. Rigid body translation, rotation and stretching of the surface in 3D so that the surface comes relatively close to the optodes, i.e. that the surface passes through the space spanned by the optodes

2. Identification of the closest nodes on the surface mesh to each optode

3. Applying of a nonlinear thin-plate spline deformation which makes the surface mesh passing through all the optodes whilst minimizing a bending energy expressed as the square root of the second derivatives

The details of this method can be found in a paper by Gibson *et al* [263].

6.2.2 Detailed results and comparison with FEM

As it can be seen in Figure 6.4, the comparison between the restricted FEM and the new BEM-FEM reconstruction shows close results. The theoretical resolution of each solution is close to 10mm if a Gaussian distribution is assumed. We also observe a 4mm distance between the maxima of the two reconstructed absorption maps, a value which is well below the resolution.

6.3 Discussion on performance

Modeling light propagation in complex structures such as the brain must be done numerically, most commonly using the FEM which requires a finite element mesh. Producing a high-quality finite element mesh of the head is extremely difficult and is one of the issues restricting the clinical useability of optical tomography. The problem of segmenting a magnetic resonance image of the head is now largely solved, particularly in adults but it is still not straightforward in babies. Even once the segmented image has been obtained, creating a finite element mesh which can represent the light fields with sufficient accuracy is demanding.

As highlighted very early on by Beer [278], and confirmed later in many studies [44, 279] one of the main advantages in principle of a mixed BEM-FEM formulation is the focus. In the particular case of DOT, we usually know where (in which organ for example) the contrast lies. By introducing prior information about the problem in the geometry of the solution itself, we increase the accuracy of the results [280, 281, 282]. By restricting the reconstruction to a particular organ, we also implicitly assume that there are no perturbations occuring in the other regions. This could be a criticism of our work since it has been proven that the extracerebral layers, especially in the case of motor activation, exhibit a change in absorption, due to the peripheral blood movements related to the muscular effort [185, 184, 186, 187]. We considered these perturbations as negligible, since the babies are asleep and the movement is actually applied to them, not originating from them (see subsection 6.2.1).

The BEM-FEM shows that it is possible to keep the FEM accuracy while easing the meshing task and reducing the problem's size. Even in the extreme case of a relatively thin FEM layer (here, the skull), the method does not fail. The result of the two techniques in the in vivo case are comparable while being obtained very differently. We especially notice that the position of the motor cortex is recovered with similar errors despite the fundamental difference in the meshes' constitution.

A more careful look at the method emphasizes the fact that a good match has to be found between the small number of nodes and high structural information content needed in a BEM

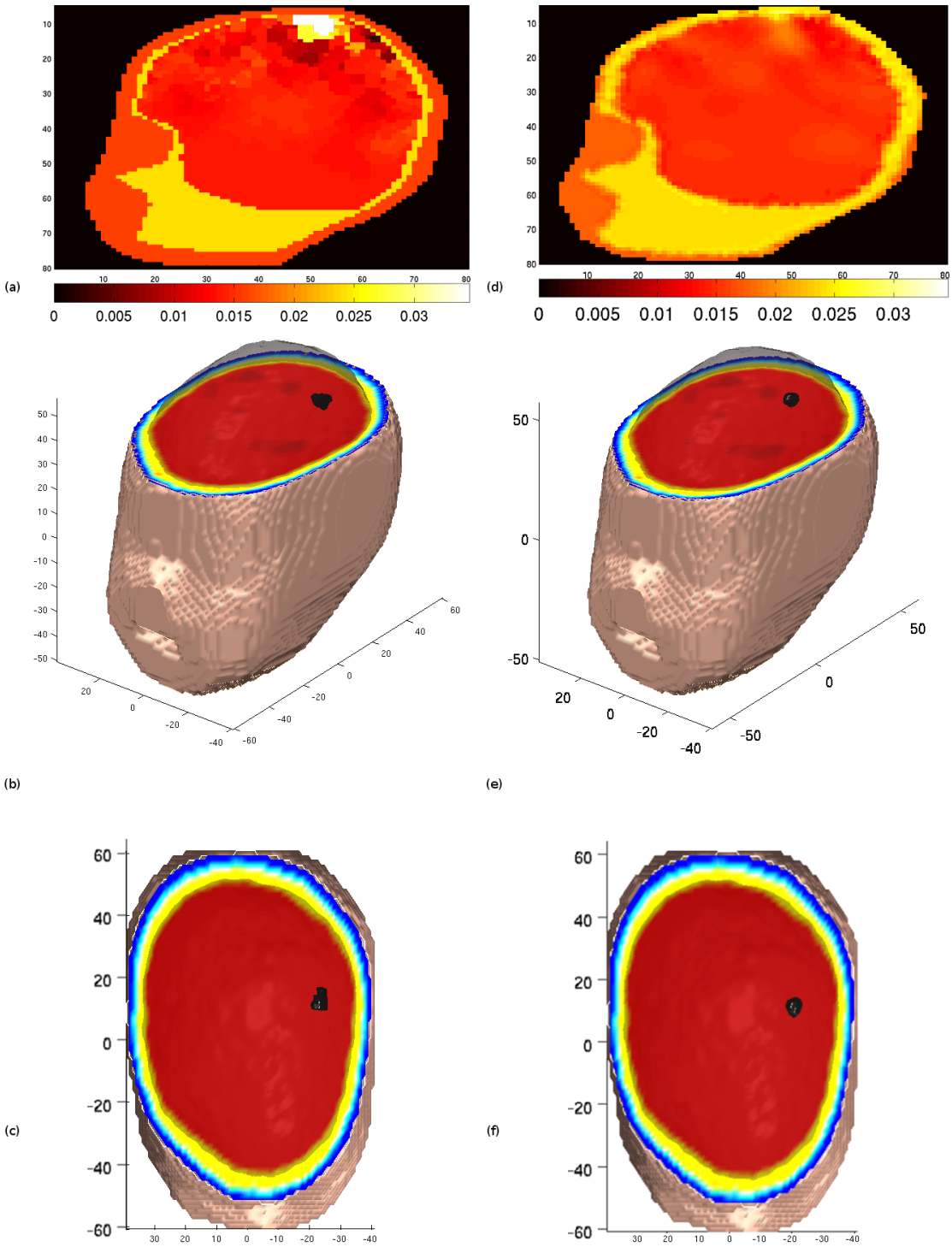

Figure 6.4: Experimental *in vivo* reconstruction on the baby head model (a): BEM-FEM slice in the reconstructed absorption, (b): 3D view of a BEM-FEM reconstruction isosurface (only the scalp and brain are represented for convenience), (c): Top view of that same BEM-FEM reconstruction isosurface, (d): restricted FEM slice in the reconstructed absorption, (e): 3D view of a restricted FEM reconstruction isosurface, (f): Top view of that same restricted FEM reconstruction isosurface.

mesh and the high resolution required in a FEM mesh. We tried to make a trade-off between these parameters and the computational expense. The lower density of these BEM-FEM meshes shows that one can avoid building the high resolution FEM mesh needed to reach an excellent convergence in all the layers. In our particular case, the skull and scalp layers were very thin (in the order of magnitude of 1mm in thickness in the upper part of the head). These kind of volumes are difficult to mesh properly using the FEM, and one has to increase the overall density of the mesh, as we did in the experimental study with about 13000 nodes (some surface nodes and some volume nodes) in BEM-FEM compared to about 100000 volume nodes in FEM.

One should also notice that the optical parameters in the layers around the volume-integral treated region of interest have to vary smoothly between the layers in order to avoid a concentration of the photon-measurement density function outside from it [283]. This is more susceptible to happen in a sharp piecewise-constant system, particularly when a low scattering region exists [97, 5].

When attention is given to the remarks above, the BEM-FEM stands out as a new easier choice when dealing with layered turbid media. It allows a simplification of the problem, especially through the avoidance of useless mesh generation, which actually enforces the anatomy in the numerical method.

The BEM-FEM frees any Near Infra-Red Spectroscopy (NIRS)-based problem from the partial volume effect (see subsection 2.2.1.4) by allowing a direct conversion of the absorption coefficient to Hemoglobin concentration. This opens the road to a more reliable quantification of the functional data obtained in DOI.

In the current implementation, the reconstruction times are the same between the FEM and BEM-FEM, due to the restriction of the reconstruction volume to the volume-integral treated region, and are below 2mins. However, one should keep in mind that, despite the reduction of the number of unknowns when passing from the FEM to the BEM-FEM, the BEM-FEM is not faster than the FEM. This is partly due to the BEM part of the solution which produces a dense array while the FEM matrix is sparse. Nevertheless, let us remember that we are comparing a newly written BEM-FEM code and a FEM code which has been optimized for this application for more than ten years. In numerical terms, in the neonatal baby head case, the BEM-FEM code currently takes 3 minutes to construct the forward model matrix (14 s in FEM) and 27 minutes (11 min in FEM) to build the Jacobian by computing the forward and adjoint fields.

Despite all this, when considering the time gained in the BEM-FEM mesh simplicity, the advantages are still apparent.

Chapter 7

BEM Diffuse Optical Cortical Mapping

7.1 Theory of the Diffuse Optical Cortical Mapping with the BEM

Doing DOCM with our existing tools (see chapter 2.1) is straightforward. As we have seen in subsection 2.2.1.3, tomographical tools can be used for topography. However, in our case, we want more than a 2D map. Rather, our goal is here to end up with a 3D map of the cortex on its surface.

Using a BEM, we develop a model for the mapping of photon densities between surfaces of the multilayer representation, thus reconstructing what we introduce as an *Equivalent Cortical Absorption* $\left(\mu_a^{\mathrm{ECA}}\right)$. The BEM theory developed earlier in section 3.2 remains valid. The only change is in the reconstruction method. We had before an intermediary space, the reconstruction grid, in which the absorption coefficient was mapped. We now have to do the reconstruction on the brain surface and thus eliminate the FEM part of the problem. The Jacobian of the new problem is computed with the forward and adjoint fields on the innermost BEM surface. The reconstruction space becomes the nodes of this surface. Our method suggests that it is possible to overcome the fundamental limitations of functional optical topography and obtain reliable maps of the cortex with a simple and fast algorithm.

Formulation

Like in section 4.2, we need to compute probe fields (from the sources and detectors). We consider S inward directed photon currents at source locations $\{\mathbf{r}_s, s = 1 \ldots S\}$ so that

$$Q_s = \begin{pmatrix} Q_s^{(0)} \\ 0 \\ 0 \\ \vdots \\ 0 \end{pmatrix}. \tag{7.1}$$

Solution of the BEM system eq.(3.25) for each input source generates the cortical photon probe densities $\{\Phi_s^{cortex}, s = 1 \ldots S\}$. Now consider the secondary sources given by the product of the probe fields and the activation in the brain, which, using Green's identity, become

$$q_s = \begin{pmatrix} 0 \\ 0 \\ 0 \\ \vdots \\ q_s^{(n_\Omega)} \end{pmatrix}, \qquad \text{where} \quad q_s^{(n_\Omega)}(\mathbf{r}) = \int_{\Omega_{n_\Omega}} G_{n_\Omega}(\mathbf{r}, \mathbf{r}') \mu_a^{actvn}(\mathbf{r}') \Phi_s^{(n_\Omega)}(\mathbf{r}') d\mathbf{r}' \tag{7.2}$$

where $\Phi_s^{(i)}(\mathbf{r}')$ is the solution density in the i^{th} layer for the source s. When dealing with nested BEM regions representing a head, Ω_{n_Ω} is the brain or the innermost region. Solution of eq.(3.25) with the secondary sources $q_s^{(\mathrm{n}_\Omega)}$ results in the secondary density Φ_s^{actvn}. The equivalent cortical absorption is therefore modeled by

$$\Phi_s^{\mathrm{actvn}} = \mu_a^{\mathrm{ECA}} \Phi_s^{\mathrm{cortex}} . \tag{7.3}$$

The ECA is a new concept which should be understood as a work in progress. As stated in eq.(7.3), it is the ratio of two surface energy densities coming from BEM results. This means that it does not have any unit, but rather corresponds to an attenuation due to the absorbers contained in the cortical region.

The quantity Φ_s^{cortex} corresponds to the energy density on the surface of the cortex if there were no absorbers inside. The quantity Φ_s^{actvn} corresponds to the energy density considering that the activated brain is the source ($q_s^{(\mathrm{n}_\Omega)}$) of the light. This means that Φ_s^{actvn} is attenuated by the integrated absorption (μ_a^{actvn}) coming from the activation which manifests itself by the cortical map obtained with μ_a^{ECA}. Basically, the ECA cannot be interpreted as a simple absorption coefficient and further study is needed to be able to relate it to a Hemoglobin/Total Hemoglobin ratio (HbO_2/Hb_{total}).

The inverse problem is solved in a similar fashion than described in chapter 4.

7.2 Simulation results - neonatal head model

The same meshes, optical properties and optode placement were used for the simulation as in the BEM-FEM in-vivo case in subsection 5.3.2 and the DOCM one in section 7.4, the detail of which are in the former. 258 measurements were kept for the analysis out of the 360 possible ones as in the section 6.2. A spherical inclusion with $\mu_{\mathrm{a}}^{\mathrm{inclusion}} = 0.034 mm^{-1}$ and of diameter

10mm was put inside the brain layer and moved along a surface normal deeper inside the mesh. The BEM-FEM model was used to generate the data and 1% of white noise was added to it. The regularisation parameter was set to $\alpha = 1.72 \times \mathrm{Tr}[\mathsf{W}^{\mathrm{T}}\mathsf{W}]$.

The figures 7.1 and 7.2 show a trend of contrast increasing and diminishing, as the blob varies in overlap with the Photon Measurement Density Function [284] of the optodes. As it moves deeper inside the brain, the contrast decreases and the noise is reconstructed instead.

The pictures in Figure 7.1 and 7.4 have been generated by a projection of the solution on a higher resolution brain mesh of 13498 surface nodes mesh for improved visualisation. Both the coarse and fine resolution meshes were obtained from a model using data from MRI scans of a neonate, courtesy of Tizzard *et al* [285].

The projection between meshes was implemented using the following steps:

1. Rigid body registration of the low and high resolution brain meshes;
2. Reparametrisation of both brain meshes to spherical coordinates;
3. Linear interpolation on the sphere of the values on the coarse mesh's nodes onto the fine mesh's nodes using an equal-area planar map projection;
4. Reprojection of the fine mesh's sphere to the fine brain mesh by converting back to Cartesian coordinates.

Notice that this is not an inverse crime, since a different model (BEM-FEM) is used to generate the data and a fair amount of noise is added. This explains the large amount of artefacts observed.

7.3 Phantom results

We took the same phantom measurements and setup as the previously reported BEM-FEM successful experiment (see section 6.1). The only differences are that the absorption change is now reconstructed on the brain BEM surface and the regularization parameter was set to $\alpha = 5.15 \times 10^3 \times \mathrm{Tr}[\mathsf{W}^{\mathrm{T}}\mathsf{W}]$. The results are shown on Figure 7.3.

7.4 In vivo experimental results

Again, the BEM-FEM experiment of section 6.2 has been re-analyzed with the BEM DOCM. All parameters were kept identical, except the Tikhonov regularization parameter.

In a previous publication [98], the motor cortex's activation was reconstructed with a resolution of 10mm. As it can be seen in Figure 7.4, the activation has been localized on the brain

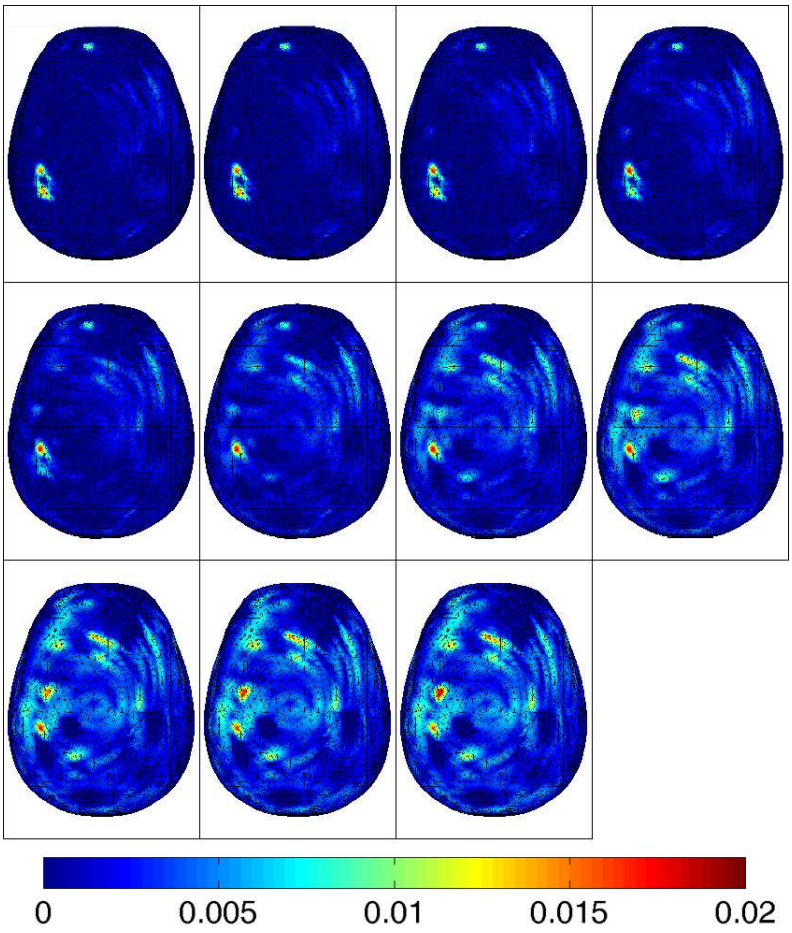

Figure 7.1: Left to right and top to bottom, reconstructions of a Gaussian absorption target simulated with the FEM (1% noise). The target is moved by 2mm from the surface of the brain (top left) to 20mm below the surface. Notice that the ECA is dimensionless.

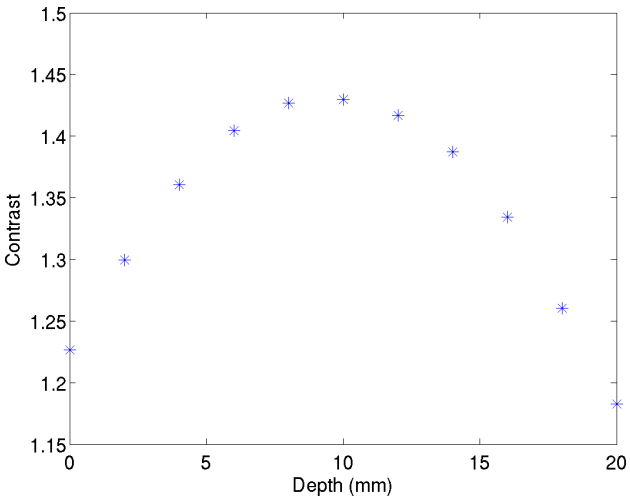

Figure 7.2: Evolution of the contrast, i.e. the difference absorption of the target divided by the background absorption. The nominal value is 1.43.

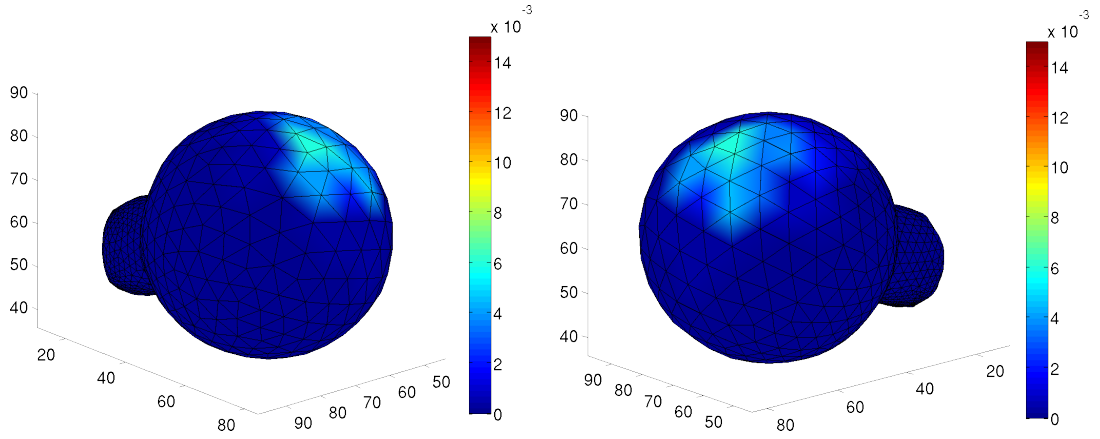

Figure 7.3: Side views of a cortical map of the "activated" phantom "brain" - the effect of the blob inserted in the liquid resin is clearly visible

surface. The regularisation parameter was set to $\alpha = 0.97 \times \mathrm{Tr}[\mathrm{W}^{\mathrm{T}}\mathrm{W}]$. The lateralization of the movement manifests itself by an increase in absorption in the hemisphere involved. A spatial Full Width at Half Maximum (FWHM) of 6mm is observed for the equivalent cortical absorption due to activation. It shows that our method is able to provide qualitatively reliable DOCM results, localized and characterized.

The relation between the quantitative reconstruction and the volume absorption activation is determined by the volume convolution in eq.(7.2), and varies with depth.

Speaking about performance, the computation of the Jacobian was completed in 27 minutes, a time which is still longer than the previous FEM computation (11 minutes) but actually identical to the BEM-FEM. Although the BEM-FEM computation was a 3D reconstruction, this indicates that the BEM DOCM, can be envisaged as a practical reconstruction method comparable to the ones described before in subsection 2.2.1.3 for frequency domain data.

7.5 Discussion and conclusions

The DOCM addresses the problems arising from erroneous interpolation and gives an insight on the localization of the sampled region. We developed a BEM DOCM method able to localize the perturbations to the NIR signal originated from activation in the brain. By testing it on simulated, phantom and *in vivo* data, we demonstrated its ability to accurately find the position of the projection of these perturbations on the surface of the cortex. However, the dimensionless ECA obtained with the BEM is not easily interpreted and transformed into a Hemoglobin/Total Hemoglobin ratio (HbO_2/Hb_{total}). This drawback needs further analysis if the ECA is to be used in a similar fashion than the absorption coefficient.

With our simple surfaces-based model, we did not explicitly model the influence of the

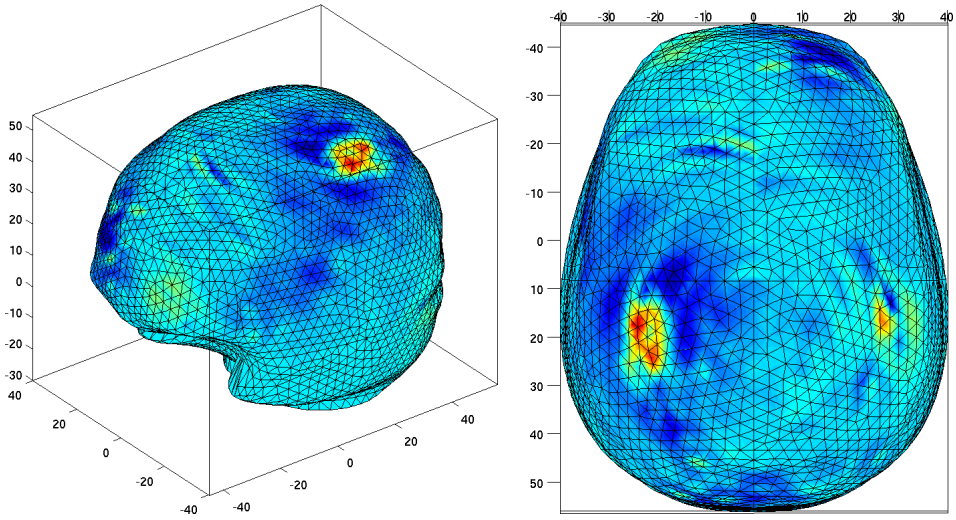

Figure 7.4: Side and top views of a cortical map of the activated brain - the primary motor and somatosensory cortices activation is clearly visible. This position corresponds to the arm region as it can be seen in [8]. Notice that the two foci visible on the left hemisphere are not really separated and that such features are below the resolution.

CSF, although this is also possible within a BEM framework. Instead we restricted the reconstruction to the cortex, as this is the key feature of a measurement passing through this region of the brain [5].

Setting up the BEM DOCM computation is simple, once anatomical data can be obtained. This can be done with the deformation of an existing atlas respective to measured fiducials during the experiment, like in our case, or with the help of individual anatomically-resolved scans (MRI, X-Ray). The meshes coming out of MRI reconstruction programs such as BrainSuite (http://brainsuite.usc.edu/) just need to be simplified (with a tool similar to the Türk/Lindström memoryless surface mesh simplification algorithm [286] from the Computer Graphics Algorithms Library algorithm embedded in the ISO2MESH [287] MATLAB package) and are ready to use in our BEM DOCM code with minimum modification. As soon as a surface mesh is obtained, which is usually the first step taken after segmentation, the BEM DOCM can be used. After the initial building of a Jacobian for the problem, subsequent measurements on the same subject could be analysed in real time, since the actual reconstruction time is less than one second.

Chapter 8

An Acceleration Method for the BEM

8.1 Introduction

8.1.1 Principles of the FMM

Basic identity The FMM is based on a decomposition of an exponential radial function on a basis of spherical Hankel and Bessel functions as described in the eq.(8.1), the addition theorem found in [240, 288]. Since most of the FMM literature uses a notation different to ours, our wave number ϖ is transformed into $\kappa = -\imath\varpi$. All the polynomials are taken as defined in [288]. This identity is illustrated by the Figure 8.1 which also describes the variables.

$$\frac{e^{-\imath\kappa|\mathbf{X}+\mathbf{d}|}}{|\mathbf{X}+\mathbf{d}|} = -\imath\kappa\sum_{l=0}^{\infty}(-1)^l(2l+1)\,j_l(\kappa d)h_l^{(2)}(\kappa X)P_l(\mathbf{d},\mathbf{X}) \tag{8.1}$$

with

- j_l: Bessel function of degree l
- $h_l^{(i)}$: spherical Hankel function of degree l of the i^{th}kind, $i = \{1,2\}$
- P_l: Legendre polynomial of degree l

Since Bessel's function is multiplied by a Legendre polynomial, the idea is to express this multiplication through a plane wave decomposition with radiations going in all directions.

FMM decomposition From this theorem, one can write the starting equation of the FMM which exhibits the separation of the terms coming from centers of cells (O_1 and O_2) from the terms

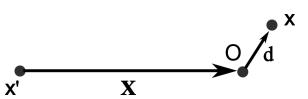

Figure 8.1: Decomposition of a radial operation between a point x and a point x' - an intermediary point O is used where $|\mathbf{X}|$ distance between x' and O is far greater than $|\mathbf{d}|$, distance between O and x.

coming from the individual nodes in the cells as seen in eq.(8.2), edited from [289]. A straightforward explanation of the process can be found in [239]. The sum on p is a (surface-) weighted (w_p) sum on unit vectors $\mathbf{s_p}$ taken on the unit sphere (spherical quadrature), while the sum on L is a serie.

$$\frac{e^{-\imath\kappa|\mathbf{x}-\mathbf{y}|}}{|\mathbf{x}-\mathbf{y}|} = \sum_p w_p e^{-\imath\kappa(\mathbf{s_p},\mathbf{x}-\mathbf{O_1})} T_{L,\mathbf{O_1}-\mathbf{O_2}}(\mathbf{s_p}) e^{-\imath\kappa(\mathbf{s_p},\mathbf{O_2}-\mathbf{y})} \tag{8.2}$$

in which T is the transfer function given by:

$$T_{L,\mathbf{O_1}-\mathbf{O_2}}(\mathbf{s_p}) = \sum_{l=0}^{L} \frac{\kappa(-\imath)^{l+1}(2l+1)}{4\pi} h_l^{(2)}(\kappa|\mathbf{O_1}-\mathbf{O_2}|) P_l(cos(\mathbf{s_p},\mathbf{O_1}-\mathbf{O_2}))$$

The geometrical translation of these principles can be illustrated with the Figure 8.2.

Example An example with Green's function (G) can help to understand what the underlying maths are. Suppose that we want to solve eq.(8.3) on the surface Γ of Figure 8.2.

$$\int_\Gamma G(\mathbf{r},\mathbf{r}')U(\mathbf{r})d^2\mathbf{r} \quad = \quad q(\mathbf{r}) \tag{8.3}$$

We define the matrix H with the entries $H_{kk'} = \int_{\Gamma_{k'}} G(\mathbf{r_k},\mathbf{r}')d^2\mathbf{r}'$, k corresponding to the element index. In the particular case of the interaction between $\mathbf{x}$ and the points $\mathbf{y}$, the computation of matrix-vector multiplications is similar to the one described in eq.(8.4). It happens between one node of the cell 1 where $\mathbf{x}$ belongs and whose center is $\mathbf{O_1}$, and all the nodes $\mathbf{y}$ of the cell 2 whose center is $\mathbf{O_2}$, C being the vincinity of $\mathbf{O_2}$, i. e. the cell 2. We notice that the shape and test functions are simplified to the maximum.

$$H_{xy}U_y = \sum_{p\ (unit\ sphere)} w_p \left[e^{-\imath\kappa(\mathbf{s_p},\mathbf{x}-\mathbf{O_1})} T_{L,\mathbf{O_1}-\mathbf{O_2}}(\mathbf{s_p}) \int_{\Gamma\cap C(\mathbf{O_2})} e^{-\imath\kappa(\mathbf{s_p},\mathbf{O_2}-\mathbf{y})} d^2\mathbf{r}'\right] U_y \tag{8.4}$$

Some of the basic features of eq.(8.4) are of primary importance:

- This formula is a decomposition of Green's function $\frac{e^{-\imath\kappa\|\mathbf{r}-\mathbf{r}'\|}}{4\pi\|\mathbf{r}-\mathbf{r}'\|}$ to compute its product with a vector
- T represents a diagonal form which contains the information about the physical problem's equation
  - it is well-known in the Helmholtz and Laplace equations cases but not in the equa-

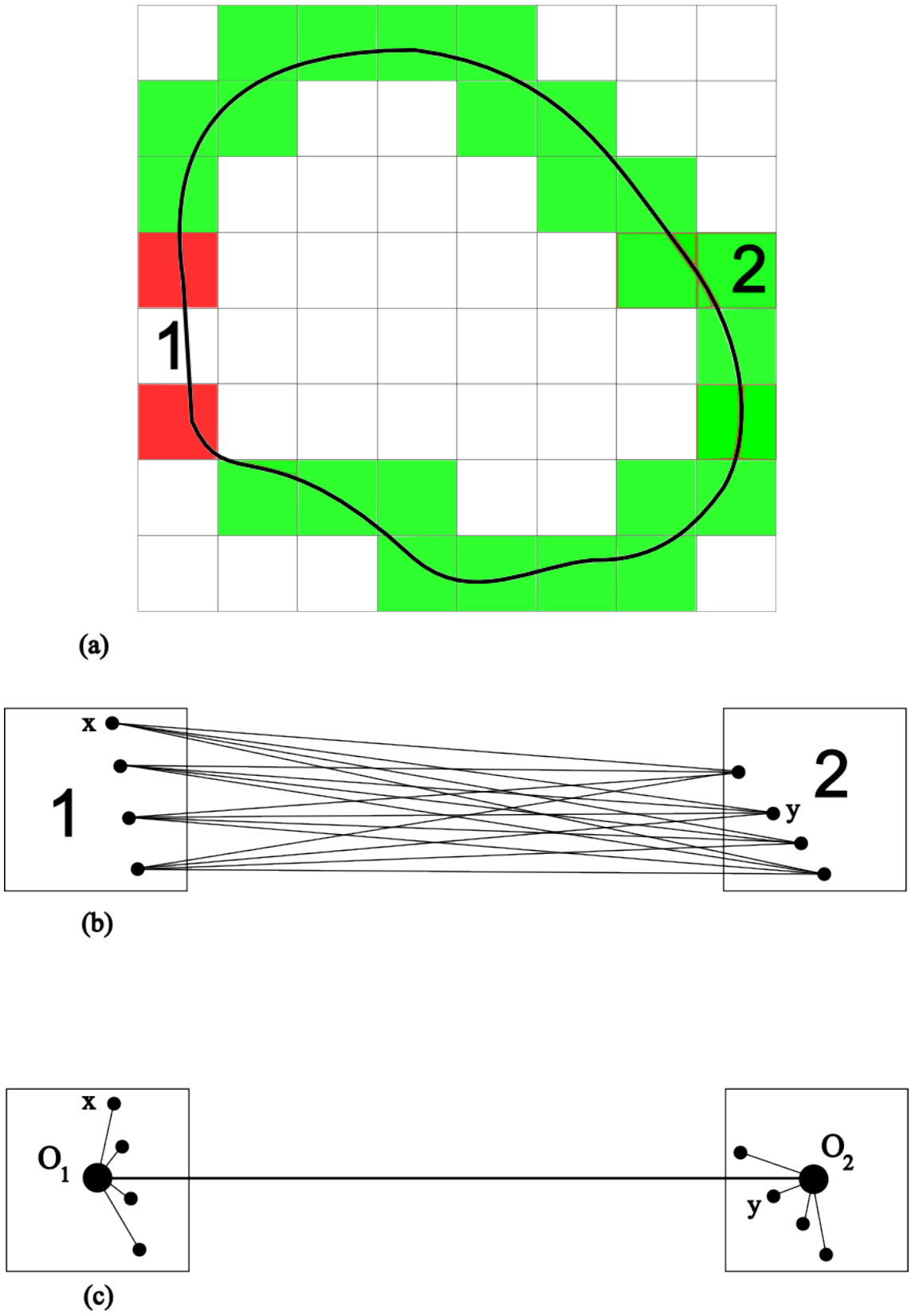

Figure 8.2: Single-level FMM for the 2D domain in black. (a) Near interactions with the cell 1 in red, far interactions in green; (b) old matrix-vector mutiplication scheme illustrated with black lines which underline the large number of operations to perform; (c) FMM matrix-vector multiplication scheme

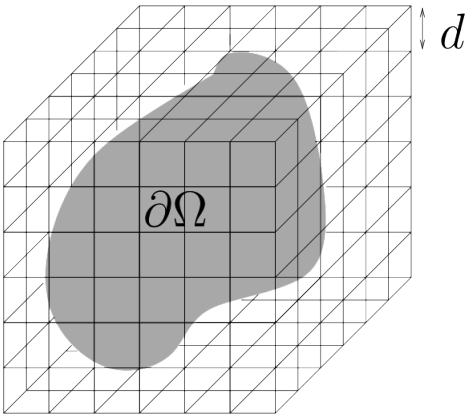

Figure 8.3: Single-level cells, courtesy of Dr. M. Bonnet

tion of the diffusion approximation (equivalent to a Helmholtz equation with a significantly imaginary wave number)

  - T is also linked to p, the number of points taken on the unit sphere, since T has to be reduced to its first terms in order to avoid a factorial divergence - this truncature is a function of p

- The integrals, all non singular, are only performed within the cell 2 considered

8.1.1.1 Single level implementation

A single-level implementation of the FMM creates a 3D grid (see Figure 8.3) in which the medium is contained. The FMM algorithm is then simply applied to the grid.

Compared to a normal full-matrix computation which requires $O(N^2)$computations, this only results in doing $O(N^{\frac{3}{2}})$ with N number of degrees of freedom [239].

8.1.1.2 Multilevel case

In the multilevel implementation, the explanation and development becomes much more difficult to do. It has been proven to reduce the complexity to its best known value of $O(Nlog(N))$ [289].

It uses an octree in subdividing the cells of the previous level in eight. The adjacent cells table then evolves, leading to a change in the truncature of T and then of p_{max} itself. An upward pass is first done in which values of the sum and truncature are passed from the leaf (lowest) level to the level 2 (highest level consisting of a 4x4x4 grid). Then, a downward pass computes the final value of 8.4. This process is described in more details in Chaillat *et al* article about multilevel Fast Multipole-BEM [290].

8.1.1.3 Preconditioning

The creation of the sparse matrix of near interactions allows the use of common preconditioners, such as the Incomplete LU (ILU) [291, 292] from this matrix. Some other techniques have been tested like the Frobenius-norm minimization preconditioner which requires, in the multilevel FMM case, the creation of a second octree [293]. In all these cases, the complexity law is not changed but the acceleration of the computation can be very significant. They also have never been tested in the context of lossy media. However, in the context of this thesis, they have not been studied.

8.1.1.4 Multidomain case

The particular treatment of nested regions is described later in this chapter .

The general multidomain case contains more empirical thinking. Actually, single-domain computations are performed and the interactions between the domains are later taken in account in a linear combination of the contributions to the matrix-vector product. This assembly of weighting coefficients must include:

- the interface conditions (continuities and boundary conditions)
- a treatment of the triple points (belonging to more than two domains)

An example in a geological continuum mechanics case is detailed in Chaillat *et al* second publication [237].

8.1.2 Choice of the method

We have chosen to implement the single level FMM and to apply it to one or more of our BEM-FEM or BEM DOCM cases. This choice has been made because of the small number of degrees of liberty we would be dealing with ($N_{dof} < 10^5$). The operations to perform are the following:

1. Division of the space in cells
2. Partial computation of the BEM Matrix (see section 8.3)
3. Computation of the Excitation vectors (Fourier transform of the basis functions)
4. Computation of the Transfer function
5. Fast Matrix-Vector multiplication - integration in GMRES or another solver

8.2 Simplified BEM with FMM

For the purpose of our study, we developed a new BEM code, which is identical to the existing described in section 3.2 but which, instead of using quadratic shape functions uses constant

functions over the elements. It is called VENOM.This is believed to result in a significant acceleration of the computation and a simplification of the implementation of the FMM (see subsection 8.4.1).

The difference with the previous code lies in the discretization, the integration scheme and the whole numerical implementation in general. All the code is in MATLAB.

The discrete BEM system is obtained from the BIE by choosing a basis representation for the functions U_i and V_i, and an observation set for the layer potential functions. We use a piecewise constant basis for U_i, V_i defined on the surfaces Γ_i and a collocation method for the observation set. Each surface Γ_j is discretised by n_j vertices $\mathbf{N}_{j,k}; k = 1...n_j$, with U_j and V_j approximated by the basis values $\{u_{j,k}\}$ defined on each element:

$$U_j(\mathbf{r}) \approx \sum_{k'=1}^{n_j} U_{j,k'} u_{j,k'}(\mathbf{r}), \quad V_j \approx \sum_{k'=1}^{n_j} V_{j,k'} u_{j,k'}(\mathbf{r}) \tag{8.5}$$

The discretisation of the operators (3.18) and (3.19) leads to $n_j \times n_{j'}$ dense matrices $A^{(i)}_{jj'}$, $B^{(i)}_{jj'}$, with entries

$$A^{(i)}_{jj'}(k,k') = \left\langle \delta(\mathbf{N}_{j,k}), \mathscr{A}^{(i)}_{j,j'} u_{j',k'}(\mathbf{r}) \right\rangle_{\Gamma_j}, \tag{8.6}$$

$$B^{(i)}_{jj'}(k,k') = \left\langle \delta(\mathbf{N}_{j,k}), \mathscr{B}^{(i)}_{j,j'} u_{j',k'}(\mathbf{r}) \right\rangle_{\Gamma_j} \tag{8.7}$$

with $k' \in 1...n_{j'}$ and $k \in 1...n_j$.

In the actual implementation, the basis functions are constant, and the non-singular and singular integrals are treated with Gaussian schemes, with integration points being taken respectively on the triangle and the square [24, 9]. The planar triangular elements used result in the existence of only one type of singular integrals, the one which involves Green's function and not its derivative. The integration of a function on an element is performed following this formula:

$$\int_\Gamma f(\mathbf{r}) d^2\mathbf{r} \to \int_\tau f(\mathbf{r}(\xi)) J(\xi) d\xi \to \sum_{h=1}^{7 \; or \; 36} f(\mathbf{r}(\xi_\mathbf{h})) J(\xi_\mathbf{h}) a_h \tag{8.8}$$

- In the triangle case, only a simple change from global (r_x, r_y, r_z) to local coordinates (ξ_1, ξ_2) is needed:

$$\mathbf{r} = \mathbf{r^1} + \xi_1(\mathbf{r^2} - \mathbf{r^1}) + \xi_2(\mathbf{r^3} - \mathbf{r^1}) \tag{8.9}$$

where the superscript refers to the position of a node in the element and the Gaussian

h	$\xi_{1,h}$	$\xi_{2,h}$	a_h
1	0.333333333333333	0.333333333333333	0.1125
2	0.059715871789769	0.470142064105115	0.0661970763942531
3	0.470142064105115	0.059715871789769	0.0661970763942531
4	0.470142064105115	0.470142064105115	0.0661970763942531
5	0.797426985353087	0.101286507323456	0.0629695902724136
6	0.101286507323456	0.797426985353087	0.0629695902724136
7	0.101286507323456	0.101286507323456	0.0629695902724136

Table 8.1: Gaussian points and weights for the triangle

h	$\xi_{1,h}$	$\xi_{2,h}$	a_h
1	-0.93246951420315202781	-0.93246951420315202781	0.17132449237917034504
2	-0.66120938646626451366	-0.66120938646626451366	0.36076157304813860757
3	-0.23861918608319690863	-0.23861918608319690863	0.46791393457269104739
4	0.23861918608319690863	0.23861918608319690863	0.46791393457269104739
5	0.66120938646626451366	0.66120938646626451366	0.36076157304813860757
6	0.93246951420315202781	0.93246951420315202781	0.17132449237917034504

Table 8.2: Gaussian points and weights for the square - they result in a concentration of points around the singular corner of the sub-triangle which is a singular side in the square - see [9])

points and weights are in Table 8.1. The Jacobian is the area of the element.

- In the case of the singular integrations of Green's function on the flat triangular elements, the elements are divided in three sub-triangles. Each of them is then transformed in squares, following [24, 9]. The conversion is simple:

$$\mathbf{r} = \mathbf{r^1} + \frac{1}{4}(1+\xi_1)(1-\xi_2)(\mathbf{r^2}-\mathbf{r^1}) + \frac{1}{4}(1+\xi_1)(1+\xi_2)(\mathbf{r^3}-\mathbf{r^1}) \tag{8.10}$$

and the Gaussian points and weights are in Table 8.2. The Jacobian of this transformation is $J = \frac{1}{8}(1+\xi_1)\Delta$ with Δ being the area of the flat sub-triangle of the element of the mesh.

Considering these changes in the discretization, the VENOM matrix is built the same way than the quadratic BEM (see subsection 3.2.2).

8.3 Theory of the FMM

8.3.1 Decomposition and solving procedure

The basic decomposition of a surface of which the so-called Coifman notation is taken from [239]. It states that m refers to the cell index, α to the index of an element within a cell m and n refers to the global index of an element. So, to each element corresponds a set of three numbers n, m, α.

In order to simplify the notation, we also define the quantities:

- θ_p: polar angle of the spherical quadrature point of index $p = 1 \dots N$
- T_p: FMM transfer function evaluated at the spherical quadrature point of index $p = 1 \dots N$
- N_e^α: number of elements containing the node α
- ξ_γ: quadrature position of the non-singular BEM integration scheme of index $\gamma = \{1 \dots N_e\}$ in the designated elements
- $\hat{\nu}_\gamma$: quadrature unit normal vector of the non-singular BEM integration scheme at the position ξ_γ
- $J(\xi_\gamma)$: value of the non-singular BEM quadrature Jacobian at the position ξ_γ
- a_{ξ_γ}: quadrature weight of the non-singular BEM integration scheme at the position ξ_γ

Green's function When Green's function is defined as:

$$G(\mathbf{r},\mathbf{r}') = \frac{e^{-\imath\kappa\|\mathbf{r}-\mathbf{r}'\|}}{4\pi\|\mathbf{r}-\mathbf{r}'\|} \tag{8.11}$$

Then its derivative along a normal unit vector $\hat{\nu}$ to the surface considered is written:

$$\frac{\partial G}{\partial \nu} = (1+\imath\kappa\|\mathbf{r}-\mathbf{r}'\|)\frac{e^{-\imath\kappa\|\mathbf{r}-\mathbf{r}'\|}}{4\pi\|\mathbf{r}-\mathbf{r}'\|^3}(\mathbf{r}'-\mathbf{r},\hat{\nu}) \tag{8.12}$$

Basic Fast Multipole decomposition - Gauss-Legendre quadrature Thanks to simulations and additional work on quadratures on the unit sphere, we have chosen the decomposition described in eq.(8.13). O and O' are respectively the centers of the cell containing $\mathbf{r}$ and the cell containing $\mathbf{r}'$.

$$\begin{aligned} \tfrac{e^{-\imath\kappa\|\mathbf{r}-\mathbf{r}'\|}}{4\pi\|\mathbf{r}-\mathbf{r}'\|} &= \tfrac{1}{4\pi}\textstyle\sum_{p=1}^{N} w_p T_p e^{-\imath\kappa(\mathbf{s}_p,\mathbf{r}-\mathbf{r}'-\mathbf{OO}')} \\ T_p &= \tfrac{1}{4\pi}\textstyle\sum_{l=0}^{L} \kappa(-\imath)^{l+1}(2l+1)h_l^{(2)}(\kappa\|\mathbf{OO}'\|)P_l(\tfrac{\mathbf{OO}'}{\|\mathbf{OO}'\|},\mathbf{s_p}) \end{aligned} \tag{8.13}$$

One can also, of course, decompose the derivative as in eq.(8.14).

$$(1+\imath\kappa\|\mathbf{r}-\mathbf{r}'\|)\frac{e^{-\imath\kappa\|\mathbf{r}-\mathbf{r}'\|}}{4\pi\|\mathbf{r}-\mathbf{r}'\|^3}(\mathbf{r}'-\mathbf{r},\hat{\nu}) = \frac{-\imath\kappa}{4\pi}\sum_{p=1}^{N} w_p T_p e^{-\imath\kappa(\mathbf{s_p},\mathbf{r}-\mathbf{r}'-\mathbf{OO}')}(\mathbf{s_p},\hat{\nu}) \tag{8.14}$$

BEM integrals decomposition Once the expression of Green's function and its derivative are established, the writing of the A and B BEM integrals in section 3.2 and [24] is straightforward as it can be seen in eq.(8.15), with α corresponding to the indices in the cell m (positions noted $\mathbf{r}$, center O) and β the indices in the cell m' (positions noted $\mathbf{r}'$, center O'). N_e^β elements contain the node β. One notices that the integration operation is trivial and does not contain any singularity.

$$\begin{aligned} A_{\alpha\beta} &= \frac{-\imath\kappa}{4N_e\pi}\sum_{p=1}^{N} w_p T_p e^{-\imath\kappa(\mathbf{s_p},\mathbf{r}_\alpha-\mathbf{O})}\sum_{\gamma=1}^{N_e^\beta}(\mathbf{s_p},\hat{\mathbf{v}}_\gamma)\sum_{\xi_\gamma} e^{-\imath\kappa(\mathbf{s_p},\mathbf{O}'-\xi_\gamma)}J(\xi_\gamma)w_{\xi_\gamma} \\ B_{\alpha\beta} &= \frac{1}{4N_e\pi}\sum_{p=1}^{N} w_p T_p e^{-\imath\kappa(\mathbf{s_p},\mathbf{r}_\alpha-\mathbf{O})}\sum_{\gamma=1}^{N_e^\beta}\sum_{\xi_\gamma} e^{-\imath\kappa(\mathbf{s_p},\mathbf{O}'-\xi_\gamma)}J(\xi_\gamma)w_{\xi_\gamma} \end{aligned} \tag{8.15}$$

In the particular case of constant shape functions, the sum on γ is useless: α and β are element indices.

Algorithm (inspired from [239], [240] and [289])

1. Division of the N nodes (or elements) mesh into $\sqrt{N}$ cells

2. Building of a sparse BEM matrix which excludes interactions coming from non-adjacent cells called M

   (a) The non-adjacent cubic cells rule is always applicable and is translated by the exclusion of interactions corresponding to couples of cells whose centers are separated by a distance $> \sqrt{3}a$ with a being the edge length [294, 295]

   (b) In our particular MATLAB implementation, because of its size, the matrix is built as a sparse structure

3. Computation of the converse excitation vectors eq.(8.16) - Coifman *et al*'s notation emphasizes the indices for the elements $n(m,\alpha)$ actually used in the program

$$C_{n(m,\alpha)}(\mathbf{s_p}) = e^{-\imath\kappa(\mathbf{s_p},\mathbf{r}_{n(m,\alpha)}-\mathbf{O}_m)} \tag{8.16}$$

4. Computation of A and B excitation vectors eq.(8.17)

$$\begin{aligned} V^A_{n(m,\alpha)} &= (\mathbf{s_p},\hat{\mathbf{v}}_n)\sum_{h=1}^{7} e^{-\imath\kappa(\mathbf{s_p},\mathbf{O}_m-\xi_h(n))}a_h \\ V^B_{n(m,\alpha)} &= \sum_{h=1}^{7} e^{-\imath\kappa(\mathbf{s_p},\mathbf{O}_m-\xi_h(n))}a_h \end{aligned} \tag{8.17}$$

5. Computation of the transfer function eq.(8.18)

$$\begin{aligned} T_p^A &= \frac{-\iota\kappa}{4\pi} w_p T_p \\ T_p^B &= \frac{1}{4\pi} w_p T_p \end{aligned} \tag{8.18}$$

6. Solving of the problem by doing matrix-vector operations in an iterative solver which computes A and B

   (a) Computation of the far fields of the cells here with vector I (8.19)

$$\begin{aligned} S_p^A(m) &= \sum_\alpha V_{n(m,\alpha)}^A(\mathbf{s_p}) I_{n(m,\alpha)} \\ S_p^B(m) &= \sum_\alpha V_{n(m,\alpha)}^B(\mathbf{s_p}) I_{n(m,\alpha)} \end{aligned} \tag{8.19}$$

   (b) Computation of the Fourier components eq.(8.20) of the field in the neighbourhood of the m cell

$$\begin{aligned} G_p^A(m) &= \sum_{m'} T_p^A(m,m') S_p^A(m') \\ G_p^B(m) &= \sum_{m'} T_p^B(m,m') S_p^A(m') \end{aligned} \tag{8.20}$$

   (c) Computation of the matrix-vector product eq.(8.21) - example of a single surface-integral treated region

$$\begin{aligned} MI &= M \cdot I \\ MatrixI_{n(m,\alpha)} &= MI_{n(m,\alpha)} + \sum_{p=1}^{N} C_{n(m,\alpha)}(\mathbf{s_p})\left(\frac{G_p^B(m)}{2D} + G_p^A(m)\right) \end{aligned} \tag{8.21}$$

In the software, the Lebedev quadrature of the sphere is used, due to its high efficiency in the small number of points needed to integrate functions on the sphere [296]. The code which generates the points has been written by Dr. R. Parrish. In practice, the quadrature weights given have to be multiplied by $sin(\theta_p)$.

8.3.2 Specifics of the Diffusion Approximation

There exists a fundamental difference between the Diffusion Approximation and the other aforementioned implementation of the FMM in seismology, electromagnetics, etc. Actually, the DOT FMM-BEM has a partially real and partially complex wave number, and in practice, it is mostly imaginary. This negatively impacts the convergence of the computation of the transfer function, because of numerical approximations in the Hankel functions.

The particular case of a lossy space (influence of μ_a and f) has been studied only by Geng *et al* so far [240] in very simple single-layer geometries (half-space) and with a small imaginary/real ratio (maximum 0.32, while our standard ratio is 9.7 when $\mu_s = 1mm^{-1}$, $\mu_a =$

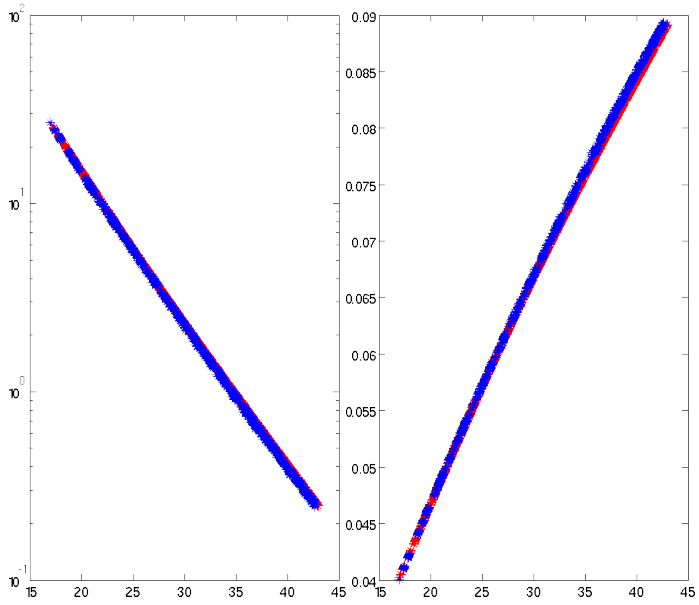

Figure 8.4: Quadratic shape functions BEM (red) against constant shape functions BEM (blue) on a sphere model - amplitude on the left and phase on the right with the distance to the source in mm as an abscissa

$0.01mm^{-1}$, $f = 100MHz$, n= 1). They found that the transfer function must be truncated so that L is chosen large enough but must not greatly exceed $|k\mathbf{OO_{max}}'|$. This is ensured by the non-adjacent cells rule [294, 295].

In our implementation, we actually realized that the impact is minimal and excellent convergence rates were reached with relatively low L as seen in the following sections. A rule of thumb is given in eq.(8.22), a formula clearly inspired from the usual computation of L explicitly described in ([294]).

$$L = |\kappa a\sqrt{3} + ln(\pi + \kappa a\sqrt{3})| + 6 \tag{8.22}$$

8.4 Results

8.4.1 Accuracy of the constant shape functions BEM code

In order to validate the accuracy of VENOM against our quadratic BEM code [297], we tested it on a simple 33mm radius high resolution sphere (17618 quadratic nodes and 8808 elements) with these optical parameters: $\mu_s = 1mm^{-1}$, $\mu_a = 0.01mm^{-1}$, $f = 100MHz$, n= 1. The Gaussian source is placed at the surface. The results are shown in Figure 8.4. The global errors in L_2-norm on both the amplitude and phase are around 1%. One however notices the limits of a constant shape function approach and the fact that the discretization of VENOM is always lower than the quadratic BEM's because the former is element-based while the latter is node-based.

MATRIX BUILDING/SETUP	VENOM	BEM	Quadratic nodes	Elements
Sphere	379s	802s	17618	8808
High resolution baby brain	204s	450s	13498	6748
Baby scalp	76s	162s	8190	4094
Baby skull	63s	131s	7374	3686
Baby brain	32s	64s	5130	2564
Mouse	101s	219s	9494	4746

SOLVING	VENOM	BEM
Sphere	6s	51s
High resolution baby brain	17s	138s
Baby scalp	6s	48s
Baby skull	5s	41s
Baby brain	3s	21s
Mouse	15s	191s

Table 8.3: Computational speed of VENOM vs BEM with Gaussian sources on the surface of the meshes (GMRES solver)

Since the entire code is in MATLAB, we have performed a vectorization of nearly all the operations and the use of only a single loop over the elements to build the system matrix. The main idea is always to compute many vector-vector operations at the same time while keeping all the different vectors in a single matrix and prohibiting any cross-talking. This code is faster than the quadratic BEM in all configurations, including those outlined in the Table 8.3.

8.4.2 Acceleration of VENOM-FMM

The complete single-level FMM decomposition has been implemented using VENOM. This yielded accelerations up to 2-3 times compared to the normal VENOM in all cases.

8.4.2.1 Implementation details

The practical writing of the matrix K (see 8.2) requires the splitting of the matrices A and B. For example, in three layers, eq.(8.23) shows that A and B should be able to be separated into parts in which the reference to the outer (0), the inner layer (1) and the innermost layer (2) is known. However, in the algorithm described in 8.3.1, V^A and V^B are separated and indexed along the cell number m. A cell, by its nature, can contain nodes in the outer and inner layers alike. This is why, in the MATLAB script, we split the test vector $(U_0\ U_1\ V_1\ U_2\ V_2)$ as described in eq.(8.24).

$$K = \begin{pmatrix} A_0^{00} + \frac{1}{2}\mathbb{I} + \frac{B_0^{00}}{2D_0} & A_0^{01} & -\frac{B_0^{01}}{D_0} & 0 & 0 \\ A_0^{10} + \frac{B_0^{10}}{2D_0} & A_0^{11} + \frac{1}{2}\mathbb{I} & -\frac{B_0^{11}}{D_0} & 0 & 0 \\ 0 & A_1^{11} + \frac{1}{2}\mathbb{I} & \frac{B_1^{11}}{D_1} & A_1^{12} & -\frac{B_1^{12}}{D_1} \\ 0 & A_1^{21} & \frac{B_1^{21}}{D_1} & A_1^{22} + \frac{1}{2}\mathbb{I} & -\frac{B_1^{22}}{D_1} \\ 0 & 0 & 0 & A_2 + \frac{1}{2}\mathbb{I} & \frac{B_2}{D_2} \end{pmatrix} \tag{8.23}$$

$$\begin{aligned} K \begin{pmatrix} U_0 \\ U_1 \\ V_1 \\ U_2 \\ V_2 \end{pmatrix} &= \begin{pmatrix} A_0^{00} + \frac{1}{2}\mathbb{I} & A_0^{01} & 0 & 0 & 0 \\ A_0^{10} & A_0^{11} + \frac{1}{2}\mathbb{I} & 0 & 0 & 0 \\ 0 & 0 & 0 & 0 & 0 \\ 0 & 0 & 0 & 0 & 0 \\ 0 & 0 & 0 & 0 & 0 \end{pmatrix} \begin{pmatrix} U_0 \\ U_1 \\ 0 \\ 0 \\ 0 \end{pmatrix} + \\ \frac{1}{D_0} \begin{pmatrix} B_0^{00} & 0 & B_0^{01} & 0 & 0 \\ B_0^{10} & 0 & B_0^{11} & 0 & 0 \\ 0 & 0 & 0 & 0 & 0 \\ 0 & 0 & 0 & 0 & 0 \\ 0 & 0 & 0 & 0 & 0 \end{pmatrix} \begin{pmatrix} \frac{U_0}{2} \\ 0 \\ -V_1 \\ 0 \\ 0 \end{pmatrix} + \begin{pmatrix} 0 & 0 & 0 & 0 & 0 \\ 0 & 0 & 0 & 0 & 0 \\ 0 & A_1^{11} + \frac{1}{2}\mathbb{I} & 0 & A_1^{12} & 0 \\ 0 & A_1^{21} & 0 & A_1^{22} + \frac{1}{2}\mathbb{I} & 0 \\ 0 & 0 & 0 & 0 & 0 \end{pmatrix} \begin{pmatrix} 0 \\ U_1 \\ 0 \\ U_2 \\ 0 \end{pmatrix} + \\ \frac{1}{D_2} \begin{pmatrix} 0 & 0 & 0 & 0 & 0 \\ 0 & 0 & 0 & 0 & 0 \\ 0 & 0 & B_1^{11} & 0 & B_1^{12} \\ 0 & 0 & B_1^{21} & 0 & B_1^{22} \\ 0 & 0 & 0 & 0 & 0 \end{pmatrix} \begin{pmatrix} 0 \\ 0 \\ V_1 \\ 0 \\ -V_2 \end{pmatrix} + \begin{pmatrix} 0 & 0 & 0 & 0 & 0 \\ 0 & 0 & 0 & 0 & 0 \\ 0 & 0 & 0 & 0 & 0 \\ 0 & 0 & 0 & 0 & 0 \\ 0 & 0 & 0 & A_2 + \frac{1}{2}\mathbb{I} & \frac{B_2}{D_2} \end{pmatrix} \begin{pmatrix} 0 \\ 0 \\ 0 \\ U_2 \\ V_2 \end{pmatrix} \end{aligned} \tag{8.24}$$

8.4.2.2 Single layer code - algorithmic complexity

In order to assess the optimality of our algorithm, we tested the law exposed in [239] where a single-level implementation of the FMM should have a computational time in $N^{\frac{3}{2}}$ of the degrees of freedom of the problem. In our particular case, the number of degrees of freedom is the number of elements. We tested spheres of 634, 1280, 2536, 3840, 5568, 7424, 8808, 10144, 17920 and 20480 surface elements with the optical parameters $\mu_s = 1mm^{-1}$, $\mu_a = 0.01mm^{-1}$, $n = 1$ in the frequency domain with $f = 100MHz$. The reference density of elements was that of the largest sphere (20480 elements and 50mm in radius): 0.65 elements per mm². A Gaussian source (see section 4.1.2) of unit intensity was placed on every sphere's surface.

Figure 8.5 shows that the law is respected in our algorithm. The fitting error, computed as the relative difference between the points and the line in L^2-norm is close to 1%.

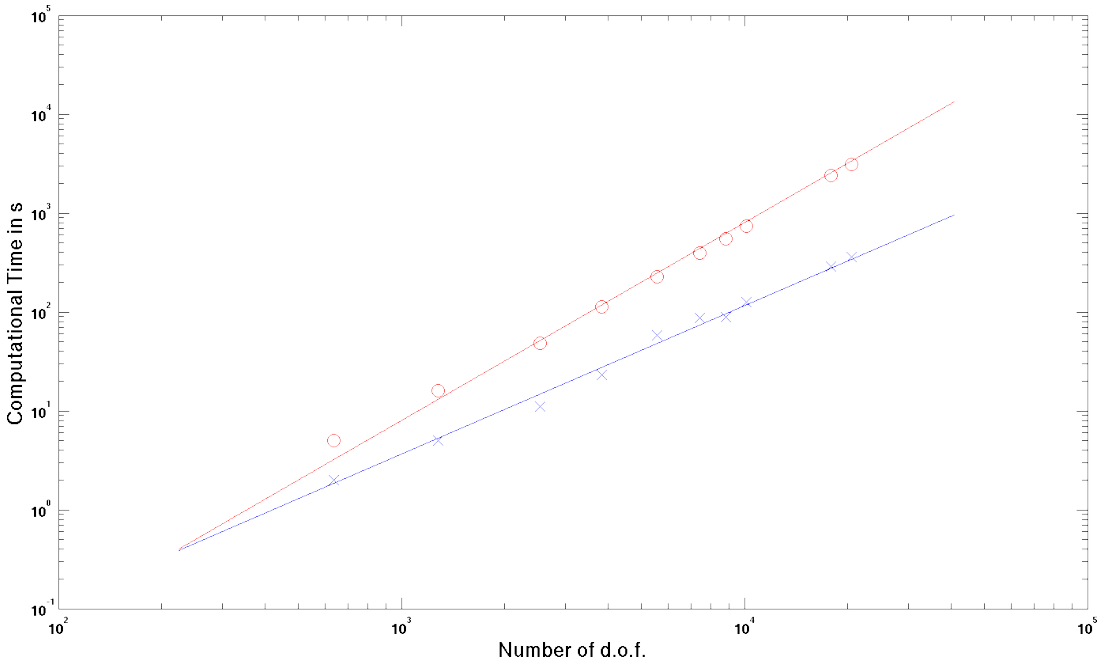

Figure 8.5: Evolution of the computational time of the FMM (blue) and VENOM (red) on constant discretization density spheres

8.4.2.3 Neonatal head

We use here the original normal resolution mesh of a neonate's head published by Tizzard *et al.* [285]. The difference with the one described in subsection 5.2 is mainly the discretization density. Furthermore, it is different from the one used in section 6.2 because no adaptation to the particular case of a live baby by warping it onto the optodes (see subsection 6.2.1) has been performed. However, the optical properties and frequency used were the same than in this BEM-FEM *in vivo* study. In total, this surface mesh contains 4094 elements for the scalp, 3686 elements for the skull and 2564 elements for the brain, which here results in 16594 degrees of freedom.

The forward model with a source on the surface shows a good agreement with VENOM with a relative solution difference in L^2-norm of $8.15 * 10^{-9}$. The global amplitude error (computed along the formula $\frac{|| \, |Solution| - |FMM \ Solution| \, ||}{||Solution||}$) is 0.02% and the global phase error 0.2% (computed with a similar scheme).

One should notice that, due to the amount of nodes involved, it is impossible to solve this problem with the existing quadratic BEM code, even with a computer with 32Go of Random Access Memory (RAM). In terms of computational speed the following results were obtained:

- 365s (FMM) versus 651s (VENOM) for the setup of the problem
- 101s (FMM) versus 347s (VENOM) for the solving

The setup includes steps 1-5 of the FMM algorithm in subsection 8.3.1 versus the matrix building for VENOM. The solving for the FMM is the step 6.

8.5 Conclusions

The acceleration of the BEM code brought by the development of the FMM and VENOM opens new perspectives for the usage of the BEM in optical imaging. So far, the mesh size has been a major obstacle. Due to the nature of the BEM matrix (which is full as described in subsection 2.1.2.3), the number of degrees of freedom often had to be reduced from FEM meshes or the like, as in [298]. With the FMM, this is not the case for most of the meshes like our three-layer example.

The FMM can be used to accelerate the BEM in any context, including DOCM and BEM-FEM. Both require, in a linear reconstruction context, the building of a Jacobian. This means that only the solving time is a limiting factor when the Jacobian is built using the adjoint method [2]. The FMM provides a very significant acceleration in this domain.

We understand that beyond 10^5 degrees of freedom, the single-level approach developed here is not sufficient to be really interesting. The largest multi-layer problem tested is a three-layered neonate's head merely identical to the one presented in section 8.4 but of a higher resolution, with in total 44356 degrees of freedom. The VENOM matrix could not fit into memory but the FMM still worked. The solving time, however, started to become slightly long (about 5 minutes for a source). One can imagine that doubling the number of degrees of freedom would make the multi-level FMM advantageous. We indeed intend to develop this method for DOI in the near future. This would enable us to work on very high resolution meshes which would include detailed topographical information on the cortex, including more particularly the sulci and gyri.

Chapter 9

Summary and future work

We have developed genuinely innovative numerical methods for diffuse optical imaging based on the BEM who have proven their worth by supporting my initial hypotheses with trustworthy results. Despite the intense work which has been needed to design them, they are now ready to be used by researchers. This opens a new field of opportunities and in the near future, the research in this domain will be easier to carry out and more adaptive, leading us closer to a wider availability and usage of near-infrared techniques in the clinic.

On the BEM-FEM

The BEM-FEM has indeed been able to aggregate the advantages of the BEM, which are mainly its meshing simplicity and adaptability, with the reconstruction simplicity and accuracy of the FEM. It has shown that it does the work of a full FEM in a easier way (once the code is written) and with a comparable accuracy. More particularly, it has been proven that a patient-dependent technique relying on an atlas is possible and actually easy to foresee being implemented in more experimental contexts.

Other advantages will be found when further work will be done on the BEM-FEM in its integration with a radiosity technique to treat the problem of the non-scattering regions such as the CSF (see paragraph 2.1.1.4). In combination with the FMM, the then FMM-FEM will present a significant memory and time consumption improvement over the full FEM.

In this thesis, images were reconstructed using a linear single-step approach, after assuming that the background optical properties of the BEM and FEM regions were known. This is appropriate for optical tomography of brain function, and it will be straightforward to extend the method to non-linear image reconstruction where the optical properties of the overlying regions are treated as unknowns. This would push further the influence of the BEM-FEM in the inverse problem by adding variables to the reconstruction and having background properties determined by calculation and not by assumption and measurements from dead tissue as it is

System	Pre-requirements	Subject-specific data	Relevance of BEM-FEM
Infant brain	Atlas	Optode positions	Strong
Adult brain	Atlas	Optode positions	Strong
Breast	MRI	None	Practically irrelevant*
Limbs and others**	MRI/CT	None	None (no thin layers)
Small animal	Atlas	Outer surface at least	Beyond our scope***

Table 9.1: BEM-FEM applications (the atlases are general structures derived from anatomical obtained with MRI, CT or other techniques such as histology). *Except to treat separately a matching fluid and the breast tissue in a setup similar to [10]. **Joints and muscles. ***In this context, the modelling does not only involve thin layers but also entire organs which should be treated with a surface-integral approach; this is more complicated than the nested regions formulation presented in this thesis.

done nowadays.

Our new formulation, as presented in this thesis, requires the knowledge of the BEM layers' optical properties and their approximate location in the overall biological medium. In our in vivo reconstructions, this data is asssumed to be known at a sufficient level. Besides, other experiments could be done with perturbations of known optical properties to compare the values found with the BEM-FEM and the FEM. Our *in vivo* study does not include such a comparison since the actual optical properties of the activation are unknown. In the more general case of neural imaging, the inverse problem could be strongly modified, position of the thin layers covering the region of interest would need to be backed up by an anatomical investigation (XCT or MRI-type atlas). This is also only relevant when actual clear layers exist and is especially advantageous when they are thin (see Table 9.1).

We are thinking about using the BEM-FEM in the breast imaging and small animal imaging environments. Indeed, the BEM-FEM could allow the simplification of the treatment of matching fluids and other interfering layers appearing during the imaging of such subjects. In the more specific case of small-animal imaging, it could also help to take in account the thin layers surrounding the organ of interest, along with a simplified modelling of the neighbouring structures.

On the BEM DOCM

We have also demonstrated that the BEM DOCM is a possible, reliable and easy to implement alternative to the existing widely used Optical Topography techniques, if written in the continuity of my work. It also provides a certain localisation accuracy and adaptability abilities. Despite the simple multi-layered model, it is possible to represent the basic structures of the brain and even to indirectly take in account the influence of the CSF.

The ECA is currently not easily linked to the concentration of the different types of

Hemoglobin. Once this link will be found, further work could be done on the reconstruction at multiple wavelengths and a comparison with the conventional NIRS techniques could be performed. This would presumably display clearly the partial volume effect which affects the NIRS results. As of now, only cortical maps using the conventional approach could be constructed to compare with the BEM DOCM maps. This could be particularly interesting when comparing the number of artefacts between the two methods.

The remarks about the necessary *a priori* knowledge of the optical properties of the regions made previously about the BEM-FEM are also relevant to the BEM DOCM. However, the BEM DOCM presents the advantage over the BEM-FEM that it is possible to reconstruct the absorption on more than one surface. This could allow to monitor the changes on the extracerebral layers.

The BEM DOCM is envisaged to be used in adults with a more limited optode coverage of the scalp surface. Some data, correlated with other imaging modalities, has been acquired and is going to be analysed soon. The speed of the reconstruction is also an advantage when imaging the evolution of activations in the cortex, once the Jacobian has been pre-computed.

On the FMM

We hope that all these findings and possible usage of the BEM in DOI will soon not be tampered any more with arguments concerning the computational speed of the BEM. Our acceleration method, along with the simplifications performed on the code, have proven their efficiency on the commonly met discretisation situations. With a single layer or in multi-layered contexts, the single-level FMM has accelerated the BEM to more acceptable speeds.

We intend to further develop this technique and apply it systematically to the surface integral-treated problems. In order to be able to work on even more accurate structures, even to the extent of taking the raw high resolution MRI-generated meshes of the brain on a routine basis, we believe that our FMM technique will be upgraded to a multilevel one with preconditioners. They have been proven to accelerate the FMM dozens of times in other contexts in addition to the improvement brought by a multilevel implementation. This requires a sustained and difficult effort, due to the nature of the diffusion equation.

Bibliography

[1] A. Yodh and B. Chance, "Spectroscopy and imaging with diffusing light," Physics Today **48**, 34–40 (1995).

[2] S. R. Arridge, "Optical tomography in medical imaging," Inverse Problems **15**, R41–R93 (1999).

[3] B. Kanmani and R. M. Vasu, "Diffuse optical tomography using intensity measurements and the a priori acquired regions of interest: Theory and simulations," Physics in Medicine and Biology **50**, 247–264 (2005).

[4] W. Zhu, Y. Wang, Y. Yao, J. Chang, H. L. Graber, and R. L. Barbour, "Iterative Total Least-Squares Image Reconstruction Algorithm for Optical Tomography by the Conjugate Gradient Method," Journal of the Optical Society of America A **14**, 799–807 (1997).

[5] E. Okada, M. Firbank, M. Schweiger, S. R. Arridge, M. Cope, and D. T. Delpy, "Theoretical and experimental investigation of near-infrared light propagation in a model of the adult head," Applied Optics **36**, 21–31 (1997).

[6] S. R. Arridge, O. Dorn, V. Kolehmainen, M. Schweiger, and A. D. Zacharopoulos, "Parameter and Structure Reconstruction in Optical Tomography," Journal of Physics: Conference Series **135**, 012001 1–17 (2008).

[7] A. Gibson, R. M. Yusof, H. Dehghani, J. Riley, N. Everdell, R. Richards, J. C. Hebden, M. Schweiger, S. R. Arridge, and D. Delpy, "Optical tomography of a realistic neonatal head phantom," Applied Optics **42**, 3109–3116 (2003).

[8] E. Widmaier, H. Raff, and K. Strang, *Vander's human physiology: the mechanisms of body function*, p. 306 (McGraw-Hill Higher Education, 2008).

[9] A. D. Zacharopoulos, "Three-dimensional shape-based reconstructions in medical imaging," Ph.D. thesis, University College London (2004).

[10] R. Choe, A. Corlu, K. Lee, T. Durduran, S. D. Konecky, and M. Grosicka-Koptyra, "Diffuse Optical Tomography of Breast Cancer During Neoadjuvant Chemotherapy: A Case Study with Comparison to MRI," Medical Physics **32**, 1128–1139 (2005).

[11] A. Villringer and B. Chance, "Non-invasive optical spectroscopy and imaging of human brain function," Trends in Neurosciences **20**, 435–442 (1997).

[12] A. J. Welch and M. J. C. van Gemert, *Optical-Thermal Response of Laser-Irradiated Tissue* (Springer, 1995).

[13] G. Alexandrakis, F. R. Rannou, and A. F. Chatziioannou, "Tomographic Bioluminescence Imaging by Use of a Combined Optical-PET (OPET) System: a Computer Simulation Feasibility Study," Physics in Medicine and Biology **50**, 4225–4241 (2005).

[14] A. J. Chaudhari, F. Darvas, J. R. Bading, R. A. Moats, P. S. Conti, D. J. Smith, S. R. Cherry, and R. M. Leahy, "Hyperspectral and multispectral bioluminescence optical tomography for small animal imaging," Physics in Medicine and Biology **50**, 5421–5441 (2005).

[15] H. Dehghani, C. S. Davis, S. Jiang, B. Pogue, K. D. Paulsen, and M. S. Patterson, "Spectrally resolved bioluminescence optical tomography," Optics Letters **31**, 365–367 (2006).

[16] A. Joshi, W. Bangerth, K. Hwang, J. C. Rasmussen, and E. M. Sevick-Muraca, "Fully adaptive FEM based fluorescence optical tomography from time-dependent measurements with area illumination and detection," Medical Physics **33**, 1299–1310 (2006).

[17] V. Ntziachristos, "Fluorescence molecular imaging," Annual Review of Biomedical Engineering **8**, 1–33 (2006).

[18] B. T. Cox, S. R. Arridge, and P. C. Beard, "Estimating Chromophore Distributions from Multiwavelength Photoacoustic Images," Journal of the Optical Society of America A **26**, 443–455 (2009).

[19] H. Dehghani, B. W. Pogue, S. P. Poplack, and K. D. Paulsen, "Multiwavelength three-dimensional near-infrared tomography of the breast: Initial simulation, phantom and clinical results," Applied Optics **42**, 135–145 (2003).

[20] N. Liu, A. Sassaroli, and S. Fantini, "Paired-wavelength spectral approach to measuring the relative concentrations of two localized chromophores in turbid media: an experimental study," Journal of Biomedical Optics **12**, 051602 (2007).

[21] A. Joshi, W. Bangerth, and E. Sevick-Muraca, "Adaptive finite element based tomography for fluorescence optical imaging in tissue," Optics Express **12**, 5402–5417 (2004).

[22] Y. Lv, J. Tian, W. Cong, G. Wang, J. Luo, W. Yang, and H. Li, "A multilevel adaptive finite element algorithm for bioluminescence tomography," Optics Express **14**, 8211–8223 (2006).

[23] B. W. Pogue, X. Song, T. D. Tosteson, T. O. McBride, S. Jiang, and K. D. Paulsen, "Statistical analysis of nonlinearly reconstructed near-infrared tomographic images: Part i-theory and simulations," IEEE Transactions on Medical Imaging **21**, 755–763 (2002).

[24] J. Sikora, A. Zacharopoulos, A. Douiri, M. Schweiger, L. Horesh, S. Arridge, and J. Ripoll, "Diffuse photon propagation in multilayered geometries," Physics in Medicine and Biology **51**, 497–516 (2006).

[25] J. Ripoll, V. Ntziachristos, R. Carminati, and M. Nieto-Vesperinas, "The Kirchhoff Approximation for Diffusive Waves," Physical Review E **64**, 051917 (2001).

[26] A. H. Hielscher, A. D. Klose, A. K. Scheel, B. Moa-Anderson, M. Backhaus, U. Netz, and J. Beuthan, "Sagittal laser optical tomography for imaging of rheumatoid finger joints," Physics in Medicine and Biology **49**, 1147–1163 (2004).

[27] B. W. Pogue, M. S. Patterson, H. Jiang, and K. D. Paulsen, "Initial assessment of a simple system for frequency domain diffuse optical tomography," Physics in Medicine and Biology **40**, 1709–1729 (1995).

[28] E. Onate, M. Cervera, and O. C. Zienkiewicz, "A Finite Volume Format for Structural Mechanics," International Journal for Numerical Methods in Engineering **37**, 181–201 (1994).

[29] K. Ren, G. S. Abdoulaev, G. Bal, and A. H. Hielscher, "Algorithm for solving the equation of radiative transfer in the frequency domain," Optics Letters **29**, 578–580 (2004).

[30] V. Y. Soloviev, "Mesh Adaptation Technique for Fourier-domain Fluorescence Lifetime Imaging," Medical Physics **33**, 4176–4183 (2006).

[31] A. D. Zacharopoulos, J. Sikora, and S. R. Arridge, "Reconstruction of 3D region boundaries in Optical Tomography using Parametric Surfaces and BEM," in "Proceedings of the Institute of Mathematics and its Applications, Third International Conference on Boundary Integral Methods: Theory and Applications, 14-18 September 2004," .

[32] J.-B. Thibaud, R. Carminati, and J.-J. Greffet, "Scattering of a diffusive wave by a subsurface object," Journal of Applied Physics **87**, 7638–7646 (2000).

[33] J. Sikora, *Boundary Element Method for Impedance and Optical Tomography* (Oficyna Wydawnicza Politechniki Wrszawskiej, 2007).

[34] E. Rank, "Adaptive h-, p- and hp-versions for boundary integral element methods," International Journal for Numerical Methods in Engineering **28**, 1335–1349 (1989).

[35] J. Sikora, S. R. Arridge, J. Ripoll, A. D. Zacharopoulos, and J. D. Riley, "Light Propagation in Diffusive Media With Non-Scattering Regions Using 3D BEM," in "Boundary Integral Methods: Theory and Applications (University of Reading 14-18 September)," (2004).

[36] O. C. Zienkiewicz, D. W. Kelly, and P. Bettess, "The coupling of the finite element method and boundary solution procedures," International Journal for Numerical Methods in Engineering **11**, 355–375 (1977).

[37] S. R. Arridge, M. Schweiger, M. Hiraoka, and D. T. Delpy, "A finite element approach for modeling photon transport in tissue," Medical Physics **20**, 299–309 (1993).

[38] M. Schweiger and S. R. Arridge, "Optical tomographic reconstruction in a complex head model using a priori region boundary information," Physics in Medicine and Biology **44**, 2703–2721 (1999).

[39] B. W. Pogue and K. D. Paulsen, "High-resolution near-infrared tomographic imaging simulations of the rat cranium by use of a priori magnetic resonance imaging structural information," Optics Letters **23**, 1716–1718 (1998).

[40] J. C. Hebden, A. Gibson, R. M. Yusof, N. Everdell, E. M. C. Hillman, D. T. Delpy, S. R. Arridge, T. Austin, J. H. Meek, and J. S. Wyatt, "Three-dimensional optical tomography of the premature infant brain," Physics in Medicine and Biology **47**, 4155–4166 (2002).

[41] N. Guyot, F. Kosior, and G. Maurice, "Coupling of finite elements and boundary elements methods for study of the frictional contact problem," Computer Methods in Applied Mechanics and Engineering **181**, 147–159 (2000).

[42] C. A. Brebbia and P. Georgiou, "Combination of boundary and finite elements in elastostatics," Applied Mathematical Modelling **3**, 212–220 (1979).

[43] U. Brink, C. Carstensen, and E. Stein, "Symmetric coupling of boundary elements and raviart-thomas-type mixed finite elements in elastostatics," Numerische Mathematik **75**, 153–174 (1996).

[44] B. Kortschak and B. Brandstaetter, "A FEM-BEM approach using level-sets in electrical capacitance tomography," COMPEL: The International Journal for Computation and Mathematics in Electrical and Electronic Engineering **24**, 591–605 (2005).

[45] L. Fox and E. T. Goodwin, "Some new methods for the numerical integration of ordinary differential equations," Mathematical Proceedings of the Cambridge Philosophical Society **45**, 373–388 (1949).

[46] G. D. Smith, *Numerical Solution of Partial Differential Equations: Finite Difference Methods* (Oxford University Press, 1985).

[47] R. W. Clough, "Early history of the finite element method from the view point of a pioneer," International Journal for Numerical Methods in Engineering **60**, 283–287 (2004).

[48] M. J. Turner, R. W. Clough, H. C. Martin, and L. Topp, "Stiffness and deflection analysis of complex structures," Journal of Aeronautical Sciences **23** (1956).

[49] O. C. Zienkiewicz, R. L. Taylor, and J. Z. Zhu, *The Finite Element Method: Its Basis and Fundamentals* (Butterworth Heinemann, 2005 (6th edition)).

[50] M. Schweiger and S. R. Arridge, "The finite element method for the propagation of light in scattering media: Frequency domain case," Medical Physics **24**, 895–902 (1997).

[51] S. Srinivasan, B. W. Pogue, S. Jiang, H. Dehgahni, and K. D. Paulsen, "Spectrally constrained chromophore and scattering near-infrared tomography provides quantitative and robust reconstruction," Applied Optics **44**, 1858–1869 (2005).

[52] Y. Xu, N. Iftimia, and H. Jiang, "Three-dimensional diffuse optical tomography of bones and joints," Journal of Biomedical Optics **7**, 88–92 (2002).

[53] A. Y. Bluestone, G. Abdoulaev, C. H. Schmitz, R. L. Barbour, and A. H. Hielscher, "Three-dimensional optical tomography of hemodynamics in the human head," Optics Express **9**, 272–286 (2001).

[54] C. M. Carpenter, S. Srinivasan, B. W. Pogue, and K. D. Paulsen, "Methodology Development for Three-Dimensional MR-Guided Near Infrared Spectroscopy of Breast Tumors," Optics Express **16**, 17903–17914 (2008).

[55] T. E. Inder and J. J. Volpe, "Mechanisms of perinatal brain injury," Seminars in Neonatology **5**, 3–16 (2000).

[56] J. S. Wyatt, "Noninvasive assessment of cerebral oxidative metabolism in the human newborn," Journal of the Royal College of Physicians London **28**, 126–132 (1994).

[57] E. Kirimi, O. Tuncer, B. Atas, M. E. Sakarya, and A. Ceylan, "Clinical value of color doppler ultrasonography measurements of full-term newborns with perinatal asphyxia and hypoxic ischemic encephalopathy in the first 12 hours of life and long-term prognosis," The Tohoku Journal of Experimental Medicine **197**, 27–33 (2002).

[58] D. M. Ferriero, "Neonatal Brain Injury," The New England Journal of Medicine **351**, 1985–1995 (2004).

[59] J. Heiskala, P. Hiltunen, and I. Nissila, "Significance of background optical propertis, time-resolved information and optode arrangement in diffuse optical imaging of term neonates," Physics in Medicine and Biology **54**, 535–554 (2009).

[60] H. Dehghani, B. R. White, B. W. Zeff, A. Tizzard, and J. P. Culver, "Depth sensitivity and image reconstruction analysis of dense imaging arrays for mapping brain function with diffuse optical tomography," Applied Optics **48**, D137–D143 (2009).

[61] Y. Fukui, Y. Ajichi, and E. Okada, "Monte carlo prediction of near-infrared light propagation in realistic adult and neonatal head models," Applied Optics **42**, 2881–2887 (2003).

[62] A. Liebert, H. Wabnitz, J. Steinbrink, H. Obrig, M. Möller, R. Macdonald, A. Villringer, and H. Rinneberg, "Time-resolved multidistance near-infrared spectroscopy of the adult head: Intracerebral and extracerebral absorption changes from moments of distribution of times of flight of photons," Applied Optics **43**, 3037–3047 (2004).

[63] T. S. Leung, C. E. Elwell, and D. T. Delpy, "Estimation of cerebral oxy- and deoxyhaemoglobin concentration changes in a layered adult head model using near-infrared spectroscopy and multivariate statistical analysis," Physics in Medicine and Biology **50**, 5783–5798 (2005).

[64] F. Abdelnour, B. Schmidt, and T. J. Huppert, "Topographic localization of brain activation in diffuse optical imaging using spherical wavelets," Physics in Medicine and Biology **54**, 6383 (2009).

[65] H. Dehghani, B. W. Pogue, J. Shudong, B. Brooksby, and K. D. Paulsen, "Three-dimensional optical tomography: Resolution in small-object imaging," Applied Optics **42**, 3117–3128 (2003).

[66] S. Allaire, F. Wolfe, J. Niu, M. Lavalley, and K. Michaud, "Work disability and its economic effect on 55-64-year-old adults with rheumatoid arthritis," Arthritis and Rheumatism **53**, 603–608 (2005).

[67] J. Beuthan, V. Prapavat, R. Naber, O. Minet, and G. Muller, "Diagnostic of inflammatory rheumatic diseases with photon density waves," Proceedings of the SPIE **2676**, 43–53 (1996).

[68] V. Prapavat, W. Runge, J. Mans, A. Krause, J. Beuthan, and G. Muller, "The development of a finger joint phantom for the optical simulation of early inflammatory rheumatic changes," Biomedizinische Technik **42**, 319–326 (1997).

[69] E. M. Hillman, J. C. Hebden, M. Schweiger, H. Dehgahni, F. E. W. Schmidt, D. T. Delpy, and S. R. Arridge, "Time-resolved optical tomography of the human forearm," Physics in Medicine and Biology **46**, 1117–1130 (2001).

[70] M. Cutler, "Transillumination of the breast," Surgical Gynecology, Obstetrics **48**, 721–727 (1929).

[71] M. J. Holbroke, B. Tromberg, X. Li, N. Shah, J. Fishkin, D. Kidney, J. Butler, B. Chance, and A. Yodh, "Three-dimensional diffuse optical mammography with ultrasound localization in a human subject," Journal of Biomedical Optics **5**, 237–247 (2000).

[72] H. Jiang, Y. Xu, N. Iftimia, J. Eggert, K. Klove, L. Baron, and L. Fajardo, "Three-dimensional optical tomographic imaging of breast in a human subject," IEEE Transactions on Medical Imaging **20**, 1334–1340 (2001).

[73] S. R. Arridge and W. R. B. Lionheart, "Nonuniqueness in diffusion-based optical tomography," Optics Letters **23**, 882–884 (1998).

[74] D. R. Leff, O. J. Warren, L. C. Enfield, A. Gibson, T. Athanasiou, D. K. Patten, J. Hebden, G. Z. Yang, and A. Darzi, "Diffuse optical imaging of the healthy and diseased breast: A systematic review," Breast Cancer Research and Treatment **108**, 9–22 (2008).

[75] B. Brooksby, B. W. Pogue, S. Jiang, H. Dehgahni, S. Srinivasan, C. Kogel, T. D. Tosteson, J. Weaver, S. P. Poplack, and K. D. Paulsen, "Imaging Breast Adipose and Fibroglan-

dular Tissue Molecular Signatures by Using Hybrid MRI-guided Near-Infrared Spectral Tomography," Proceedings of the National Academy of Sciences of the United States of America **103**, 8826–8833 (2006).

[76] A. Sharma, L. Enfield, A. Gibson, N. Everdell, M. Schweiger, S. Arridge, D. Delpy, J. Hebden, M. Keshtgar, and R. Sainsbury, "The sensitivity and specificity of optical tomography for the detection of breast cancer," European Journal of Surgical Oncology **33**, 1134–1135 (2007).

[77] M. A. Bedell, N. A. Jenkins, and N. G. Copeland, "Mouse models of human disease. part i: Techniques and recsources for genetic analysis in mice," Genes and Development **11**, 1–10 (1997).

[78] S. K. Lyons, "Advances in imaging mouse tumour models in vivo," The Journal of Pathology **205**, 194–205 (2005).

[79] K. Shah and R. Weissleder, "Molecular optical imaging: Applications leading to the development of present day therapeutics," NeuroRX **2**, 215–225 (2005).

[80] A. K. Klose, V. Ntziachristos, and A. H. Hielscher, "The inverse source problem based on the radiative transfer equation in molecular optical imaging," Journal of Computational Physics **202**, 323–345 (2005).

[81] A. H. Hielscher, A. Y. Bluestone, G. S. Abdoulaev, A. D. Klose, J. Lasker, M. Stewart, U. Netz, and J. Beuthan, "Near-infrared diffuse optical tomography," Disease Markers **18**, 313–337 (2002).

[82] U. Mahmood, C. Tung, Y. Tang, and R. Weissleder, "Feasibility of in vivo multichannel optical imaging of gene expression: Experimental study in mice," Radiology **224**, 446–451 (2002).

[83] X. Cheng and B. A. Boas, "Systematic diffuse optical image errors resulting from uncertainty in the background optical properties," Optics Express **4**, 299–307 (1999).

[84] J. Masciotti, G. Abdoulaev, F. Provenzano, J. Hur, J. Papa, J. Bae, J. Huang, D. Yamashiro, J. Kandel, and A. H. Hielscher, "Optical tomographic and magnetic resonance imaging of tumor growth and regression in mice treated with vegf blockade," Proceedings of the 2005 IEEE pp. 205–208 (2005).

[85] A. Da Silva, J. Dinten, J. Coll, and P. Rizo, "From bench-top small animal diffuse optical tomography towards clinical imaging," Proceedings of the 29th Annual International Conference of the IEEE EMBS pp. 526–529 (2007).

[86] N. Deliolanis, T. Lasser, D. Hyde, A. Soubret, J. Ripoll, and V. Ntziachristos, "Free-Space Fluorescence Molecular Tomography Utilizing 360 degrees Geometry Projections," Optics Letters **32**, 382–384 (2007).

[87] R. Weissleder and V. Ntziachristos, "Shedding light onto live molecular targets," Nature Medicine **9**, 123–128 (2003).

[88] Y. Zilberman, I. Kallai, Y. Gafni, G. Pelled, S. Kossodo, W. Yared, and D. Gazit, "Fluorescence molecular tomography enables in vivo vsualization and quantification of nonunion fracture repair induced by genetically engineered mesenchymal stem cells," Journal of Orthopaedic Research **26**, 522–530 (2008).

[89] W. Cong, G. Wang, D. Kumar, Y. Liu, M. Jiang, L. V. Wang, E. A. Hoffman, G. McLennan, P. B. McCray, J. Zabner, and A. Cong, "Practical reconstruction technique for bioluminescence tomography," Optics Express **13**, 6756–6771 (2005).

[90] E. A. Forssen, R. Male-Brune, J. P. Adler-Moore, M. J. A. Lee, P. G. Schmidt, T. B. Krasieva, S. Shimizu, and B. J. Tromberg, "Fluorescence imaging studies for the disposition of daunorubicin liposomes (daunoxome) within tumor tissue," Cancer Research **56**, 2066–2075 (1996).

[91] R. Weissleder and M. J. Pittet, "Imaging in the era of molecular oncology," Nature **452**, 580–589 (2008).

[92] S. R. Cherry, "In vivo molecular and genomic imaging: New challenges for imaging physics," Physics in Medicine and Biology **49**, R13–R48 (2004).

[93] P. R. Contag, "Whole-animal cellular and molecular imaging to accelerate drug development," Drug Discovery Today **7**, 555–562 (2002).

[94] A. H. Hielscher, "Optical tomographic imaging of small animals," Current Opinion in Biotechnology **16**, 79–88 (2005).

[95] M. Firbank, S. R. Arridge, M. Schweiger, and D. Delpy, "An Investigation of Light Transport Through Scattering Bodies with Non-Scattering Regions," Physics in Medicine and Biology **41**, 767–783 (1996).

[96] S. R. Arridge, H. Dehgahni, M. Schweiger, and E. Okada, "The Finite Element Model for the Propagation of Light in Scattering Media: A Direct Method for Domains with Non-Scattering Regions," Medical Physics **27**, 252–264 (2000).

[97] H. Dehghani, S. R. Arridge, M. Schweiger, and D. Delpy, "Optical tomography in the presence of void regions," Journal of the Optical Society of America A **17**, 1659–1670 (2000).

[98] A. P. Gibson, T. Austin, N. L. Everdell, M. Schweiger, S. R. Arridge, J. H. Meek, J. S. Wyatt, D. T. Delpy, and J. C. Hebden, "Three-dimensional whole-head optical tomography of passive motor evoked responses in the neonate," Neuroimage **30**, 521–528 (2006).

[99] E. Okada and D. T. Delpy, "Near-Infrared Light Propagation in an Adult Head Model. I. Modeling of Low-Level Scattering in the Cerebrospinal Fluid Layer," Applied Optics **42**, 2906–2914 (2003).

[100] J. Riley, H. Dehgahni, M. Schweiger, S. R. Arridge, J. Ripoll, and M. Nieto-Vesperinas, "3D Optical Tomography in the Presence of Void Regions," Optics Express **7**, 462–467 (2000).

[101] A. Y. Bluestone, M. Stewart, J. Lasker, G. S. Abdoulaev, and A. H. Hielscher, "Three-dimensional optical tomographic brain imaging in small animals, part 1: hypercapnia," Journal of Biomedical Optics **9**, 1046–1062 (2004).

[102] I. Babuska and A. K. Aziz, "On the angle condition in the finite element method," SIAM Journal on Numerical Analysis **13**, 214–226 (1976).

[103] J. R. Shewchuk, "What is a good linear finite element? interpolation, conditioning, anisotropy, and quality measures," (2002).

[104] I. Harari and T. J. R. Hughes, "A cost comparison of boundary element and finite element methods for problems of time-harmonic acoustics," Computer Methods in Applied Mechanics and Engineering **97**, 77–102 (1992).

[105] M. A. Jaswon, "Integral Equation Methods in Potential Theory. I," Proceedings of the Royal Society of London. Series A, Mathematical and Physical Sciences **275**, 23–32 (1963).

[106] G. T. Symm, "Integral Equation Methods in Potential Theory. II," Proceedings of the Royal Society of London. Series A, Mathematical and Physical Sciences **275**, 33–46 (1963).

[107] C. A. Brebbia and J. Dominguez, "Boundary element methods for potential problems," Applied Mathematical Modelling **1**, 372–378 (1977).

[108] J. Ripoll and M. Nieto-Vesperinas, "Scattering integral equations for diffusive waves: Detection of objects buried in diffusive media in the presence of rough interfaces," Journal of the Optical Society of America A **16**, 1453–1465 (1999).

[109] J. Ripoll, "Light diffusion in turbid media with biomedical application," Ph.D. thesis, Universidad Autonoma de Madrid (2000).

[110] J. Ripoll and V. Ntziachristos, "Iterative boundary method for diffuse optical tomography," Journal of the Optical Society of America A **20**, 1103–1110 (2003).

[111] M. Boffety, J. Elisee, M. Allain, A. Sentenac, B. Zhang, M. Massonneau, and R. Carminati, "Molecular Imaging on Small Animals Using Reflection-Mode Fluorescent Diffuse Optical Tomography," Poster in the 6th International Conference on Photonics and Imaging in Biology and Medicine (PIBM 2007) (2007). Wuhan, China.

[112] W. Cong and G. Wang, "Boundary integral method for bioluminescence tomography," Journal of Biomedical Optics Letters **11**, 020503–1–3 (2006).

[113] A. A. Becker, *The Boundary Element Method in Engineering. A Complete Course* (McGraw-Hill Book Company, 1992).

[114] D. A. S. Curran, M. Cross, and B. A. Lewis, "Solution of parabolic differential equations by the boundary element method using discretisation in time," Applied Mathematical Modelling **4**, 398–400 (1980).

[115] G. C. Everstine and F. M. Henderson, "Coupled Finite Element/Boundary Element Approach for Fluid Structure Interaction," Journal of the Acoustical Society of America **87**, 1938–1947 (1990).

[116] L. Gaul and M. Fischer, "Fast BEM-FEM mortar coupling for Acoustic-Structure Interaction," International Journal for Numerical Methods in Engineering **62**, 1677–1690 (2005).

[117] J.-M. Jin, J. L. Volakis, and J. D. Collins, "A Finite-Element–Boundary-Integral Method for Scattering and Radiation by Two- and Three-Dimensional Structures," IEEE Antennas and Propagation Magazine **33**, 22–32 (1991).

[118] A. Frangi and G. Novatti, "BEM-FEM Coupling for 3D Fracture Mechanics Applications," Computational Mechanics **32**, 415–422 (2003).

[119] K. L. Leung, P. B. Zavareh, and D. E. Beskos, "2-D Elastostatic Analysis by a Symmetric BEM/FEM Scheme," Engineering Analysis with Boundary Elements **15**, 67–78 (1995).

[120] J. O'Brien and D. C. Rizos, "A 3D BEM-FEM Methodology for Simulation of High-Speed Train Induced Vibrations," Soil Dynamics and Earthquake Engineering **25**, 289–301 (2005).

[121] J. R. Soares, O. von Estorff, and W. J. Mansur, "Iterative Coupling of BEM and FEM for Nonlinear Dynamic Analyses," Computational Mechanics **34**, 67–73 (2004).

[122] G. Swoboda, W. Mertz, and G. Beer, "Rheological Analysis of Tunnel Excavations by Means of Coupled Finite Element (FEM)-Boundary Element (BEM) Analysis," International Journal for Numerical and Analytical Methods in Geomechanics **11**, 115–129 (1985).

[123] W. M. Elleithy and H. J. Al-Gahtani, "An overlapping domain decomposition approach for coupling the finite and boundary element methods," Engineering Analysis with Boundary Elements **24**, 391–398 (2000).

[124] F. Jobsis, "Noninvasive, infrared monitoring of cerebral and myocardial oxygen sufficiency and circulatory parameters," Science **198**, 1264–1267 (1977).

[125] Y. Hoshi, "Functional Near Infrared Spectroscopy: Potential and Limitations in Neuroimaging Studies," in "Neuroimaging, Part A," , vol. 66 of *International Review of Neurobiology*, M. F. Glabus, ed. (Academic Press, 2005), pp. 237 – 266.

[126] D. T. Delpy, M. Cope, P. van der Zee, S. R. Arridge, S. Wray, and J. Wyatt, "Estimation of optical pathlength through tissue from direct time of flight measurement," Physics in Medicine and Biology **33**, 1433 (1988).

[127] H. Zhao, Y. Tanikawa, F. Gao, Y. Onodera, A. Sassaroli, K. Tanaka, and Y. Yamada, "Maps of optical differential pathlength factor of human adult forehead, somatosensory

motor and occipital regions at multi-wavelengths in nir," Physics in Medicine and Biology **47**, 2075 (2002).

[128] Y. Hoshi, "Functional near-infrared spectroscopy: current status and future prospects," Journal of Biomedical Optics **12**, 062106 (2007).

[129] N. L. Everdell, A. P. Gibson, I. D. C. Tullis, T. Vaithianathan, J. C. Hebden, and D. T. Delpy, "A frequency multiplexed near-infrared topography system for imaging functional activation in the brain," Review of Scientific Instruments **76**, 093705 (2005).

[130] T. J. Germon, P. D. Evans, N. J. Barnett, P. Wall, A. R. Manara, and R. J. Nelson, "Cerebral near infrared spectroscopy: emitter-detector separation must be increased," Br. J. Anaesth. **82**, 831–837 (1999).

[131] P. W. McCormick, M. Stewart, M. G. Goetting, M. Dujovny, G. Lewis, and J. I. Ausman, "Noninvasive cerebral optical spectroscopy for monitoring cerebral oxygen delivery and hemodynamics," Critical Care Medicine **19** (1991).

[132] F. Fabbri, A. Sassaroli, M. E. Henry, and S. Fantini, "Optical measurements of absorption changes in two-layered diffusive media," Physics in Medicine and Biology **49**, 1183–1201 (2004).

[133] T. S. Leung, I. Tachtsidis, M. Smith, D. T. Delpy, and C. E. Elwell, "Measurement of the absolute optical properties and cerebral blood volume of the adult human head with hybrid differential and spatially resolved spectroscopy," Physics in Medicine and Biology **51**, 703 (2006).

[134] S. J. Matcher, P. J. Kirkpatrick, K. Nahid, M. Cope, and D. T. Delpy, "Absolute quantification methods in tissue near-infrared spectroscopy," Optical Tomography, Photon Migration, and Spectroscopy of Tissue and Model Media: Theory, Human Studies, and Instrumentation **2389**, 486–495 (1995).

[135] S. Suzuki, S. Takasaki, T. Ozaki, and Y. Kobayashi, "Tissue oxygenation monitor using NIR spatially resolved spectroscopy," in "Proceedings of the SPIE," , vol. 3597, B. Chance, R. R. Alfano, and B. J. Tromberg, eds. (SPIE, 1999), vol. 3597, pp. 582–592.

[136] T. Correia, A. Banga, N. L. Everdell, A. P. Gibson, and J. C. Hebden, "A quantitative assessment of the depth sensitivity of an optical topography system using a solid dynamic tissue-phantom," Physics in Medicine and Biology **54**, 6277 (2009).

[137] R. J. Hunter, M. S. Patterson, T. J. Farrell, and J. E. Hayward, "Haemoglobin oxygenation of a two-layer tissue-simulating phantom from time-resolved reflectance: effect of top layer thickness," Physics in Medicine and Biology **193**, 193–208 (2002).

[138] E. Okada and D. T. Delpy, "Near-infrared Light Propagation in an Adult Head Model. II. Effect of Superficial Tissue Thickness on the Sensitivity of the Near-infrared Spectroscopy Signal," Applied Optics **52**, 2915–2921 (2003).

[139] J. Steinbrink, "Near-infrared-spectroscopy on the adult human head with picosecond resolution," Ph.D. thesis, Fachbereich Physik, Freie Universitaet Berlin (2000).

[140] D. Boas, J. Culver, J. Stott, and A. Dunn, "Three dimensional monte carlo code for photon migration through complex heterogeneous media including the adult human head," Optics Express **10**, 159–170 (2002).

[141] M. Hiraoka, M. Firbank, M. Essenpreis, M. Cope, S. R. Arridge, P. van der Zee, and D. T. Delpy, "A Monte Carlo investigation of optical pathlength in inhomogeneous tissue and its application to near-infrared spectroscopy," Physics in Medicine and Biology **38**, 1859 (1993).

[142] M. Takeuchi, E. Hori, K. Takamoto, A. H. Tran, K. Satoru, A. Ishikawa, T. Ono, S. Endo, and H. Nishijo, "Brain Cortical Mapping by Simultaneous Recording of Functional Near Infrared Spectroscopy and Electroencephalograms from the Whole Brain During Right Median Nerve Stimulation," Brain Topography **22**, 197–214 (2009).

[143] M. J. Hofmann, M. J. Herrman, I. Dan, H. Obrig, M. Conrad, L. Kuchinke, A. M. Jacobs, and A. J. Fallgatter, "Differential Activation of Frontal and Parietal Regions during Visual Word Recognition: An Optical Topography Study," Neuroimage **40**, 1340–1349 (2008).

[144] T. Nakahachi, M. Iwase, L. Canuet, H. Takahashi, R. Kurimoto, K. Ikezawa, M. Azechi, R. Sekiyama, E. Honaga, C. Uchiumi, M. Iwakiri, N. Motomura, and M. Takeda, "Frontal Activity during the Digit Symbol Substitution Test Determined by Multichannel Near-Infrared Spectroscopy," Neuropsychobiology **57**, 151–158 (2008).

[145] M. H. Shalinsky, I. Kovelman, M. S. Berens, and L. A. Petitto, "Exploring Cognitive Functions in Babies, Children and Adults with Near Infrared Spectroscopy," Journal of Visualized Experiments (2009).

[146] H. H. Jasper, "Report of the committee on methods of clinical examination in electroencephalography," Electroencephalography and Clinical Neurophysiology **10**, 370–371 (1958).

[147] M. Okamoto, H. Dan, K. Sakamoto, K. Takeo, K. Shimizu, S. Kohno, I. Oda, S. Isobe, T. Suzuki, K. Kohyama, and I. Dan, "Three-dimensional probabilistic anatomical cranio-cerebral correlation via the international 10-20 system oriented for transcranial functional brain mapping," NeuroImage **21**, 99 – 111 (2004).

[148] V. L. Towle, J. Bolanos, D. Suarez, K. Tan, R. Grzeszczuk, D. N. Levin, R. Cakmur, S. A. Frank, and J.-P. Spire, "The spatial location of eeg electrodes: locating the best-fitting sphere relative to cortical anatomy," Electroencephalography and Clinical Neurophysiology **86**, 1 – 6 (1993).

[149] A. K. Singh, M. Okamoto, H. Dan, V. Jurcak, and I. Dan, "Spatial registration of multichannel multi-subject fNIRS data to MNI space without MRI," NeuroImage **27**, 842 – 851 (2005).

[150] D. Tsuzuki, V. Jurcak, A. K. Singh, M. Okamoto, E. Watanabe, and I. Dan, "Virtual spatial registration of stand-alone fNIRS data to MNI space," NeuroImage **34**, 1506 – 1518 (2007).

[151] D. A. Boas, K. Chen, D. Grebert, and M. A. Franceschini, "Improving the diffuse optical imaging spatial resolutionof the cerebral hemodynamic response to brain activation in humans," Optics Letters **29**, 1506–1508 (2004).

[152] M. L. Schroeter, M. M. Bucheler, K. Mueller, K. Uludag, H. Obrig, G. Lohmann, M. Tittgemeyer, A. Villringer, and D. Y. von Cramon, "Towards a standard analysis for functional near-infrared imaging," Neuroimage **21**, 283–290 (2004).

[153] M. Plichta, S. Heinzel, A.-C. Ehlis, P. Pauli, and A. Fallgatter, "Model-based analysis of rapid event-related functional near-infrared spectroscopy (NIRS) data: A parametric validation study," NeuroImage **35**, 625 – 634 (2007).

[154] K. J. Worsley and K. J. Friston, "Analysis of fMRI Time-Series Revisited–Again," NeuroImage **2**, 173 – 181 (1995).

[155] P. H. Koh, D. E. Glaser, G. Flandin, S. Kiebel, B. Butterworth, A. Maki, D. T. Delpy, and C. E. Elwell, "Functional optical signal analysis: a software tool for near-infrared

spectroscopy data processing incorporating statistical parametric mapping," Journal of Biomedical Optics **12**, 064010 (2007).

[156] J. C. Ye, S. Tak, K. E. Jang, J. Jung, and J. Jang, "NIRS-SPM: Statistical parametric mapping for near-infrared spectroscopy," NeuroImage **44**, 428 – 447 (2009).

[157] K. E. Jang, S. Tak, J. Jang, J. Jung, and J. C. Ye, "Wavelet-MDL based detrending method for near infrared spectroscopy (NIRS)," Multimodal Biomedical Imaging III **6850**, 68500Y (2008).

[158] D. Contini, A. Torricelli, A. Pifferi, L. Spinelli, F. Paglia, and R. Cubeddu, "Multi-channel time-resolved system for functional near infrared spectroscopy," Optics Express **14**, 5418–5432 (2006).

[159] H. Eda, I. Oda, Y. Ito, Y. Wada, Y. Oikawa, Y. Tsunazawa, M. Takada, Y. Tsuchiya, Y. Yamashita, M. Oda, A. Sassaroli, Y. Yamada, and M. Tamura, "Multichannel time-resolved optical tomographic imaging system," Review of Scientific Instruments **70**, 3595–3602 (1999).

[160] M. Kacprzak, A. Liebert, P. Sawosz, N. Zolek, and R. Maniewski, "Time-resolved optical imager for assessment of cerebral oxygenation," Journal of Biomedical Optics **12**, 034019 (2007).

[161] F. E. W. Schmidt, M. E. Fry, E. M. C. Hillman, J. C. Hebden, and D. T. Delpy, "A 32-channel time-resolved instrument for medical optical tomography," Review of Scientific Instruments **71**, 256–265 (2000).

[162] J. Selb, J. J. Stott, M. A. Franceschini, A. G. Sorensen, and D. A. Boas, "Improved sensitivity to cerebral hemodynamics during brain activation with a time-gated optical system: analytical model and experimental validation," Journal of Biomedical Optics **10**, 011013 (2005).

[163] H. Wabnitz, M. Moeller, A. Liebert, A. Walter, R. Macdonald, H. Obrig, J. Steinbrink, R. Erdmann, and O. Raitza, "A time-domain nir brain imager applied in functional stimulation experiments," in "Photon Migration and Diffuse-Light Imaging II," (Optical Society of America, 2005), p. WA5.

[164] A. Liebert, H. Wabnitz, J. Steinbrink, M. Möller, R. Macdonald, H. Rinneberg, A. Villringer, and H. Obrig, "Bed-side assessment of cerebral perfusion in stroke patients based

on optical monitoring of a dye bolus by time-resolved diffuse reflectance," NeuroImage **24**, 426 – 435 (2005).

[165] J. Steinbrink, H. Wabnitz, H. Obrig, A. Villringer, and H. Rinneberg, "Determining changes in nir absorption using a layered model of the human head," Physics in Medicine and Biology **46**, 879–896(18) (2001).

[166] H. Wabnitz, M. Moeller, A. Liebert, H. Obrig, J. Steinbrink, and R. Macdonald, *Oxygen Transport to Tissue XXXI* (Springer US, 2010), vol. 662 of *Biomedical and Life Sciences*, chap. Time-Resolved Near-Infrared Spectroscopy and Imaging of the Adult Human Brain, pp. 143–148.

[167] M. Kohl-Bareis, H. Obrig, J. Steinbrink, J. Malak, K. Uludag, and A. Villringer, "Noninvasive monitoring of cerebral blood flow by a dye bolus method: Separation of brain from skin and skull signals," Journal of Biomedical Optics **7**, 464–470 (2002).

[168] A. Blasi, S. Fox, N. Everdell, A. Volein, L. Tucker, G. Csibra, A. P. Gibson, J. C. Hebden, M. H. Johnson, and C. E. Elwell, "Investigation of depth dependent changes in cerebral haemodynamics during face perception in infants," Physics in Medicine and Biology **52**, 6849 (2007).

[169] S. R. Arridge, M. Cope, and D. T. Delpy, "The theoretical basis for the determination of optical pathlengths in tissue: temporal and frequency analysis," Physics in Medicine and Biology **37**, 1531 (1992).

[170] F. Abdelnour and T. Huppert, "A random-effects model for group-level analysis of diffuse optical brain imaging," Biomedical Optics Express **2**, 1–25 (2011).

[171] B. Fischl, M. I. Sereno, and A. M. Dale, "Cortical Surface-Based Analysis: II: Inflation, Flattening, and a Surface-Based Coordinate System," NeuroImage **9**, 195 – 207 (1999).

[172] Y. Tong and B. Frederick, "Using fMRI analysis tools (FSL/FreeSurfer) to analyze near-infrared imaging of the brain," NeuroImage **47**, S58 (2009). Organization for Human Brain Mapping 2009 Annual Meeting.

[173] A. Custo, D. A. Boas, D. Tsuzuki, I. Dan, R. Mesquita, B. Fischl, W. E. L. Grimson, and W. W. III, "Anatomical atlas-guided diffuse optical tomography of brain activation," NeuroImage **49**, 561 – 567 (2010).

[174] M. Caffini, A. Torricelli, R. Cubeddu, A. Custo, J. Dubb, and D. A. Boas, "Validating an Anatomical Brain Atlas for Analyzing NIRS Measurements of Brain Activation," in "Digital Holography and Three-Dimensional Imaging," (Optical Society of America, 2010), p. JMA87.

[175] R. P. Kennan, D. Kim, A. Maki, H. Koizumi, and R. T. Constable, "Non-Invasive Assessment of Language Lateralization by Transcranial Near Infrared Optical Topography and Functional MRI," Human Brain Mapping **16**, 183–189 (2002).

[176] H. Koizumi, T. Yamamoto, A. Maki, Y. Yamashita, H. Sato, H. Kawaguchi, and N. Ichikawa, "Optical Topography: Practical Problems and New Applications," Applied Optics **42**, 3054–3062 (2003).

[177] S. G. Horovitz and J. C. Gore, "Simultaneous event-related potential and near-infrared spectroscopic studies of semantic procesing," Human Brain Mapping **22**, 110–115 (2004).

[178] S. P. Koch, J. Steinbrink, A. Villringer, and H. Obrig, "Synchronization between Background Activity and Visually Evoked Potential Is Not Mirrored by Focal Hyperoxygenation: Implications for the Interpretation of Vascular Brain Imaging," The Journal of Neuroscience **26**, 4940–4948 (2006).

[179] B.-M. Mackert, G. Wuebbeler, S. Leistner, K. Uludag, H. Obrig, A. Villringer, L. Trahms, and G. Curio, "Neurovascular coupling analyzed non-invasively in the human brain," NeuroReport **15**, 63–66 (2004).

[180] H. Obrig, H. Israel, M. Kohl-Bareis, K. Uludag, R. Wenzel, B. Mueller, G. Arnold, and A. Villringer, "Habituation of the visually evoked potential and its vascular response: Implications for neurovascular coupling in the healthy adult," NeuroImage **17**, 1 – 18 (2002).

[181] M. M. Tisdall, I. Tachtsidis, T. S. Leung, C. E. Elwell, and M. Smith, "Near-infrared spectroscopic quantification of changes in the concentration of oxidized cytochrome c oxidase in the healthy human brain during hypoxemia," Journal of Biomedical Optics **12**, 024002 (2007).

[182] M. Smith and C. Elwell, "Near-Infrared Spectroscopy: Shedding Light on the Injured Brain," Anesthesia & Analgesia **108**, 1055–1057 (2009).

[183] Y. Hoshi, O. Hazeki, Y. Kakihana, and M. Tamura, "Redox behavior of cytochrome oxidase in the rat brain measured by near-infrared spectroscopy," Journal of Applied Physiology **83**, 1842–1848 (1997).

[184] M. A. Franceschini, S. Fantini, L. A. Paunescu, J. S. Maier, and E. Gratton, "Influence of a Superficial Layer in the Quantitative Spectroscopic Study of Strongly Scattering Media," Applied Optics **37**, 7447–7458 (1998).

[185] T. J. Farrell, M. S. Patterson, and M. Essenpreis, "Influence of layered tissue architecture on estimates of tissue optical properties obtained from spatially resolved diffuse reflectometry," Applied Optics **37**, 1958–1972 (1998).

[186] A. H. Hielscher, H. Liu, B. Chance, F. K. Tittel, and S. L. Jacques, "Time-resolved photon emission from layered turbid media," Applied Optics **35**, 719–728 (1996).

[187] H. Owen-Reece, M. Smith, C. E. Elwell, and J. C. Goldstone, "Near infrared spectroscopy," British Journal of Anaesthesia **82**, 418–426 (1999).

[188] P. G. Al-Rawi, P. Smielewski, and P. J. Kirkpatrick, "Evaluation of a Near-Infrared Spectrometer (NIRO 300) for the Detection of Intracranial Oxygenation Changes in the Adult Head," Stroke **32**, 2492–2500 (2001).

[189] S. Kohno, I. Miyai, A. Seiyama, I. Oda, A. Ishikawa, S. Tsuneishi, T. Amita, and K. Shimizu, "Removal of the skin blood flow artifact in functional near-infrared spectroscopic imaging data through independent component analysis," Journal of Biomedical Optics **12**, 062111 (2007).

[190] J. Dunn, Y. Zaim-Wadghiri, B. Pogue, and I. Kida, "Bold MRI vs. NIR spectrophotometry - Will the best technique come forward?" in "OXYGEN TRANSPORT TO TISSUE XX," , vol. 454 of *ADVANCES IN EXPERIMENTAL MEDICINE AND BIOLOGY* (1998), vol. 454 of *ADVANCES IN EXPERIMENTAL MEDICINE AND BIOLOGY*, pp. 103–113. 25th Annual Meeting of the International-Society-on-Oxygen-Transport-to-Tissue (ISOTT), MILWAUKEE, WISCONSIN, AUG 19-23, 1997.

[191] T. Huppert, R. Hoge, S. Diamond, M. Franceschini, and D. Boas, "A temporal comparison of BOLD, ASL, and NIRS hemodynamic responses to motor stimuli in adult humans," NeuroImage **29**, 368 – 382 (2006).

[192] G. Strangman, J. P. Culver, J. H. Thompson, and D. A. Boas, "A Quantitative Comparison of Simultaneous BOLD fMRI and NIRS Recordings during Functional Brain Activation," NeuroImage **17**, 719 – 731 (2002).

[193] Y. Hoshi, M. Shimada, C. Sato, and Y. Iguchi, "Reevaluation of near-infrared light propagation in the adult human head: implications for functional near-infrared spectroscopy," Journal of Biomedical Optics **10**, 064032 (2005).

[194] M. S. Patterson, B. Chance, and B. C. Wilson, "Time resolved reflectance and transmittance for the non-invasive measurement of tissue optical properties," Applied Optics **28**, 2331–2336 (1989).

[195] A. Kienle, M. S. Patterson, N. Dögnitz, R. Bays, G. Wagnieres, and H. van den Bergh, "Noninvasive Determination of the Optical Properties of Two-Layered Turbid Media," Applied Optics **37**, 779–791 (1998).

[196] D. A. Boas, T. Gaudette, G. Strangman, X. Cheng, J. J. Marota, and J. B. Mandeville, "The accuracy of near infrared spectroscopy and imaging during focal changes in cerebral hemodynamics," NeuroImage **13**, 76 – 90 (2001).

[197] I. Miyai, H. C. Tanabe, I. Sase, H. Eda, I. Oda, I. Konishi, Y. Tsunazawa, T. Suzuki, T. Yanagida, and K. Kubota, "Cortical Mapping of Gait in Humans: A Near-Infrared Spectroscopic Topography Study," NeuroImage **14**, 1186 – 1192 (2001).

[198] C. Hock, K. Villringer, F. Mueller-Spahn, R. Wenzel, H. Heekeren, S. Schuh-Hofer, M. Hofmann, S. Minoshima, M. Schwaiger, U. Dirnagl, and A. Villringer, "Decrease in parietal cerebral hemoglobin oxygenation during performance of a verbal fluency task in patients with Alzheimer's disease monitored by means of near-infrared spectroscopy (NIRS) – correlation with simultaneous rCBF-PET measurements," Brain Research **755**, 293 – 303 (1997).

[199] Y. Hoshi, H. Onoe, Y. Watanabe, J. Andersson, M. Bergstroem, A. Lilja, B. Langstom, and M. Tamura, "Non-synchronous behavior of neuronal activity, oxidative metabolism and blood supply during mental tasks in man," Neuroscience Letters **172**, 129 – 133 (1994).

[200] E. Rostrup, I. Law, F. Pott, K. Ide, and G. M. Knudsen, "Cerebral hemodynamics measured with simultaneous PET and near-infrared spectroscopy in humans," Brain Research **954**, 183 – 193 (2002).

[201] A. Kleinschmidt, H. Obrig, M. Requardt, K.-D. Merboldt, U. Dirnagl, A. Villringer, and J. Frahm, "Simultaneous Recording of Cerebral Blood Oxygenation Changes During Human Brain Activation by Magnetic Resonance Imaging and Near-Infrared Spectroscopy," Journal of Cerebral Blood Flow and Metabolism **16**, 817–826 (1996).

[202] V. Toronov, A. Webb, J. H. Choi, M. Wolf, L. Safonova, U. Wolf, and E. Gratton, "Study of local cerebral hemodynamics by frequency-domain near-infrared spectroscopy and correlation with simultaneously acquired functional magnetic resonance imaging," Optics Express **9**, 417–427 (2001).

[203] T. Shinba, M. Nagano, N. Kariya, K. Ogawa, T. Shinozaki, S. Shimosato, and Y. Hoshi, "Near-infrared spectroscopy analysis of frontal lobe dysfunction in schizophrenia," Biological Psychiatry **55**, 154 – 164 (2004).

[204] T. Suto, M. Fukuda, M. Ito, T. Uehara, and M. Mikuni, "Multichannel near-infrared spectroscopy in depression and schizophrenia: cognitive brain activation study," Biological Psychiatry **55**, 501 – 511 (2004).

[205] A. A. Baird, J. Kagan, T. Gaudette, K. A. Walz, N. Hershlag, and D. A. Boas, "Frontal Lobe Activation during Object Permanence: Data from Near-Infrared Spectroscopy," NeuroImage **16**, 1120 – 1126 (2002).

[206] Y. Hoshi and S.-J. Chen, "Regional cerebral blood flow changes associated with emotions in children," Pediatric Neurology **27**, 275 – 281 (2002).

[207] H. Koizumi, A. Maki, and T. Yamamoto, "Optical topography: Practical problems and novel applications," in "Biomedical Topical Meeting," (Optical Society of America, 2002), p. MC1.

[208] M. Pena, A. Maki, D. Kovacic, G. Deheane-Lambertz, H. Koizumi, F. Bouquet, and J. Mehler, "Sounds and Silence: An Optical Topography study of Language Recognition at Birth," Proceedings of the National Society of America **100**, 11702–11705 (2003).

[209] K. Liu, D. S. Borrett, A. Cheng, D. Gasparro, and H. C. Kwan, "Near-Infrared Spectroscopy Study of Language Activated Hyper- and Hypo-Oxygenation in Human Prefrontal Cortex," International Journal of Neuroscience **118**, 657–666 (2008).

[210] T. Ota, K. Kamada, K. Kawai, M. Yumoto, and N. Saito, "Noninvasive determination of language dominance using multiple functional brain imaging," NeuroImage **47**, S120 (2009). Organization for Human Brain Mapping 2009 Annual Meeting.

[211] H. Sato, T. Takeuchi, and K. L. Sakai, "Temporal cortex activation during speech recognition: an optical topography study," Cognition **73**, B55 – B66 (1999).

[212] M. Bartocci, J. Winberg, C. Ruggiero, L. L. Bergqvist, G. Serra, and H. Lagercrantz, "Activation of olfactory cortex in newborn infants after odor stimulation: A functional near-infrared spectroscopy study," Pediatric Research **48**, 18–23 (2000).

[213] M. Ohnishi, N. Kusakawa, S. Masaki, K. Honda, N. Hayashi, Y. Shimada, I. Fujimoto, Hirao, and Konomu, "Measurement of hemodynamics of auditory cortex using magnetoencephalography and near infrared spectroscopy," Acta Oto-laryngologica **117**, 129–131 (1997).

[214] A. Villringer, J. Planck, C. Hock, L. Schleinkofer, and U. Dirnagl, "Near infrared spectroscopy (NIRS): A new tool to study hemodynamic changes during activation of brain function in human adults," Neuroscience Letters **154**, 101 – 104 (1993).

[215] B. Shadgan, W. D. Reid, R. Gharakhanlou, L. Stothers, and A. J. Macnab, "Wireless near-infrared spectroscopy of skeletal muscle oxygenation and hemodynamics during exercise and ischemia," Spectroscopy **23**, 233–241 (2009).

[216] T. Vaithianathan, I. D. C. Tullis, N. Everdell, T. Leung, A. Gibson, J. Meek, and D. T. Delpy, "Design of a portable near infrared system for topographic imaging of the brain in babies," Review of Scientific Instruments **75**, 3276–3283 (2004).

[217] P. Panzera, G. Cicco, R. Memeo, G. Catalano, L. Greco, F. Staffieri, L. Lupo, and V. Memeo, "Predictive Value of Alterations of Brain Perfusion During Liver Transplantation," Transplantation Proceedings **37**, 2622–2625 (2005).

[218] C. D. Kurth, J. C. McCann, J. Wu, L. Miles, and A. W. Loepke, "Cerebral Oxygen Saturation-Time Threshold for Hypoxic-Ischemic Injury in Piglets," Anesthesia & Analgesia **108**, 1268–1277 (2009).

[219] S. Moritz, P. Kasprzak, M. Arlt, K. Taeger, and C. Metz, "Accuracy of Cerebral Monitoring in Detecting Cerebral Ischemia during Carotid Endarterectomy: A Comparison of Transcranial Doppler Sonography, Near-infrared Spectroscopy, Stump Pressure, and Somatosensory Evoked Potentials," Anesthesiology **107**, 563–569 (2007).

[220] J. M. Murkin, S. J. Adams, R. J. Novick, M. Quantz, D. Bainbridge, I. Iglesias, A. Cleland, B. Schaefer, B. Irwin, and S. Fox, "Monitoring Brain Oxygen Saturation During

Coronary Bypass Surgery: A Randomized, Prospective Study," Anesthesia & Analgesia **104**, 51–58 (2007).

[221] M. M. Tisdall and M. Smith, "Multimodal monitoring in traumatic brain injury: current status and future directions," Br. J. Anaesth. **99**, 61–67 (2007).

[222] S. R. Hintz, D. A. Benaron, A. M. Siegel, A. Zourabian, D. K. Stevenson, and B. A. Boas, "Bedside functional imagin of the premature infant brain during passive motor activation," Journal of Perinatal Medicine **29**, 335–343 (2001).

[223] T. Kusaka, K. Isobe, K. Nagano, K. Okubo, S. Yasuda, M. Kondo, S. Itoh, and S. Onishi, "Estimation of regional cerebral blood flow distribution in infants by near-infrared topography using indocyanine green," NeuroImage **13**, 944 – 952 (2001).

[224] G. Naulaers, G. Morren, S. Van Huffel, P. Casaer, and H. Devlieger, "Cerebral tissue oxygenation index in very premature infants," Archives of Disease in Childhood - Fetal and Neonatal Edition **87**, F189–192 (2002).

[225] A. Petrova and R. Mehta, "Near-infrared spectroscopy in the detection of regional tissue oxygenation during hypoxic events in preterm infants undergoing critical care," Pediatric Critical Care Medicine **7**, 449–454 (2006).

[226] W. N. J. M. Colier, V. Quaresima, B. Oeseburg, and M. Ferrari, "Human motor-cortex oxygenation changes induced by cyclic coupled movements of hand and foot," Experimental Brain Research **129**, 457–461 (1999).

[227] M. Okamoto, H. Dan, K. Shimizu, K. Takeo, T. Amita, I. Oda, I. Konishi, K. Sakamoto, S. Isobe, T. Suzuki, K. Kohyama, and I. Dan, "Multimodal assessment of cortical activation during apple peeling by NIRS and fMRI," NeuroImage **21**, 1275 – 1288 (2004).

[228] S. Perrey, "Non-invasive NIR spectroscopy of human brain function during exercise," Methods **45**, 289 – 299 (2008). Neuroimaging in the sports sciences.

[229] F. Fedele, M. J. Eppstein, J. P. Laible, A. Godavarty, and E. M. Sevick-Muraca, "Fluorescence photon migration by the boundary element method," Journal of Computational Physics **210**, 109 – 132 (2005).

[230] S. Kurz, O. Rain, and S. Rjasanow, "The Adaptive Cross-Approximation Technique for the 3D Boundary-Element Method," IEEE Transactions on Magnetics **38**, 421–424 (2002).

[231] S. Kurz, R. O., and R. S., "Application of the Adaptive Cross-Approximation Technique for the Coupled BE-FE Solution of Symmetric Electromagnetic Problems," Computational Mechanics **32**, 423–429 (2003).

[232] M. Bebendorf and S. Rjasanow, "Adaptive low-rank approximation of collocation matrices," Computing **70**, 1–24 (2003).

[233] M. Bebendorf and R. Grzhibovskis, "Accelerating Galerkin BEM for Linear Elasticity Using Adaptive Cross-Approximation," Mathematical Methods In the Applied Sciences **29**, 1721–1747 (2006).

[234] M. Bonnet, "Methode multipole rapide," (2009). Ecole Doctorale MODES - Methodes Numeriques Avancees, Ecole Polytechnique, Palaiseau, France.

[235] L. Greengard and V. Rokhlin, "A fast algorithm for particle simulations," Journal of Computational Physics **73**, 325 – 348 (1987).

[236] K. E. Schmidt and M. A. Lee, "Implementing the fast multipole method in three dimensions," Journal of Statistical Physics **63**, 1223–1225 (1991).

[237] S. Chaillat, M. Bonnet, and J. F. Semblat, "A New Fast Multi-Domain BEM to Model Seismic Wave Propagation and Amplification in 3-D Geological Structures," Geophysical Journal International **177**, 509–531 (2009).

[238] M. Challacombe, C. White, and M. Head-Gordon, "Periodic boundary conditions and the fast multipole method," The Journal of Chemical Physics **107**, 10131–10140 (1997).

[239] R. Coifman, V. Rokhlin, and S. Wandzura, "The Fast Multipole Method for the Wave Equation: A Pedestrian Prescription," IEEE Antennas and Propagation Magazine **35**, 7–12 (1993).

[240] N. Geng, A. Sullivan, and L. Carin, "Fast Multipole Method for Scattering from an Arbitrary PEC Target Above of Buried in a Lossy Half Space," IEEE Transactions on Antennas and Propagation **49**, 740–748 (2001).

[241] K. N. Kudin and G. E. Scuseria, "Linear-scaling density-functional theory with gaussian orbitals and periodic boundary conditions: Efficient evaluation of energy and forces via the fast multipole method," Physical Review B **61**, 16440–16453 (2000).

[242] M. Yang, J. Song, Z. Chen, and N. Nakagawa, "A fast multipole boundary integral equation method for 2-dimensional diffusion problems," Review of Quantitative Nondestructive Evaluation **26**, 294–301 (2007).

[243] A. Buchau, W. M. Rucker, O. Rain, V. Rischmuller, S. Kurz, and S. Rjasanow, "Comparison Between Different Approaches for Fast and Efficient 3-D BEM Computations," IEEE Transactions on Magnetics **39**, 1107–1110 (2003).

[244] S. Arridge, "A Hybrid FEM-BEM model for Optical Tomography," Unpublished Note (2004).

[245] S. Chandrashekhar, *Radiative Transfer Theory* (Dover, 1960).

[246] J. Heino, S. Arridge, J. Sikora, and E. Somersalo, "Anisotropic effects in highly scattering media," Physical Review E **68**, 031908 (2003).

[247] A. P. Gibson, J. C. Hebden, and S. R. Arridge, "Recent advances in diffuse optical imaging," Physics in Medicine and Biology **50**, R1–R43 (2005).

[248] H. Jiang, K. D. Paulsen, and U. L. Osterberg, "Optical image reconstruction using frequency-domain data: Simulations and experiments," Journal of the Optical Society of America A **13**, 253–266 (1996).

[249] M. A. Atalay, "Milne problem for linearly anisotropic scattering and a specular and diffuse reflecting boundary," Journal of Quantitative Spectroxcopy and Radiative Transfer **72**, 589–606 (2002).

[250] A. Ishimaru, *Wave propagation and Scattering in Random Media, Vol. 1: Single scattering and transport theory* (Academic Press, New York, 1978).

[251] A. Kienle, "Light diffusion through a turbid parallelepiped," Journal of the Optical Society of America A **22**, 1883–1888 (2005).

[252] G. Popescu, C. Mujat, and A. Dogariu, "Evidence of scattering anisotropy effects on boundary conditions of the diffusion equation," Physical Review E **61**, 4523–4529 (2000).

[253] D. Contini, F. Martelli, and G. Zaccanti, "Photon migration through a turbid slab described by a model based on diffusion approximation. i. theory," Applied Optics **36**, 4587–4599 (1997).

[254] K. Case and P. Zweifel, *Linear Transport Theory* (Addison-Wesley, Reading, MA, 1967).

[255] M. Bonnet, *Boundary Integral Equation Methods for Fluids and Solids* (John Wiley and Sons, 1999).

[256] J.-B. Thibaud, "Propagation de la lumiere en milieu aleatoire. fondements et limites de la description radiometrique. application a l'imagerie," Ph.D. thesis, Ecole Centrale Paris, Formation Doctorale en Energetique (2000).

[257] G. Beer, *Programming the Boundary Element Method: an introduction for Engineers* (John Wiley & Sons, 2001).

[258] F. Zhang, *The Schur complement and its applications* (Springer, 2005).

[259] Q. Zhang, T. J. Brukilacchio, A. Li, J. J. Stott, T. Chaves, E. Hillman, T. Wu, M. Chorlton, E. Rafferty, R. H. Moore, D. B. Kopans, and D. A. Boas, "Coregistered tomographic x-ray and optical breast imaging: initial results," Journal of Biomedical Optics **10**, 024033 (2005).

[260] V. Ntziachristos, A. G. Yodh, M. Schnall, and B. Chance, "Concurrent MRI and diffuse optical tomography of breast after indocyanine green enhancement," Proceedings of the National Academy of Sciences of the United States of America **97**, 2767–2772 (2000).

[261] D. W. Shattuck and R. M. Leahy, "Brainsuite: An automated cortical surface identification tool," Medical Image Analysis **6**, 129 – 142 (2002).

[262] S. Azernikov and A. Fischer, "A new volume warping method for surface reconstruction," Virtual and Physical Prototyping **1**, 65–71 (2006).

[263] A. P. Gibson, J. Riley, M. Schweiger, J. C. Hebden, S. R. Arridge, and D. T. Delpy, "A method for generating patient-specific finite element meshes for head modelling," Physics in Medicine and Biology **48**, 481–495 (2003).

[264] A. Magri, A. Krol, M. Unlu, E. Lipson, J. Mandel, W. McGraw, W. Lee, I. Coman, and D. Feiglin, "Nonrigid registration of dynamic breast F-18-FDG PET/CT images using deformable FEM model and CT image warping," in "Society of Photo-Optical Instrumentation Engineers (SPIE) Conference Series," , vol. 6512 of *Society of Photo-Optical Instrumentation Engineers (SPIE) Conference Series* (2007), vol. 6512 of *Society of Photo-Optical Instrumentation Engineers (SPIE) Conference Series*.

[265] S. M. Shontz and S. A. Vavasis, "A mesh warping algorithm based on weighted laplacian smoothing," 12th International Meshing Roundtable (2004).

[266] I. A. Sigal, M. R. Hardisty, and C. M. Whyne, "Mesh-morphing algorithms for specimen-specific finite element modeling," Journal of Biomechanics **41**, 1381 – 1389 (2008).

[267] J. Schoeberl, "NETGEN An Advancing Front 2D/3D-Mesh Generator Based on Abstract Rules," Computing and Visualization in Science **1**, 41–52 (1997).

[268] M. Schweiger, S. R. Arridge, and I. Nissila, "Gauss-newton method for image reconstruction in diffuse optical tomography," Physics in Medicine and Biology **50**, 2365 (2005).

[269] J. C. Hebden, F. M. Gonzalez, A. Gibson, E. M. C. Hillman, R. M. Yusof, N. Everdell, D. T. Delpy, G. Zaccanti, and F. Martelli, "Assessment of an in situ temporal calibration method for time-resolved optical tomography," Journal of Biomedical Optics **8**, 87–92 (2003).

[270] J. C. Hebden, H. Veenstra, H. Dehghani, E. M. C. Hillman, M. Schweiger, S. R. Arridge, and D. T. Delpy, "Three-dimensional time-resolved optical tomography of a conical breast phantom," Applied Optics **40**, 3278–3287 (2001).

[271] J. A. Fessler and B. P. Sutton, "Nonuniform fast fourier transforms using min-max interpolation," IEEE Transactions on Signal Processing **51**, 560–574 (2003).

[272] S. Arridge and J. Schotland, "Optical tomography: forward and inverse problems," ArXiv e-prints (2009).

[273] C. Hansen, "Rank-deficient and discrete ill-posed problems," Ph.D. thesis, Technical University of Denmark (1996).

[274] A. D. Zacharopoulos, M. Schweiger, V. Kolehmainen, and S. Arridge, "3D shape based reconstruction of experimental data in Diffuse Optical Tomography," Optics Express **17**, 18940–18956 (2009).

[275] J. C. Hebden, "Advances in Optical Imaging of the Newborn Infant Brain," Psychophysiology **40**, 501–510 (2003).

[276] J. C. Hebden and T. Austin, "Optical tomography of the neonatal brain," European Radiology **17**, 2926–2933 (2007).

[277] M. Firbank, M. Oda, and D. T. Delpy, "An improved design for a stable and reproducible phantom material for use in near-infrared spectroscopy and imaging," Physics in Medicine and Biology **40**, 955 (1995).

[278] G. Beer, "Finite element, boundary element and coupled analysis of unbounded problems in elastostatics," International Journal for Numerical Methods in Engineering **19**, 567–580 (1983).

[279] X. Yuan, D. R. Lynch, and J. W. Strohbehn, "Coupling of finite element and moment methods for electromagnetic scattering from inhomogeneous objects," IEEE Transactions on Antennas and Propagation **38**, 386–393 (1990).

[280] S. R. Arridge, J. P. Kaipio, V. Kolehmainen, M. Schweiger, E. Somersalo, T. Tarvainen, and M. Vauhkonen, "Approximation errors and model reduction with an application in optical diffusion tomography," Inverse Problems **22**, 175 (2006).

[281] M. Guven, B. Yazici, X. Intes, and B. Chance, "Diffuse optical tomography with a priori anatomical information," Physics in Medicine and Biology **50**, 2837–2858 (2005).

[282] A. Li, G. Boverman, Y. Zhang, D. Brooks, E. L. Miller, M. E. Kilmer, Q. Zhang, E. M. C. Hillman, and D. A. Boas, "Optimal linear inverse solution with multiple priors in diffuse optical tomography," Applied Optics **44**, 1948–1956 (2005).

[283] M. Schweiger, "Application of the finite element method in infrared image reconstruction of scattering media," Ph.D. thesis, University of London (1994).

[284] S. R. Arridge and M. Schweiger, "Photon Measurement Density Functions. Part 2: Finite Element Calculations," Applied Optics **34**, 8026–8037 (1995).

[285] A. Tizzard, L. Horesh, R. J. Yerworth, D. S. Holder, and R. H. Bayford, "Generating Accurate Finite Element Meshes for the Forward Model of the Human Head in EIT," Physiological Measurements **26**, S251–S261 (2005).

[286] P. Lindstrom and G. Turk, "Fast and memory efficient polygonal simplification," Visualization '98 Proceedings pp. 279–286 (1998).

[287] F. Qianqian, S. A. Carp, J. Selb, R. Moore, D. B. Kopans, E. L. Miller, D. H. Brooks, and D. A. Boas, "A multi-modality image reconstruction platform for diffuse optical tomography," Tech. rep., Biomedical Optics (BIOMED Poster Session II) (2008).

[288] M. Abramovitz and I. A. Stegun, *Handbook of Mathematical Functions* (Dover, 1970).

[289] E. Darve, "The fast multipole method: Numerical implementation," Journal of Computational Physics **160**, 195–240 (2000).

[290] S. Chaillat, M. Bonnet, and J. F. Semblat, "A Multi-Level Fast Multipole BEM for 3-D Elastodynamics in the Frequency Domain," Computer Methods in Applied Mechanics and Engineering **197**, 4233–4249 (2008).

[291] T. Malas and L. Gurel, "Incomplete lu preconditioning with the multilevel fast multipole algorithm for electromagnetic scattering," SIAM Journal on Scientific Computing **29**, 1476–1494 (2007).

[292] K. Sertel and J. L. Volakis, "Incomplete lu preconditioner for fmm implementation," Microwave and Optical Technology Letters **26**, 265–267 (2000).

[293] B. Carpentieri, I. S. Duff, L. Giraud, and G. Sylvand, "Combining fast multipole techniques and an approximate inverse preconditioner for large electromagnetism calculations," SIAM Journal on Scientific Computing **27**, 774–792 (2005).

[294] E. Darve, "The fast multipole method i: Error analysis and asymptotic complexity," SIAM Journal on Numerical Analysis **38**, pp. 98–128 (2001).

[295] G. Sylvand, "La methode multipole rapide en electromagnetisme: performances, parallelisation, applications," Ph.D. thesis, Ecole Nationale des Ponts et Chaussees (2002).

[296] V. I. Lebedev and D. N. Laikov, "A quadrature formula for the sphere of the 131st algebraic order of accuracy," Doklady Mathematics **59**, 477–481 (1999).

[297] J. Elisee, A. Gibson, and S. Arridge, "Combination of boundary element method and finite element method in diffuse optical tomography," Biomedical Engineering, IEEE Transactions on **57**, 2737–2745 (2010).

[298] A. D. Zacharopoulos, S. R. Arridge, O. Dorn, V. Kolehmainen, and J. Sikora, "Three-dimensional reconstruction of shape and piecewise constant region values for optical tomography using spherical harmonic parametrization and a boundary element method," Inverse Problems **22**, 1509–1532 (2006).